

Review on the lithium transport mechanism in solid-state battery materials

Zhong-Heng Fu  | Xiang Chen  | Qiang Zhang 

Beijing Key Laboratory of Green Chemical Reaction Engineering and Technology, Department of Chemical Engineering, Tsinghua University, Beijing, People's Republic of China

Correspondence

Xiang Chen and Qiang Zhang, Beijing Key Laboratory of Green Chemical Reaction Engineering and Technology, Department of Chemical Engineering, Tsinghua University, Beijing 100084, People's Republic of China.
 Email: xiangchen@mail.tsinghua.edu.cn and zhang-qiang@mails.tsinghua.edu.cn

Funding information

China Postdoctoral Science Foundation, Grant/Award Numbers: 2021TQ0161, 2021M691709; Guoqiang Institute at Tsinghua University, Grant/Award Number: 2020GQG1006; National Key Research and Development Program, Grant/Award Number: 2021YFB2500300; National Natural Science Foundation of China, Grant/Award Numbers: 22109086, U1801257, 21825501; Natural Science Foundation of Beijing Municipality, Grant/Award Number: Z200011

Edited by: Jinlong Yang, Associate Editor
 and Peter R. Schreiner, Editor-in-Chief

Abstract

The growing demands to mitigate climate change and environmental degradation stimulate the rapid developments of rechargeable lithium (Li) battery technologies. Fast Li transports in battery materials are of essential significance to ensure superior Li dynamical stability and rate performance of batteries. Herein, the Li transport mechanisms in solid-state battery materials (SSBMs) are comprehensively summarized. The collective diffusion mechanisms in solid electrolytes are elaborated, which are further understood from multiple perspectives including lattice dynamics, crystalline structure, and electronic structure. With the exponentially improving performance of computers, atomistic simulations have been playing an increasingly important role in revealing and understanding the Li transport in SSBMs, bridging the gap between experimental phenomena and theoretical models. Theoretical and experimental characterization methods for Li transports are discussed. The design strategies toward fast Li transports are classified. Finally, a perspective on the achievements and challenges of probing Li transports is provided.

This article is categorized under:

Structure and Mechanism > Computational Materials Science

KEY WORDS

lithium transport mechanism, solid-state battery, solid electrolytes

1 | INTRODUCTION

The global climatic and environmental concerns induced by anthropogenic greenhouse gas emissions have resulted in multidimensional issues including global warming, ecological imbalance, technological issues, economic issues, and societal issues.^{1,2} Developing alternative, renewable, and clean energy such as wind, solar, and hydrogen energies is a promising solution to mitigate the environmental issues and enable social sustainability. However, because of the intermittent nature of renewable energy, it is necessary to develop stable, reliable, and high-performance energy storage devices matching the conversion and storage of renewable energy.^{3–5} Electrochemical energy storage devices represented by lithium (Li) batteries feature high energy density, no memory effect, and low self-discharge rate, which has been widely used in portable electronic devices and smart grids.^{6,7}

A battery is consisting of several electrochemical cells connected in series and/or in parallel. The cells are further divided into anodes, cathodes, and electrolytes. Anodes and cathodes are used for the conversion between chemical and electrical energy, between which the electrolytes permit the ionic transfer and block electronic transport.^{8–10} The organic liquid electrolytes including ethylene carbonate (EC) and diethyl carbonate (DEC) are usually adopted in conventional Li-ion batteries.^{11,12} However, the safety concern for flammable organic electrolytes stimulates the rapid development of alternative solid electrolytes (SEs).^{13–15} The batteries with SEs are accordingly named solid-state batteries (SSBs; Figure 1). Based on electrochemical lithiation/delithiation mechanisms, anode materials are classified into three types, that is, alloying (e.g., Si and Sn),^{16–18} conversion (e.g., Fe₂O₃, Fe₃O₄, SiO_x, and SnO₂),^{19,20} and intercalation (e.g., graphite and Li₄Ti₅O₁₂).^{21–23} Cathode materials are split into conversion (e.g., S) and intercalation (e.g., LiFePO₄, LiCoO₂, LiMn₂O₄, and LiNi_xMn_yCo_zO₂) by a similar classification strategy.^{24–26}

Rate performances of batteries largely rely on Li transport properties. Especially, fast charging is recently proposed to be a key requirement for the economic success of electric vehicles.²⁷ Although macroscopic electrochemical impedances, microscopic Li diffusion channels, and averaged Li-ion diffusion coefficients can be figured out by electrochemical impedance spectroscopy (EIS) and solid-state nuclear magnetic resonance (ssNMR) spectroscopy, it is still challenging to fundamentally understand the relationship between structures and Li transport behaviors.²⁸ For instance, defects in solids are believed to be closely related to diffusions. Zero-dimensional (0D) point defects including interstitials and vacancies are defined as diffusion vehicles. One-dimensional (1D) dislocations and two-dimensional (2D) grain boundaries are considered as fast ionic diffusion channels, that is, diffusion short circuits. Despite that tremendous achievements (e.g., Li transport impeded by single-atom-layer trap²⁹ and facilitated by Schottky defect pairs³⁰) have been made in probing the Li transports at defect structures, it is still puzzling to fully understand the role of defects in Li transports.

Atomistic simulation techniques have been becoming a powerful tool to understand Li transport behaviors with the ever-increasing computing power. Transport-related physical quantities including carrier concentration, activation energy, diffusion coefficient, and ionic conductivity are explicitly determined by the atomistic simulation techniques, which are beneficial to reveal underlying transport mechanisms and rationally designing materials with targeted properties. First-principles calculations based on density functional theory (DFT) efficiently figure out electronic structures, total energy, and material properties. Molecular dynamics (MD) based on classical Newton's equation of motion simulates the random walk of atoms and calculates diffusion coefficients. Deep physics and chemistry are revealed with the assistance of atomistic simulations, for example, understanding interatomic interactions and correlations between ionic motions. Atomistic simulations are playing an increasingly important role in multidisciplinary research fields including physics, chemistry, material science, and engineering.

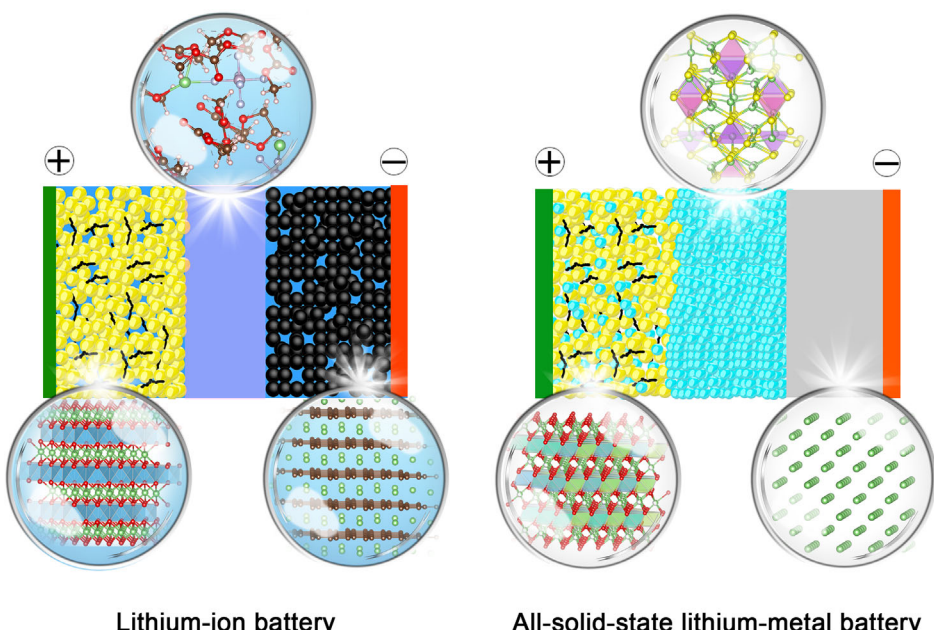


FIGURE 1 A schematic of a conventional Li-ion battery and all-solid-state Li-metal battery

In this review, the Li transport mechanisms in solid-state battery materials (SSBMs) are comprehensively summarized. A relationship between structures and Li transport mechanisms is established. Several theoretical insights including collective diffusion mechanisms and the relationship between lattice dynamics and ionic migrations are highlighted. First, the computational and experimental characterization methods to probe ionic transports are introduced in Section 2. Second, Li transport mechanisms in SSBMs are discussed in Section 3. Third, the design strategies for fast Li transports are classified in Section 4. Finally, the achievements and challenges of understanding Li transport mechanisms are provided.

2 | METHODS

Li transports in SSBMs are a scientific issue covering a temporal scale of 10^{-15} – 10^0 s and a spatial scale of 10^{-12} – 10^{-2} m. The Li transport mechanism at the atomistic scale is focused on in this review. The ionic transport at different scales and conventional DFT and MD methods were elaborately discussed in several high-quality reviews.^{28,31–33} Emerging simulation methods, for example, machine learning molecular dynamics (MLMD), are especially focused on in the following.

2.1 | Density functional theory

DFT is a computational quantum mechanical modeling method, which can efficiently determine the ground state of both geometric and electronic structures of many-body systems. In the framework of DFT, the motions of nuclei and electrons are separated because of their significant mass difference, that is, Born–Oppenheimer approximation. The stationary electronic wavefunction $\Psi(\mathbf{r}_1, \dots, \mathbf{r}_N)$ is governed by the many-electron time-independent Schrödinger equation,

$$\hat{H}\Psi = (\hat{T} + \hat{V} + \hat{U})\Psi = \left[\sum_i \left(-\frac{\hbar^2}{2m_i} \nabla_i^2 \right) + \sum_i V(\mathbf{r}_i) + \sum_{i < j} U(\mathbf{r}_i, \mathbf{r}_j) \right] \Psi = E\Psi \quad (1)$$

in which \hat{H} , \hat{T} , \hat{V} , and \hat{U} denote the operators of Hamiltonian, kinetic energy, potential energy, and electron–electron interaction energy, respectively. E , \hbar , and m_i are the total energy of the system, reduced Planck constant, and the electronic mass, respectively. The Schrödinger equation is usually solved by the expansion of the electronic wavefunctions in many quantum chemical methods, for example, Hartree–Fock and post-Hartree–Fock methods. Alternatively, the DFT deals with the Schrödinger equation based on the electron density $n(\mathbf{r})$,

$$n(\mathbf{r}) = N \int d^3\mathbf{r}_2 \cdots \int d^3\mathbf{r}_N \Phi^*(\mathbf{r}, \mathbf{r}_2, \dots, \mathbf{r}_N) \Phi(\mathbf{r}, \mathbf{r}_2, \dots, \mathbf{r}_N) \quad (2)$$

where $\Phi(\mathbf{r}, \mathbf{r}_2, \dots, \mathbf{r}_N)$ is a normalized electronic wavefunction.

The accuracy of the DFT calculation depends on the quality of the exchange–correlation energy E_{XC} .³⁴ It has taken decades to develop new approximations of E_{XC} with high accuracy, such as local density approximation (LDA),³⁵ generalized gradient approximation (GGA) proposed by Perdew–Wang,³⁶ Perdew–Burke–Ernzerhof,³⁷ and Becke–Lee–Yang–Parr,^{38,39} and more accurate meta-GGA.⁴⁰ In addition, hybrid functionals including HSE03 and HSE06,⁴¹ and GGA + U approach⁴² can further improve the accuracy of GGA functionals. Recently, machine learning (ML) is proposed to be a promising approach to constructing specific E_{XC} , which has been successfully applied to the organic molecules.^{43–46} Initial high-quality datasets including total energy, atomic force, and ground-state electron density are constructed by the second-order Møller–Plessett perturbation theory (MP2), Coupled-cluster singles, doubles, and perturbative triples (CCSD[T]), or quantum Monte Carlo (QMC). Gaussian process regression or deep neural network is used for the training to enable the prediction of correlated wavefunction energies. However, it is still far away from practical applications in solids because of more freedom degrees.

Once the ground-state electronic structures of the systems are determined, material properties are further solved by the DFT calculations, for example, defect formation energy and potential energy surface (PES) of Li transports in lattices. The former determines carrier types and carrier concentrations. The latter reveals diffusion pathways, and

determines the activation energy of Li transports. More details can be found in several comprehensive reviews.^{47–50} Herein, only nudged elastic band (NEB) method is introduced.

The saddle point in the PES corresponds to the diffusion barrier according to the transition-state theory (Figure 2a). The NEB method is usually adopted to accelerate the search for saddle points and minimum energy paths.⁵¹ A constrained optimization of intermediate images along the transport path is performed by the NEB method, where each image automatically searches for the minimum in the PES and keeps equal spacing to neighboring images. The spring forces along the band between images are applied. The components of the spring force perpendicular to the pathway are projected out (Figure 2b).

2.2 | Molecular dynamics

MD is a computational simulation technique that predicts the time evolution of an atomic system by conducting numerical integration of Newton's equation of motion.⁵⁵ The statistical quantities of the system can be derived from the atomic motion information in the MD simulations.

The classical motion of a N -atom system follows Newton's equation of motion,

$$m_i \frac{d^2 \mathbf{r}_i}{dt^2} = \mathbf{F}_i \quad (3)$$

where m_i , \mathbf{r}_i , t , and \mathbf{F}_i are the atomic mass, position coordinate, time, and atomic force of the i^{th} atom, respectively. The Hamiltonian of the system is expressed as

$$H(\mathbf{p}, \mathbf{r}) = \sum_i \frac{\mathbf{p}_i^2}{2m_i} + U(\mathbf{r}_1, \dots, \mathbf{r}_N) \quad (4)$$

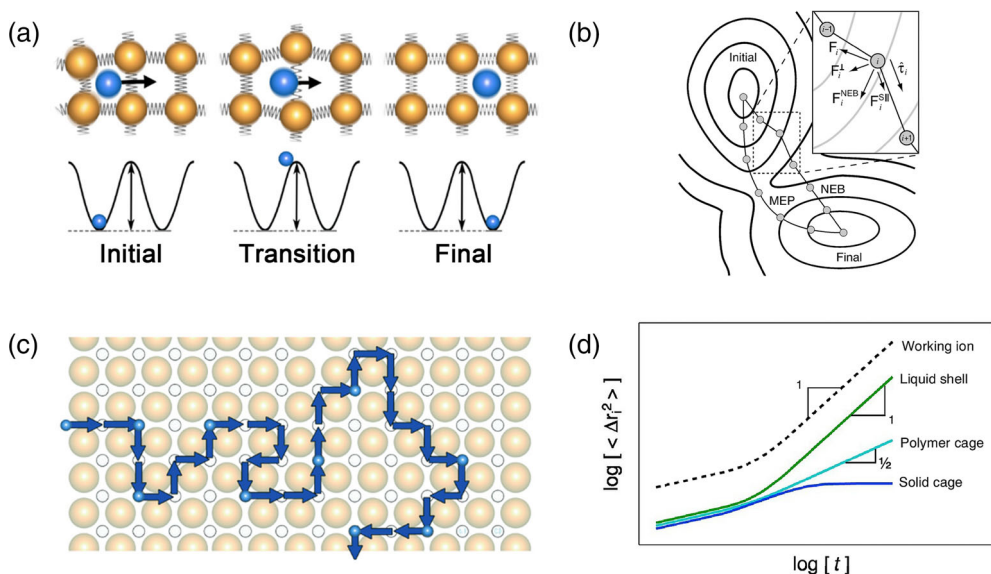


FIGURE 2 Schematic of atomistic simulation methods. (a) An ionic jump between sites and the corresponding PES. Reprinted with permission from Reference 52. Copyright © 2021 ChemRxiv. (b) A schematic of the NEB method. An additional NEB force $\mathbf{F}_i^{\text{NEB}}$ is introduced, which is projected into the spring force \mathbf{F}_i^{\parallel} along the tangent $\hat{\tau}_i$ and the perpendicular force \mathbf{F}_i^{\perp} . Reprinted with permission from Reference 53. Copyright © 2008 AIP Publishing. (c) A schematic of ionic random walk within a lattice. Reprinted with permission from Reference 52. Copyright © 2021 ChemRxiv. (d) Mean square displacements (MSDs) of the working ion and elements of shells and cages $\langle \Delta \mathbf{r}_i^2 \rangle$ as a function of time t in different electrolytes. Reprinted with permission from Reference 54. Copyright © 2021 Elsevier

where \mathbf{p}_i is the momentum of the i^{th} atom. $U(\mathbf{r}_1, \dots, \mathbf{r}_N)$ is the potential energy. The derivation of the potential is the atomic force \mathbf{F}_i ,

$$\mathbf{F}_i = -\frac{\partial U(\mathbf{r}_1, \dots, \mathbf{r}_N)}{\partial \mathbf{r}_i} \quad (5)$$

Therefore, the accuracy of the MD simulation directly depends on the quality of the interatomic potential. The preliminary interatomic interaction is simply considered a perfect collision, that is, a “hard-sphere” model, which was used for the research on liquid dynamics in 1957.⁵⁶ Since such an intuitive description of the interatomic interaction is far away from the real condition, a smooth and continuous non-bonded Lennard-Jones potential was proposed by Rahman in 1964.⁵⁷

$$U(\mathbf{r}) = 4\epsilon \left[\left(\frac{\sigma}{\mathbf{r}} \right)^{12} - \left(\frac{\sigma}{\mathbf{r}} \right)^6 \right] \quad (6)$$

where ϵ , σ , and \mathbf{r} are the depth of the potential well (i.e., dispersion energy), the distance where the potential energy U is zero (i.e., size of the particle), and interatomic distance, respectively. Lennard-Jones potential reasonably describes van der Walls forces. The contribution of three or more atoms interacting with each other to the potential energy is considered in many-body potential, such as Tersoff potential⁵⁸ and embedded-atom method (EAM) potential.⁵⁹ Covalent and metallic systems are well described by the many-body potential.

In addition to the above empirical interatomic potential, the potential can also be constructed by *ab initio* method on the fly. MD simulations are traditionally divided into two classes, classical mechanics and quantum mechanics approaches by the mathematical formalism involved. The former (classical molecular dynamics, CMD) treats atoms as classical objects under a classical mechanics framework, while the latter (*Ab initio* molecular dynamics, AIMD) considers the quantum nature of chemical bonds. As a consequence, AIMD usually exhibits an improved simulation accuracy compared with CMD, especially in the situation involving charge transfer, and inevitably consumes more computational resources.

The boundary in the classification of potential functions is recently getting blurred with the introduction of ML techniques. A new-coming potential function, namely machine learning potential (MLP), is rapidly developing, in which ML methods, for example, neural network and Gaussian process regression, efficiently tackle the regression tasks of energy fitting.

Neural network potential (NNP) was first proposed by Doren et al. in 1995,⁶⁰ which was used to probe the H₂ adsorption at the Si(100) surface. A feed-forward neural network (FFNN) is adopted as the central component in the first-generation NNP. However, the application of the first-generation NNP is limited because it cannot tackle the system with the variable atomic numbers. A high-dimensional NNP (HDNNP) was further developed by Behler and Parrinello in 2007,⁶¹ that is, the second-generation NNP, in which the description of interatomic interactions is changed from a single FFNN for the global PES to an individual NN for every atom. The potential energy is expressed as a sum of atomic pair energies E_{ij} ,

$$E = \sum_i^{N_{\text{atom}}} \sum_{j > i}^{N_{\text{atom}}} E_{ij} \quad (7)$$

where N_{atom} is the number of atoms. Atom-centered symmetry functions (ACSF) are constructed as an ideal descriptor preserving the translational, rotational, and permutational invariances of the PES. Radial symmetry functions are expressed as a sum of Gaussians,

$$G_i^{\text{rad}} = \sum_{i \neq j} e^{-\eta(r_j - r_s)^2} f_c(r_{ij}) \quad (8)$$

where r_{ij} is the distance between atoms i and j . The parameters η and r_s control the width of the Gaussians and the position shift of the centers of the Gaussians, respectively. $f_c(r_{ij})$ is a cutoff function based on the locality approximation,

$$f_c(r_{ij}) = \begin{cases} 0.5 \left[\cos\left(\frac{\pi r_{ij}}{r_c}\right) + 1 \right] & \text{for } r_{ij} \leq r_c \\ 0 & \text{for } r_{ij} > r_c \end{cases} \quad (9)$$

where r_c is the cutoff radius. Angular symmetry functions have a form of

$$G_i^{\text{ang}} = 2^{1-\zeta} \sum_{i,j,k} (1 + \lambda \cos \theta_{ijk})^\zeta e^{-\eta' (r_{ij}^2 + r_{ik}^2 + r_{jk}^2)} f_c(r_{ij}) f_c(r_{ik}) f_c(r_{jk}) \quad (10)$$

where $\cos \theta_{ijk}$ is the angle between the connections of the atom i with the atoms j and k . The parameters η' and ζ control the width of the Gaussians and angular resolution, respectively. Another parameter λ determines the positions of the maxima of the cosine function at $\theta_{ijk} = 0^\circ$ ($\lambda = 1$) or $\theta_{ijk} = 180^\circ$ ($\lambda = -1$). The long-range electrostatic and dispersion interactions are considered in the third-generation NNPs,⁶² which are beyond the short-range chemical interactions in the local environments. The nonlocal effects, for example, long-range charge transfer, are recently involved in the fourth-generation NNPs,⁶³ indicating an increasingly reasonable consideration of physical and chemical environments. In addition, other descriptors including the Chebyshev polynomials,⁶⁴ the Zernike descriptor,⁶⁵ and the atomic coordinated-based descriptor⁶⁶ are also used for the NNPs.

The Gaussian process regression is used in the Gaussian Approximation Potential (GAP),⁶⁷ in which smooth-overlap of atomic positions (SOAP) kernels are adopted as structural descriptors. The GAP model energy is expressed as a sum of a pair potential and a many-body term,

$$E = \sum_{i < j} V^{(2)}(r_{ij}) + \sum_i \sum_s^M \alpha_s K(R_i, R_s) \quad (11)$$

where r_{ij} is the distance between atoms i and j . R_i is the collection of position vectors from the atom i to all the neighboring atoms, which is called a neighborhood. M representative atoms are extracted from the input dataset, which is used to construct a basis. The kernel $K(R_i, R_s)$ describes the similarity between neighborhoods. The neighborhood R_i of the atom i is further expressed as a neighbor density $\rho_i(\mathbf{r})$ in the SOAP kernel,

$$\rho_i(\mathbf{r}) = \sum_{i'} f_c(r_{ii'}) e^{-(\mathbf{r}-\mathbf{r}_{ii'})/2\sigma_{\text{atom}}^2} \quad (12)$$

where $f_c(r_{ii'})$ and σ_{atom} are a cutoff function and a smearing parameter, respectively. The neighbor density $\rho_i(\mathbf{r})$ is further expanded on a basis of spherical harmonics $Y_{lm}(\hat{\mathbf{r}})$ and radial functions $g_n(r)$,

$$\rho_i(\mathbf{r}) = \sum_{nlm} c_{nlm}^i Y_{lm}(\hat{\mathbf{r}}) g_n(r) \quad (13)$$

The spherical power spectrum vector is a description preserving the rotational and permutational invariances of the neighbor environment,

$$\tilde{p}_{nn'l}^i = \sum_{m=-l}^l c_{nlm}^{i*} c_{n'l'm}^i \quad (14)$$

$$\mathbf{p}^i = \tilde{\mathbf{p}}^i / |\tilde{\mathbf{p}}^i| \quad (15)$$

The SOAP kernel is represented by a scalar product,

$$K(R_i, R_s) = \delta^2 |\mathbf{p}^i \cdot \mathbf{p}^j|^\zeta \quad (16)$$

where ζ and δ are two hyperparameters, determining the spread of the kernel and the energy scale of the many-body term, respectively.

A brief workflow of MLMD with the MLP is described below using DeePMD⁶⁸ as an example. (1) The high-quality data including atomic coordinates, total energies, and atomic forces are extracted from short-time AIMD simulations. (2) The data is input into an initial training set. (3) Deep neural network is used to train a PES model. (4) MLMD simulations are performed based on the MLP. The root mean square errors (RMSE) of the energy and the force in the MLMD simulation are close to the levels of meV atom⁻¹ and meV Å⁻¹ based on an AIMD benchmark, respectively.⁶⁹ Such accuracy is comparable to that in the original AIMD simulation. The MLMD simulations exhibit a computational efficiency with an $O(N)$ scaling compared with the $O(N^3)$ scaling in the AIMD simulation,⁷⁰ in which the N denotes the number of atoms. The MLMD simulation is performed at larger spatial and temporal scales compared with the traditional AIMD simulation due to its increased computational speed. Because of the limited simulation scale in the AIMD simulation, the room-temperature ionic conductivity of SEs usually depends on a linear extrapolation of the Arrhenius equation in the traditional computational solution of diffusion properties. The method will fail to tackle a system with a non-Arrhenius behavior,⁷¹ for example, phase transitions or the transitions of ionic transport mechanisms. MLMD can simulate the behavior of Li-ion diffusions at room temperature, directly determining the room-temperature diffusion coefficient and ionic conductivity of SEs. Such a feature is beneficial to the material design of potential high-ionic-conductivity SEs and the understanding of ionic transport mechanisms. More details on the motivation, methodology, and application of MLP can be found in the insightful reviews written by Behler and Csanyi.⁷²⁻⁷⁴

The atoms usually undergo a random-walk process in MD simulations (Figure 2c). Diffusive Brownian motions are observed after a short-time ballistic region (Figure 2d). The ballistic region is derived from the harmonic vibrational motion of mobile ions around the equilibrium configurations.^{75,76} Tracer diffusion coefficients D^* are linearly fitted from the diffusive region based on the Einstein–Smoluchowski equation,^{77,78}

$$D^* = \frac{\langle [\mathbf{r}(t)]^2 \rangle}{2dt}, \quad (17)$$

where d , t , and $\langle [\mathbf{r}(t)]^2 \rangle$ are diffusion dimensionality, time, and MSD, respectively. MSD is an ensemble average,

$$\langle [\mathbf{r}(t)]^2 \rangle = \frac{1}{N} \sum_{n=1}^N \langle [\mathbf{r}_n(t+t_0)]^2 - [\mathbf{r}_n(t_0)]^2 \rangle, \quad (18)$$

where $\mathbf{r}_n(t)$ denotes the displacement of the n^{th} mobile ion at time t . The Einstein–Smoluchowski equation is an early example of the fluctuation–dissipation relation,⁷⁹ which makes a correlation between the microscopic diffusion behaviors and the macroscopic diffusion-related quantities.

Charge diffusion coefficient D_σ are linearly fitted from the MSD of the center-of-mass \mathbf{r}_{com} ,

$$D_\sigma = \frac{N \mathbf{r}(t)_{\text{com}}^2}{2dt}, \quad (19)$$

$$\mathbf{r}(t)_{\text{com}}^2 = \left[\frac{1}{N} \sum_{n=1}^N \mathbf{r}_n(t+t_0) - \mathbf{r}_n(t_0) \right]^2. \quad (20)$$

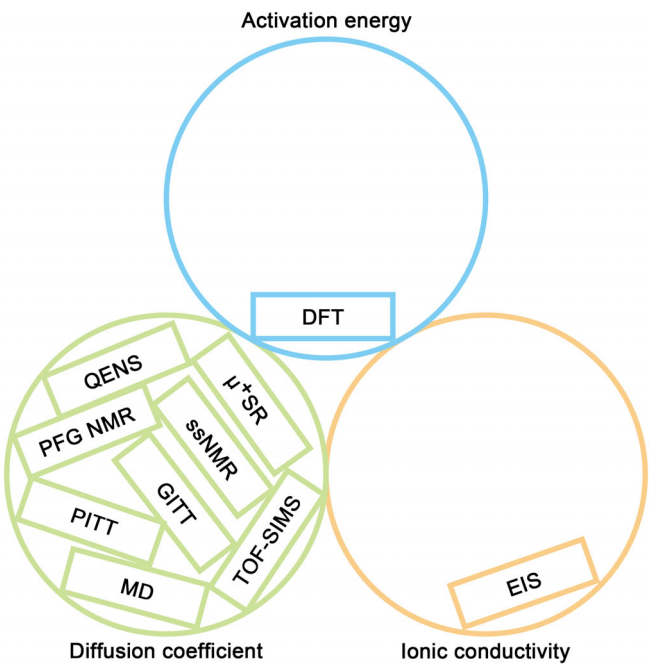


FIGURE 3 The correspondence between the transport-related physical quantities and the theoretical and experimental characterization methods

2.3 | Experimental characterization techniques

Experimental characterization techniques probing Li transport in SSBMs are divided into two classes as below. All experimental characterization methods except EIS determine diffusion coefficients, while EIS does ionic conductivities (Figure 3).

2.3.1 | Macroscopic ionic transport

Electrochemical impedance spectroscopy (EIS) is an electrochemical characterization technology, which is widely used to measure ionic conductivities of dielectric materials. When a frequency-dependent sinusoidal voltage signal is applied to samples, a corresponding current response is observed.⁸⁰ The frequency-dependent impedances including resistive and reactive components are determined. The ionic conductivities are further calculated based on the impedances and the sizes of the samples.

Galvanostatic intermittent titration technique (GITT) and potentiostatic intermittent titration technique (PITT) are two common transient measurement techniques. A constant current is applied to samples in the measurement of GITT, followed by a relaxation time.⁸¹ The change of the potential as a function of time is collected to probe electrode kinetics. Assuming that the Li transport is controlled by the diffusion process, the diffusion coefficient is determined by the formula proposed by Weppner and Huggins,⁸²

$$D = \frac{4}{\pi} \left(\frac{V_M}{SFn} \right)^2 \left[I_O \left(\frac{dE}{d\delta} \right) / \left(\frac{dE}{d\sqrt{t}} \right) \right]^2 \text{ for } t \ll L^2/D \quad (21)$$

where V_M , S , F , n , and I_O are the mole volume of the electrode material, the surface area of the electrode, the Faraday's constant, electron number, and applied current, respectively. $\frac{dE}{d\delta}$ and $\frac{dE}{d\sqrt{t}}$ are the slopes of the coulometric titration curve and of the potential versus square root of the time during the current pulse, respectively.

Electrode potential is changed quickly in PITT, following to keep a constant potential. Time-dependent current is recorded to determine the electrode relaxation process, which is formulated as⁸³

$$i = \frac{2FS(C_s - C_0)D}{L} \exp\left(-\frac{\pi^2 Dt}{4L^2}\right) \quad (22)$$

in which F , S , $C_s - C_0$, D , and L denote the Faraday's constant, the surface area of the electrode, the concentration difference of Li ions at the surface at time t and at the beginning time during each potential pulse, diffusion coefficient, and the electrode thickness, respectively. The diffusion coefficient D is further determined by the equation⁸³

$$D = \frac{d\ln(i)}{dt} \frac{4L^2}{\pi^2}. \quad (23)$$

Time-of-flight secondary ion mass spectrometry (TOF-SIMS) is a surface-sensitive characterization method. Pulsed Cs- or Ga-ion beams are focused on samples to bombard surface atoms. A few atoms are removed from the surface and then accelerated into a flight tube. The masses of these atoms are determined by measuring the time of flight in the tube. The tracer diffusion coefficient is further calculated. The flat surface of SEs is partially covered by ${}^6\text{Li}$ metal when the diffusion coefficients of SEs are measured. The secondary ion signals from secondary ion mass spectrometry are collected to calculate the isotopic fraction of ${}^6\text{Li}$,⁸⁴

$$C({}^6\text{Li}) = \frac{I({}^6\text{Li}^+)}{I({}^6\text{Li}^+) + I({}^7\text{Li}^+)} \quad (24)$$

where $I({}^6\text{Li}^+)$ and $I({}^7\text{Li}^+)$ are the counts of ${}^6\text{Li}^+$ and ${}^7\text{Li}^+$, respectively. The normalized concentration of ${}^6\text{Li}$ $C'({}^6\text{Li})$ is formulated as,⁸⁴

$$C'({}^6\text{Li}) = \frac{C({}^6\text{Li}) - C_{\text{bg}}({}^6\text{Li})}{C_{\text{source}}({}^6\text{Li}) + C_{\text{bg}}({}^6\text{Li})}. \quad (25)$$

$C_{\text{bg}}({}^6\text{Li})$ and $C_{\text{source}}({}^6\text{Li})$ are the background isotopic fraction of ${}^6\text{Li}$ in SEs and the source concentration of ${}^6\text{Li}$ in the Li metal, respectively. The $C'({}^6\text{Li})$ is further expressed as a solution of Fick's second law for a semi-infinite medium,⁸⁴

$$C'({}^6\text{Li}) = \operatorname{erfc}\left(\frac{x}{2\sqrt{Dt}}\right) - \exp(hx + h^2Dt)\operatorname{erfc}\left(\frac{x}{2\sqrt{Dt}} + h\sqrt{Dt}\right) \quad (26)$$

where t , h , x , and D denote anneal time, the ratio of the surface exchange coefficient, the distance from the interface, and diffusion coefficient, respectively.

2.3.2 | Microscopic ionic transport

Nuclear magnetic resonance (NMR) is the oscillatory response of nuclei with non-zero spins to a magnetic field.⁸⁵ The jump frequency and jump distance of Li ions in solids are determined by ssNMR. At the onset temperature T_{onset} of the ionic motion, the jump frequency τ^{-1} is expressed as

$$\tau^{-1} = \sqrt{M_2} \quad (27)$$

where M_2 is the second moment in the rigid lattice line. The M_2 is further described by⁸⁶

$$M_2(\text{I}) = M_2(\text{II}) + \sum_S M_2(\text{IS}) \quad (28)$$

$$= \frac{3}{5} \gamma_i^4 h^2 I(I+1) \sum_k \frac{1}{r_{jk}^6} + \frac{4}{15} \gamma_i^2 \gamma_S^2 h^2 S(S+1) \sum_k \frac{1}{r_{jk}^6} \quad (29)$$

where γ_i , h , I , S , and r_{jk} are the gyromagnetic ratio of atoms, the Planck's constant, resonant nuclear spin, nonresonant nuclear spin, and the distance between nuclei, respectively. The diffusion pathway of Li ions in the framework is obtained by ssNMR combining the maximum entropy method. Large linewidths induced by anisotropic spin interactions are usually observed in ssNMR. Magic angle spinning is applied in ssNMR to remove anisotropic interactions, and improve resolution.

Neutrons can interact with nuclei via elastic and inelastic scattering. Quasi-elastic neutron scattering (QENS) denotes the situation that the collisions between neutrons and nuclei exhibit small energy transfer (usually ± 2 meV).⁸⁷ The intensity of scattered neutrons as a function of momentum transfer and energy transfer is collected to determine the peak width of the elastic scattering function. The jump distance and jump frequency of Li ions are further determined based on the Chudley–Elliott model,⁸⁸

$$\Delta\Gamma(Q) = \frac{1}{\tau} \left[1 - \frac{\sin(Qa)}{Qa} \right] \quad (30)$$

in which $\Delta\Gamma$, Q , τ^{-1} , and a are the half-width at half-maximum of the scattering function, momentum transfer, jump frequency, and jump distance, respectively.

The muon (μ) is an elementary particle with a charge of e^- and a spin of $\frac{1}{2}$. It is sensitive to the local atomic environment, which can be used to probe Li transports. Muon spin relaxation ($\mu^+\text{SR}$) is a characterization technique to implant spin-polarized muons in samples and detect the effect of atomic structures on the spin motion of muons.⁸⁹ The random diffusion coefficient D_r by muons is expressed as⁹⁰

$$D_r = \sum_i \frac{1}{N_i} Z_{v,i} a_i^2 v \quad (31)$$

in which N_i , $Z_{v,i}$, a_i , and v are the number of neighboring lattice sites in the i th ion jump path, vacancy fraction of the targeted sites, jump distance, and fluctuation rate, respectively. The diffusion coefficient of Li ions is further determined by the analysis of the perturbation of implanted muons.

3 | Li TRANSPORT MECHANISM

The Li transport mechanisms in SSBMs are summarized in this section. The structural, atomic, and electronic origins of fast Li transports are further interpreted. First, the diffusion mechanisms in solids are introduced in Section 3.1. Second, a quantitative description of diffusion in solids is formulated in Section 3.2. Third, the Li transports in intercalating-type electrodes, conversion-type electrodes, and SEs are discussed in Sections 3.3, 3.4, and 3.5, respectively. Finally, the Li transports at interfaces are interpreted in Section 3.6.

3.1 | Diffusion mechanism in solids

The atomic diffusions in solids are fundamentally connected with defects. Diffusion mechanisms in solids are divided into direct exchange mechanism, interstitial mechanism, vacancy mechanism, Zener ring mechanism, interstitialcy mechanism, crowdion mechanism, etc. (Figure 4).

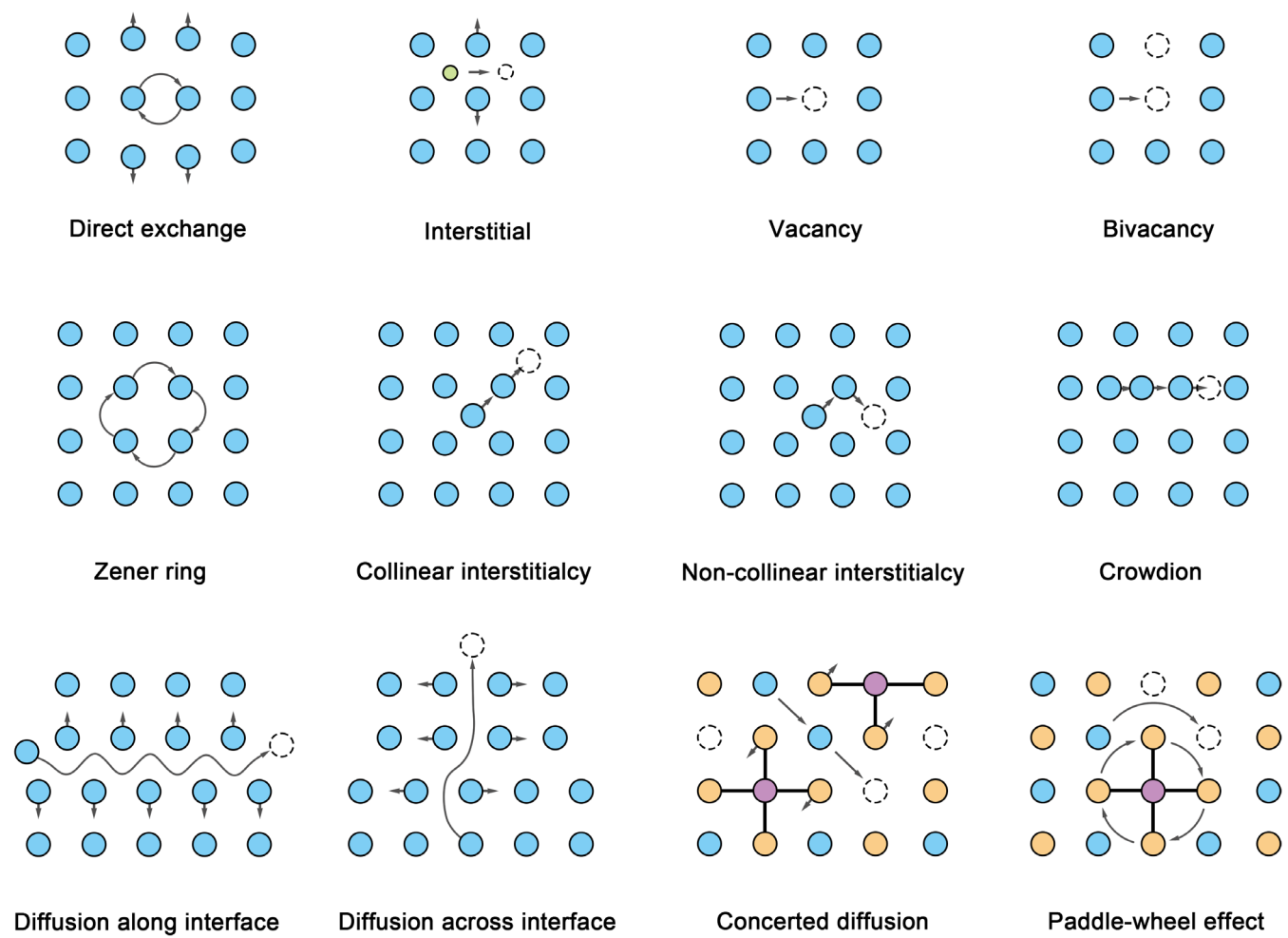


FIGURE 4 Diffusion mechanisms in solids

3.1.1 | Direct exchange mechanism

The direct exchange mechanism is an ideal model in defect-free crystalline solids, which was proposed to interpret the diffusion of gold in solids by Roberts-Austen in 1896.⁹¹ However, such a conceptually simple hypothesis is ruled out due to an ultrahigh activation energy.

3.1.2 | Interstitial mechanism

Light atoms such as hydrogen, carbon, nitrogen, and oxygen usually occupy the interstitial sites in metals. They jump between interstitial sites without the help of intrinsic point defects, contributing to a much higher diffusion coefficient than substitutional atoms.

3.1.3 | Vacancy/bivacancy mechanism

Vacancies inevitably exist in crystals due to thermal movement. Vacancies usually act as diffusion vehicles in atomic diffusion in metals, alloys, and ionic compounds. In addition, vacancy pairs also serve as diffusion vehicles. Such a diffusion mechanism is called the bivacancy mechanism, which has been proposed in LiCoO₂⁹² and LiTiS₂.⁹³

3.1.4 | Zener ring

Collective diffusion mechanisms sometimes significantly decrease the activation energy of ionic motion compared with a single-atom hop, which has been originally discussed in supercooled liquids and glasses.^{94,95} Inspired by the direct exchange mechanism, Zener proposed a ring diffusion mechanism in 1950 to understand the diffusion mechanism in metals.⁹⁶

3.1.5 | Knock-off mechanism

An interstitial atom can move to an adjacent host lattice site, accompanied by the atom in the host site moving to another interstitial site simultaneously. Such the diffusion mechanism is called the knock-off mechanism, which is further divided into collinear and non-collinear interstitialcy by the collinearity of the motion of the two atoms. The Li-ion diffusion in Li_2CO_3 was successfully explained by the knock-off mechanism.⁹⁷

3.1.6 | Crowdion mechanism

A crowdion is a postulated low-temperature configuration of interstitials in face-centered cubic (FCC) metals, in which a host site is occupied by two atoms. One of the two atoms in the host site can diffuse into another host site occupied by an atom. Such the diffusion mechanism is called the crowdion mechanism.

3.1.7 | Short-circuit diffusion

1D and 2D defects including dislocation lines, dislocation walls, grain boundaries, and phase boundaries are regarded as the short circuits in materials. The diffusion mechanism in the short circuits is different from that in lattices because of the special atomic environment in the short circuits. It is generally considered that the diffusion along interfaces is faster than that across interfaces, which has been demonstrated in SE Li_3OCl ⁹⁸ and cathode material $\text{LiNi}_{0.5}\text{Mn}_{0.3}\text{Co}_{0.2}\text{O}_2$.⁹⁹

3.1.8 | Concerted diffusion

Concerted diffusion is a collective movement behavior composed of two or more atoms. It usually appears in the crystalline lattice with partial occupancies of atoms. The atoms at high-energy sites go downhill in concerted diffusion, accompanied by the atoms at low-energy sites going uphill simultaneously, which results in a lower diffusion barrier than single-ion migrations.¹⁰⁰

3.1.9 | Paddle-wheel effect

The paddle-wheel effect is a cooperative movement, in which the rotation of groups in crystalline structures drives the movement of the surrounding atoms. It has been predicted in many SEs with groups of SO_4^{2-} , WO_4^{3-} , $\text{N}_x\text{O}_y^{z-}$, CO_3^{2-} , SiF_6^{2-} , AlF_6^{3-} , PO_4^{3-} , PS_4^{3-} , SbS_4^{3-} , BH_4^- , $\text{XCl}_6^{2-/3-}$ ($\text{X} = \text{Zr}$ or Y), and BF_4^- .¹⁰¹

3.2 | Quantitative description of diffusion in solids

Independent hops of diffusion vehicles follow a random-walk model.¹⁰² The corresponding diffusion coefficient is defined as the random diffusion coefficient D_r , complying with the Einstein-Smoluchowski equation,

$$D_r = \frac{\langle [\mathbf{r}(t)]^2 \rangle}{2dt} = \frac{a^2 v}{2d} \quad (32)$$

where $\langle [\mathbf{r}(t)]^2 \rangle$, d , t , a , and v are the MSD of mobile ions, diffusion dimensionality, time, diffusion distance, and the jump frequency of successful jumps, respectively. The jump frequency v is expressed as follows:²⁸

$$v = v_0 \exp\left(-\frac{G_m}{k_B T}\right) = v_0 \exp\left(\frac{S_m}{k_B}\right) \exp\left(-\frac{H_m}{k_B T}\right) \quad (33)$$

where v_0 , k_B , T , G_m , S_m , and H_m are attempt frequency, the Boltzmann constant, temperature, the Gibbs free energy of migration, migration entropy, and migration enthalpy, respectively. The random diffusion coefficient D_r is further integrated into

$$D_r = \frac{a^2}{2d} v_0 \exp\left(\frac{S_m}{k_B}\right) \exp\left(-\frac{H_m}{k_B T}\right). \quad (34)$$

If only thermally activated intrinsic defects are considered, the defect concentration in thermal equilibrium C is equal to

$$C = N \exp\left(-\frac{G_F}{k_B T}\right) = N \exp\left(\frac{S_F}{k_B}\right) \exp\left(-\frac{H_F}{k_B T}\right) \quad (35)$$

where N , G_F , S_F , and H_F are the number of the working sites per unit volume, the Gibbs free energy of defect formation, defect formation entropy, and defect formation enthalpy, respectively. The tracer diffusion coefficient D^* is further given by,

$$D^* = g f C D_r = \frac{g f N a^2 v_0}{2d} \exp\left(\frac{S_F + S_m}{k_B}\right) \exp\left(-\frac{H_F + H_m}{k_B T}\right) = D_0 \exp\left(-\frac{H_a}{k_B T}\right) \quad (36)$$

where D_0 , H_a , g , and f are the pre-exponential factor, activation enthalpy (approx. Activation energy E_a at the ambient condition), geometrical factor, and correlation factor, respectively. When extrinsic defects are introduced by doping, their concentration is usually far more than that of intrinsic defects. The activation energy E_a , in this case, is approximated as the migration energy E_m ,

$$E_a \approx E_m \quad (37)$$

$$D^* \approx D_r = \frac{a^2}{2d} v_0 \exp\left(\frac{S_m}{k_B}\right) \exp\left(-\frac{H_m}{k_B T}\right). \quad (38)$$

The charge diffusion coefficient D_σ is defined by the equation

$$D_\sigma = \frac{k_B T}{c q^2} \sigma \quad (39)$$

where c , q , and σ are carrier concentration, ionic charge, and ionic conductivity, respectively. The Haven ratio H_R evaluates the correlation effect of ionic motions

$$H_R = \frac{D^*}{D_\sigma}. \quad (40)$$

3.3 | Diffusion in intercalating-type electrodes

Intercalation and deintercalation reactions take place at intercalating-type electrodes by solid-state diffusions. A sluggish solid-state diffusion dynamics severely limit rate performances of intercalating-type electrodes, especially for the batteries in the low-temperature or fast-charging operating conditions.¹⁰³ Diffusion coefficients in intercalating-type electrodes not only depend on the diffusion pathways in crystalline structures but also are affected by changed Li-ion concentrations. The detailed discussion is conducted based on the intercalating-type electrodes including layered graphite, Li_xCoO_2 , $\text{Li}(\text{Ni}_x\text{Co}_y\text{Mn}_z)\text{O}_2$, olivine LiFePO_4 , and spinel $\text{Li}_4\text{Ti}_5\text{O}_{12}$. Note that only thermal diffusion is considered. The grand canonical ensemble needs to be introduced regarding chemical diffusions driven by Li concentration differences.¹⁰⁴

Graphite is an anode material delivering a low average voltage of 0.1 V versus Li/Li^+ and a high theoretical specific capacity of 372 mAh g⁻¹, which was first reported by Yazami and Touzain in 1983.¹⁰⁵ It is the large-scale utilization of graphite electrodes that drives the commercialization of Li-ion batteries. It is generally believed that continuous discharge platforms correspond to LiC_6 , LiC_{12} , and LiC_{24} (stages I–III) with a spontaneous stacking sequence transition from AB to AA.^{106–108} The atomistic modeling regarding the Li diffusion in graphite is plagued by the structural complexity of intermediate configurations, which has been elaborately addressed by a combination of *ab initio* calculations and disordered structure generation methods such as cluster expansions¹⁰⁹ or group–subgroup transformation (Figure 5a).¹¹⁰ Activation energy of 283 and 297 meV was determined for states I and II, respectively.¹⁰⁹ Tracer diffusion coefficients of 10^{-8} – 10^{-11} cm² s⁻¹ were further derived (Figure 5b), in agreement with the experimental results ranging from 10^{-7} to 10^{-14} cm² s⁻¹.^{111–113} The diffusion coefficient is dominated by the in-plane Li-ion concentration and the Li–Li electrostatic interactions rather than the interlayer coupling effect.

Cathode material LiCoO_2 exhibits an average voltage of 3.9 V versus Li/Li^+ and a theoretical specific capacity of 274 mAh g⁻¹, which was first synthesized by Johnston et al. in 1958¹¹⁵ and was introduced into energy storage application by Mizushima et al. in 1980.¹¹⁶ Similar to graphite, the structural complexity of intermediate configurations during charging and discharging is a stumbling block for understanding the underlying Li transport mechanism. The phase transition between O₃-type $\text{Li}_{0.75}\text{CoO}_2$ and spinel $\text{Li}_{0.5}\text{CoO}_2$ ^{117–119} further enhances the difficulty to determine the intermediate structures. A series of ground-state configurations were determined by cluster expansions,¹²⁰ similar to the procedure implemented in graphite. DFT calculations indicate that a divacancy diffusion mechanism is energetically favorable for Li transports in Li_xCoO_2 . The activation energy in Li_xCO_2 decreases from 610 to 210 meV with an increasing Li content from 0 to 1, in agreement with the results determined by a kinetic Monte Carlo simulation and PITT measure,^{92,121,122} which is attributed to the change in the c lattice parameter and effective valence of the Co ions.^{120,123} A diffusion coefficient of 1.19×10^{-13} – 1.27×10^{-11} cm² s⁻¹ was further determined by the PITT measure.¹²²

The significant capacity fading in LiCoO_2 under cycling and low abundance of Co promotes the explorations of the LiMO₂ with different transition metal M in electrode material applications.¹²⁴ LiNiO₂ exhibits a comparable theoretical specific capacity (275 mAh g⁻¹) to LiCoO_2 , while it suffers from poor cycling performance induced by a structural change. Such the structural change corresponds to the movements of Ni ions from transition metal layers to Li layers, stemming from the similar ionic radii of Li^+ and Ni^{2+} ions.¹²⁵ The research interest in LiMnO₂ benefits from the low price of Mn and a similar theoretical specific capacity (285 mAh g⁻¹).¹²⁶ The practical application of LiMnO₂ is also impeded by a transition from layer phase to spinel phase. A mixing strategy has been proposed to further improve the electrochemical properties of LiMO₂, such as combinations of Ni, Co, and Mn (NCM), and of Ni, Co, and Al (NCA).¹²⁷ The predicted activation energy in $\text{Li}(\text{Ni}_x\text{Co}_y\text{Mn}_z)\text{O}_2$ depends on the transition metal ions adjacent to mobile Li ions, for example, 357, 430, 545, 510, and 523 meV for the Li ions around Ni^{2+} , Ni^{3+} , Ni^{4+} , Co^{3+} , and Mn^{4+} , respectively.¹²⁸ An increasing diffusion coefficient from 10^{-9} to 10^{-7} cm² s⁻¹ is predicted with an increasing Ni content regardless of the state of charge, in agreement with the experimental measurements.¹²⁸

Intercalation and deintercalation of Li ions in LiFePO_4 and $\text{Li}_4\text{Ti}_5\text{O}_{12}$ exhibit a typical two-phase reaction with a flat voltage plateau.¹²⁹ Cathode material LiFePO_4 delivers an average voltage of 3.45 V versus Li/Li^+ and a theoretical specific capacity of 170 mAh g⁻¹.¹²⁹ The 1D Li transport channel along the [010] direction was predicted by DFT calculation with the NEB method (Figure 5c). Activation energy of 190 and 290 meV was further determined for Li_xFePO_4 with $x = 0$ and 1, respectively (Figure 5d).¹⁰² However, the 1D Li diffusion channel cannot support fast Li transports at the macroscopic level owing to the inevitable channel blocking defects.¹³⁰ Subsequently, Fe-ion migrations in the framework and antisite defect formation were verified by AIMD simulations¹³¹ and neutron powder diffraction experiments (Figure 5c).¹³² A new octahedron–tetrahedron–octahedron Li diffusion pathway was proposed. The experimental value (10^{-13} – 10^{-14} cm² s⁻¹)¹³³ of the diffusion coefficient in LiFePO_4 is 4–6 orders

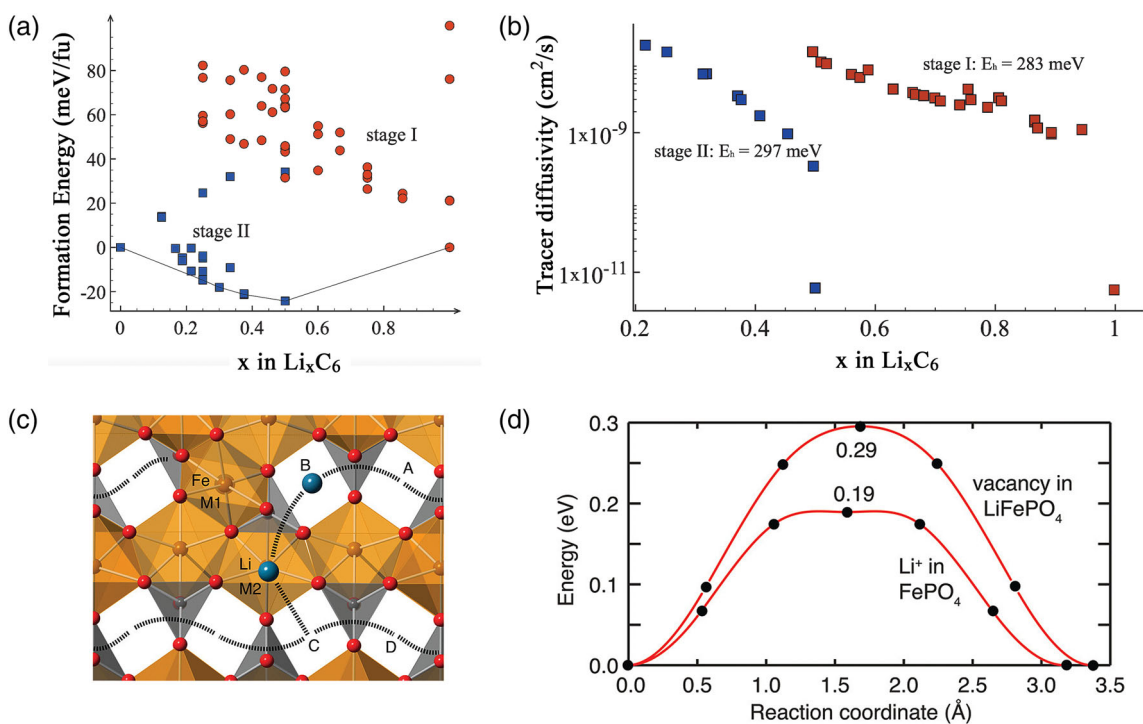


FIGURE 5 The Li migration in intercalating-type electrodes. (a) Predicted ground states and (b) diffusion coefficients of lithiation graphite Li_xC . Reprinted with permission from Reference 109. Copyright[©] 2010 American Physical Society. (c) The antisite defect is composed of Fe at site M1 and Li at site M2 in Li_xFePO_4 . (d) Migration energy profiles for Li-ion hopping in FePO_4 and Li-vacancy hopping in LiFePO_4 . Reprinted with permission from Reference 114. Copyright[©] 2011 American Chemical Society

of magnitude lower than the theoretical prediction (10^{-7} – $10^{-8} \text{ cm}^2 \text{ s}^{-1}$),^{114,134} which is attributed to the effect of defects and interfaces in samples.

Anode material $\text{Li}_4\text{Ti}_5\text{O}_{12}$ possesses an average voltage of 1.5 V versus Li/Li^+ and a theoretical specific capacity of 175 mAh g⁻¹, featuring zero-strain characteristics (a varied volume of 0.2%) during charging and discharging.^{135,136} The spinel $\text{Li}_4\text{Ti}_5\text{O}_{12}$ transforms into rock-salt $\text{Li}_7\text{Ti}_5\text{O}_{12}$ with the Li-ion insertion.¹³⁷ Activation energy of 0.30–0.48 and 0.20–0.51 eV was predicted for $\text{Li}_4\text{Ti}_5\text{O}_{12}$ and $\text{Li}_7\text{Ti}_5\text{O}_{12}$, respectively, depending on the local chemical environment.¹³⁸ A diffusion coefficient of $(1.15\text{--}6.8) \times 10^{-11} \text{ cm}^2 \text{ s}^{-1}$ was measured by $\mu^+\text{SR}$ spectroscopy,¹³⁹ cyclic voltammetry (CV),^{140,141} and PITT.¹⁴⁰ Superior fast-charging performance in $\text{Li}_4\text{Ti}_5\text{O}_{12}$ has recently been reported, which is ascribed to the fast Li transport channel in metastable intermediates $\text{Li}_{5+\delta}\text{Ti}_5\text{O}_{12}$.¹⁴² NEB calculations predict that the activation energy (216 meV) in $\text{Li}_{5+\delta}\text{Ti}_5\text{O}_{12}$ is lower than those (343 and 455 meV) in $\text{Li}_{4+\delta}\text{Ti}_5\text{O}_{12}$ and $\text{Li}_{7-\delta}\text{Ti}_5\text{O}_{12}$, in agreement with NMR measurements¹⁴³ and AIMD simulations.¹⁴⁴

3.4 | Diffusion in conversion-type electrodes

Compared to the limited capacity of intercalating-type electrodes, alloying-type and conversion-type electrodes deliver higher capacities through conversion reactions. It is extremely challenging to accurately determine the crystalline structures during conversion-type electrode operations. Only Li metal and alloys are briefly discussed to probe the Li transports in conversion-type electrodes.

Li metal is a special conversion-type electrode, which exhibits the highest theoretical specific capacity of 3860 mAh g⁻¹ and a very negative reduction potential of −3.04 V versus standard hydrogen electrode.^{145,146} Vacancy mechanism is the dominant diffusion mechanism in bulk Li metal, similar to other metallic crystals.¹⁴⁷ Although the migration energy of a vacancy in Li metal is 55 meV, much lower than those in the intercalating-type electrodes, a high vacancy formation energy (520 meV) at ambient conditions contributes to a high activation energy (575 meV).¹⁴⁷ A diffusion coefficient of $(1\text{--}10) \times 10^{-11} \text{ cm}^2 \text{ s}^{-1}$ was further determined,¹⁴⁷ in agreement with the experimental results of about

$5\text{--}9 \times 10^{-11} \text{ cm}^2 \text{ s}^{-1}$.^{148–152} The low diffusion coefficient leads to the difficulty in the mass transport in Li metal, which is responsible for the morphological change at SE/Li metal interfaces (e.g., vacancy accumulation and macroscopic pore formation) and an increasing interface resistance in SSBs.¹⁵³ Various strategies including applying external stack pressures,¹⁵⁴ designing 3D interfaces,^{155,156} and utilizing alloy anodes^{157,158} have been proposed to eliminate the dynamical morphological degradations at SE/Li interfaces.

Alloy anode materials including Li–Mg,^{157,159} Li–Si,¹⁶⁰ Li–Ge,¹⁶¹ Li–Sn,^{162,163} Li–In,¹⁶⁴ Li–Sb,¹⁶² Li–Al,¹⁶⁵ Li–Zn,^{162,166} Li–Bi,¹⁶² Li–Pb,¹⁶² Li–Au,¹⁶⁷ Li–Ag,¹⁶⁸ and Li–Pt¹⁶⁹ are believed to effectively increase diffusion coefficients compared with Li metal, at the expense of reduced theoretical specific capacities (ca. $<1000 \text{ mAh g}^{-1}$) except for Li–Mg (3350 mAh g^{-1}) and Li–Si (4200 mAh g^{-1}). Since Li and Mg form a stable β -phase within a wide composition range at the Li-rich side, Li-rich Li–Mg alloy is an ideal research system to probe the Li dynamics in alloys. The intrinsic diffusion coefficients in Li-rich Li–Mg alloy ($\text{Li}_{0.9}\text{Mg}_{0.1}$) and Li metal have been identified as 2.3×10^{-11} and $0.8 \times 10^{-11} \text{ cm}^2 \text{ s}^{-1}$, respectively, by operando galvanostatic electrochemical impedance spectroscopy (GEIS),¹⁵⁷ which fails to explain the difference in Li kinetics between alloy and Li metal electrodes. The nonequilibrium defect concentrations in the alloy and Li metal anodes are further considered to dominantly affect Li diffusion coefficients, which is responsible for the highly varied diffusion coefficients in Li–Mg alloy ranging from 10^{-11} to $10^{-7} \text{ cm}^2 \text{ s}^{-1}$. The migration energy of diffusion vehicles in Li–Sn and Li–In alloy crystalline structures with different Li contents has been determined by the NEB method.¹⁷⁰ Interstitial- and vacancy-based collective diffusion mechanisms including knock-off and coordinate exchange have been proposed with migration energy of 110–490 and 15–260 meV for Li–Sn and Li–In alloys, respectively (Figure 6).¹⁷⁰ However, it is challenging to experimentally probe the Li transports in Li–Sn and Li–In alloys because of continuous phase transitions of the alloys during electrode operations.

3.5 | Diffusion in solid electrolytes

The safety concern regarding flammable liquid electrolytes stimulates the rapid development of SEs. Carrying the SEs with high ionic conductivities is one of the prerequisites for the practical design of SSBs. Therefore, it is of essential importance to understand the Li transport mechanisms in SEs. Inorganic solid electrolyte materials contain sulfides (e.g., thiophosphates $\text{Li}_{10}\text{GePS}_{12}$ (LGPS),¹⁷¹ glass-ceramics Li_3PS_4 and $\text{Li}_7\text{P}_3\text{S}_{11}$,^{172,173} and argyrodite $\text{Li}_6\text{PS}_5\text{Cl}$ (LPSCl)),¹⁷⁴ oxides (e.g., garnet $\text{Li}_7\text{La}_3\text{Zr}_2\text{O}_{12}$ (LLZO),¹⁷⁵ NASICON $\text{Li}_{1.5}\text{Al}_{0.5}\text{Ti}_{1.5}(\text{PO}_4)_3$ (LATP),¹⁷⁶ and perovskite $\text{Li}_{0.5}\text{La}_{0.5}\text{TiO}_3$ (LLTO)),¹⁷⁷ halides (e.g., Li_3YCl_6),¹⁷⁸ and nitrides (e.g., Li_3N and LiPON). The diffusion-related physical quantities including activation energy, diffusion coefficients, and ionic conductivities in SEs are summarized (Table 1). The detailed Li transport behaviors in SEs have been comprehensively discussed by several high-impact reviews.^{28,179–182} Herein, only several insights regarding the Li transport mechanisms in SEs are discussed.

3.5.1 | Concerted diffusion

The lattice structures of SEs comprise mobile Li ions and anionic frameworks. Li ions are disorderly distributed in certain crystallographic sites, contributing to partial occupancy of high-energy sites. Compared to individual jumps of the Li ions at low-energy sites, the collective motions of the Li ions at low- and high-energy sites, that is, concerted diffusion, exhibit lower migration energy.¹⁸³ Such a result is attributed to the compromise between the downhill of Li ions at high-energy sites and the uphill of Li ions at low-energy sites on the PES (Figure 7). The activation energies (0.20 and 0.26 eV) of the multi-ion concerted diffusions in LGPS and LLZO are much lower than those (0.47 and 0.58 eV) of the single-ion jumps.¹⁰⁰ An intuitive theoretical diffusion model was proposed in this work by Mo et al., in which an extra Coulomb term is appended to the lattice potential. The decreased activation energy induced by the concerted diffusion is reproduced by employing the model. The Coulomb term effectively describes the Li–Li interactions, which are considered as the origin of concerted diffusion. The work provides a very important insight to understand the concerted diffusion.

3.5.2 | Paddle–wheel effect

In addition to concerted diffusions induced by Li–Li interactions, the coupling between Li and anionic frameworks, that is, the paddle–wheel effect, is also proposed to be an origin of fast Li-ion transports in certain SEs.¹⁸⁵ In the scenario of

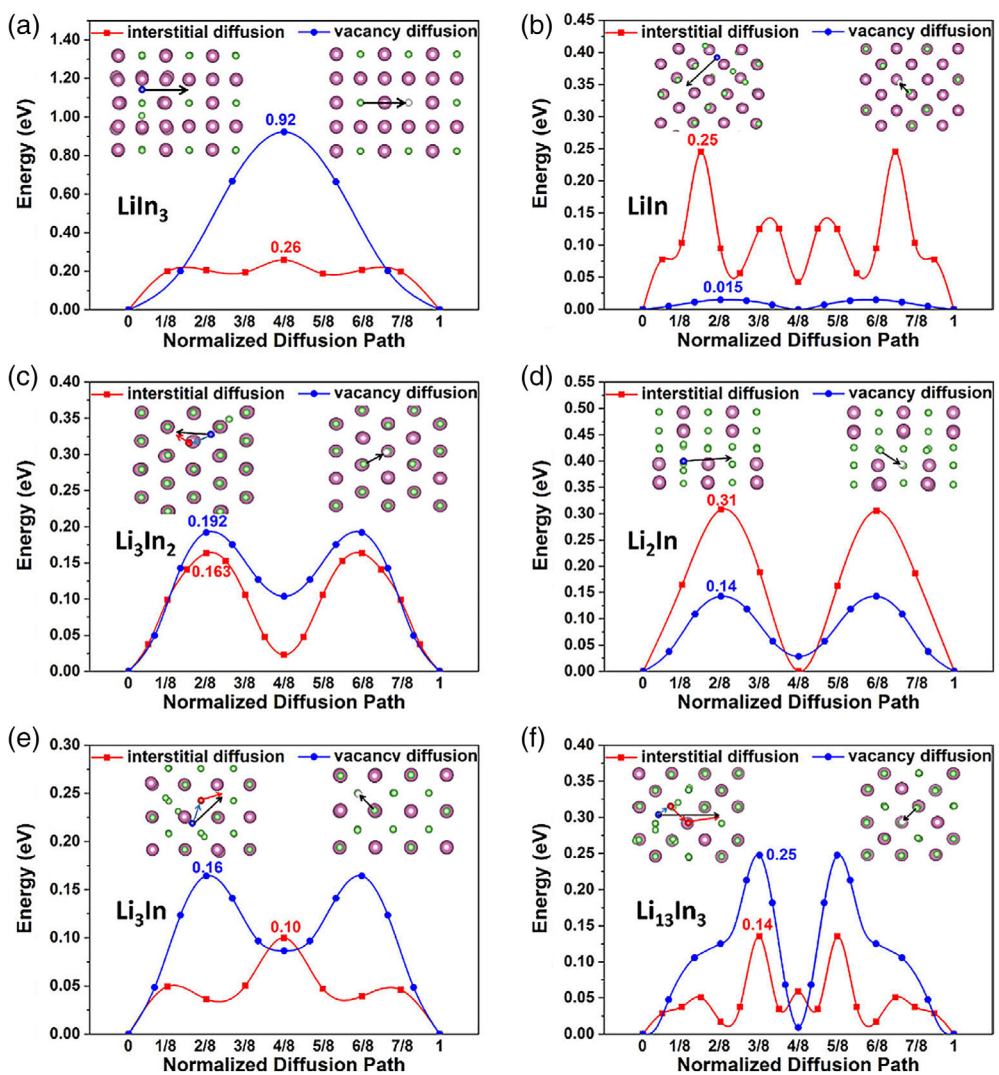


FIGURE 6 The Li migration pathways and corresponding migration energy profiles for (a) LiIn_3 , (b) LiIn , (c) Li_3In_2 , (d) Li_2In , (e) Li_3In , and (f) $\text{Li}_{13}\text{In}_3$. Reprinted with permission from Reference 170. Copyright[©] 2020 American Chemical Society

the paddle-wheel effect, Li-ion transport is facilitated by the rotation of anionic frameworks (Figure 8),¹⁰¹ which is somewhat similar to the transport of people through a multi-people revolving door. Such a mechanism has been used to explain the fast Li-ion transports at room temperature in glassy $\text{Li}_7\text{P}_3\text{S}_{11}$,¹⁸⁴ $\beta\text{-Li}_3\text{PS}_4$,¹⁸⁶ $\text{Li}_{3.25}\text{Si}_{0.25}\text{P}_{0.75}\text{S}_4$,¹⁸⁶ $\text{Li}_6\text{PS}_5\text{X}$ ($\text{X} = \text{Cl}, \text{Br}, \text{and I}$),¹⁸⁷ LiBF_4 ,¹⁸⁸ and Li_2BF_5 .¹⁸⁸ The paddle-wheel effect in glassy $\text{Li}_7\text{P}_3\text{S}_{11}$ is attributed to the similar vibration frequency distributions of Li ions and anions and similar activation energies (0.27 and 0.22 eV) of PS_4 rotation and Li translation. Very recently, Li et al. performed a brilliant theoretical investigation to understand the paddle-wheel effect.¹⁸⁸ The cation-anion interactions in SEs are further divided into vibrational- and rotational-type couplings by the motions of anion frameworks. A new anion framework BF_4^- is screened out based on its low rotation energy barriers. The compounds with the anion framework BF_4^- , LiBF_4 , and Li_2BF_5 , exhibit two different Li diffusion behaviors. The Li ions in the two diffusion modes migrate with the assistance of the vibration and rotation modes of BF_4^- , respectively. Such an investigation enriches the cognition of the paddle-wheel effect and proposes fresh ideas for designing new SEs.

3.5.3 | Lattice dynamics

Atoms vibrate around their equilibrium position according to lattice dynamics theory, similar to harmonic oscillators. The atomic transport is considered as a special vibration process, in which the atom escapes from the original potential

TABLE 1 Comparison in activation energy E_a , diffusion coefficients D , and ionic conductivities σ determined by experimental and computational methods

Species	$E_a(\text{exp}) \text{ (eV)}$	$E_a(\text{cal}) \text{ (eV)}$	$D(\text{exp}) \text{ (cm}^2 \text{ s}^{-1}\text{)}$	$D(\text{cal}) \text{ (cm}^2 \text{ s}^{-1}\text{)}$	$\sigma(\text{exp}) \text{ (mS cm}^{-1}\text{)}$	$\sigma(\text{cal}) \text{ (mS cm}^{-1}\text{)}$
<i>Anode</i>						
Li	0.52–0.57 [148–152]	0.575 [147]	(5–9) $\times 10^{-11}$ [148–152]	(1–10) $\times 10^{-11}$ [147]		
LiC_6	0.27–0.55 [221,222]	0.283 [109]	(3.8–7.6) $\times 10^{-11}$ [221–223]	9 $\times 10^{-12}$ [109]		
LiC_{12}	0.17 [222]	0.297 [109]	1.46 $\times 10^{-10}$ [222]	9 $\times 10^{-12}$ [109]		
$\text{Li}_4\text{Ti}_5\text{O}_{12}$	0.2–0.48 [138,224]		(1.15–6.8) $\times 10^{-11}$ [139–141]		5.96 $\times 10^{-4}$ [224]	
SEI						
LiF	1.99 [215]	2.03 [225]	3.5 $\times 10^{-16}$ [226]	10 $^{-11}$ –10 $^{-6}$ [227–229]	10 $^{-28}$ –10 $^{-4}$ [225,230]	
LiCl	1.47 [215]					
LiBr	1.29 [215]					
LiI	1.05 [215]					
Li_2O	0.86 [216]					
Li_2S	0.90 [231]					
Li_3N	0.41–0.43 (ab) [232,233], 0.68 (c) [232]		2.53 $\times 10^{-13}$ (ab) [232], 3.49 $\times 10^{-10}$ (c) [232]		0.16–0.58 [233,234]	
Li_2CO_3		0.67 [97]			1.1 $\times 10^{-7}$ [97]	
<i>Sulfide electrolyte</i>						
$\text{Li}_{3.25}\text{Ge}_{0.25}\text{P}_{0.75}\text{S}_4$	0.21 [235]				2.17 [235]	
$\text{Li}_{3.4}\text{Si}_{0.4}\text{P}_{0.6}\text{S}_4$	0.5–0.6 [236]				0.64 [236]	
$\text{Li}_7\text{P}_3\text{S}_{11}$	0.18 [173]				17 [173]	
$\beta\text{-Li}_3\text{PS}_4$	0.16 [237]				0.3 [237]	
$\gamma\text{-Li}_3\text{PS}_4$	0.22 [237]					
Amorphous Li_3PS_4	0.35 [238]				0.2 [238]	
$\text{Li}_{10}\text{GeP}_2\text{S}_{12}$	0.21–0.24 [171,239]		0.22–0.23 [100,240]	2.20 $\times 10^{-8}$ [239]	1.00 $\times 10^{-7}$ [240]	12 [171]
Li_7GePS_8	0.23 [239]			1.80 $\times 10^{-8}$ [239]		10 $^{-13}$ [100,240]
$\text{Li}_9\text{P}_3\text{S}_{12}$						
$\text{Li}_{11}\text{AlP}_2\text{S}_{12}$	0.26 [240]				6 [240]	
$\text{Li}_{11}\text{Si}_2\text{PS}_{12}$	0.18 [240]					33 [240]
$\text{Li}_{10}\text{SnP}_2\text{S}_{12}$	0.19 [242]					4 [240]
$\text{Li}_{10}\text{SiP}_2\text{S}_{12}$	0.23–0.27 [241,242]	0.24 [240]	1.4–1.8 $\times 10^{-8}$ [241,242]	4.40 $\times 10^{-8}$ [240]	7 [241]	
$\text{Li}_{10}\text{GeP}_2\text{Se}_{12}$	0.2 [240]				1.90 $\times 10^{-7}$ [240]	
$\text{Li}_{9.54}\text{Si}_{1.74}\text{P}_{1.44}\text{S}_{11.7}\text{Cl}_{0.3}$	0.19 [240]					23 [240]
						25 [243]

TABLE 1 (Continued)

Species	$E_a(\text{exp})$ (eV)	$E_a(\text{cal})$ (eV)	$D(\text{exp})$ ($\text{cm}^2 \text{s}^{-1}$)	$D(\text{cal})$ ($\text{cm}^2 \text{s}^{-1}$)	$\sigma(\text{exp})$ (mS cm^{-1})	$\sigma(\text{cal})$ (mS cm^{-1})
$\text{Li}_6\text{PS}_5\text{Cl}$	0.33 [244]				0.62–2.4 [244,245]	
$\text{Li}_6\text{PS}_5\text{Br}$	0.3–0.4 [244]				0.46–1.9 [244,245]	
$\text{Li}_6\text{PS}_5\text{I}$	0.3–0.4 [244]				0.19 [244]	
<i>Oxide electrolyte</i>						
$\text{Li}_{10}\text{GeP}_2\text{O}_{12}$	0.36 [240]				24 [240]	
$\text{Li}_7\text{La}_3\text{Zr}_2\text{O}_{12}$	0.32 [175]	0.25 [100]			0.3 [175]	0.03 [240]
$\text{Li}_5\text{La}_3\text{Bi}_2\text{O}_{12}$	0.47 [246]				5.2×10^{-2} [246]	
$\text{Li}_6\text{SrLa}_2\text{Bi}_2\text{O}_{12}$	0.42 [246]				10^{-3} [247]	
$\text{Li}_5\text{La}_3\text{Nb}_2\text{O}_{12}$	0.43 [247]				10^{-3} [247]	
$\text{Li}_5\text{La}_3\text{Ta}_2\text{O}_{12}$	0.56 [247]				7.0×10^{-3} [248]	
$\text{Li}_6\text{SrLa}_2\text{Ta}_2\text{O}_{12}$	0.50 [248]				$1.3\text{--}4.0 \times 10^{-2}$ [248,249]	
$\text{Li}_6\text{BaLa}_2\text{Ta}_2\text{O}_{12}$	0.40–0.44 [248,249]				1 [250]	
$\text{Li}_6\text{La}_4\text{Zr}_{1.4}\text{Ta}_{0.6}\text{O}_{12}$	0.35 [250]				0.16 [251]	
$\text{Li}_6\text{La}_3\text{Ta}_{1.5}\text{Y}_{0.5}\text{O}_{12}$	0.36 [251]				2.2×10^{-3} [249]	
$\text{Li}_6\text{CaLa}_2\text{Ta}_2\text{O}_{12}$	0.50 [249]				5.0×10^{-2} [252]	
$\text{Li}_6\text{La}_3\text{HfNbO}_{12}$					2.2×10^{-2} [253]	
$\text{Li}_6\text{La}_3\text{SnSbO}_{12}$	0.50 [253]				3.5×10^{-2} [253]	
$\text{Li}_6\text{La}_3\text{NbO}_{12}$	0.50 [253]				4.2×10^{-2} [253]	
$\text{Li}_6\text{La}_3\text{SnTaO}_{12}$	0.50 [253]				0.18 [254]	
$\text{Li}_6\text{La}_3\text{ZrTaO}_{12}$	0.42 [254]				0.15 [255]	
$\text{Li}_6\text{La}_3\text{ZrNbO}_{12}$	0.40 [255]				0.24 [256]	
$\text{Li}_7\text{La}_3\text{Hf}_2\text{O}_{12}$	0.29 [256]				0.20 [257]	
Al-doped $\text{Li}_7\text{La}_3\text{Zr}_2\text{O}_{12}$						
$\text{Li}_{6.25}\text{Ga}_{0.25}\text{La}_3\text{Zr}_2\text{O}_{12}$	0.25 [258]				1.46 [258]	
$\text{Li}_{6.25}\text{La}_3\text{Nb}_{1.375}\text{Sc}_{0.625}\text{O}_{12}$	0.36 [259]				0.37 [259]	
$\text{Li}_{6.5}\text{La}_3\text{Zr}_{1.75}\text{Te}_{0.25}\text{O}_{12}$	0.37 [260]				1.02 [260]	
$\text{Li}_{7.06}\text{La}_3\text{Y}_{0.06}\text{Zr}_{1.94}\text{O}_{12}$	0.26 [261]				0.81 [261]	
$\text{Li}_{1.3}\text{Ti}_{1.7}\text{Al}_{0.3}(\text{PO}_4)_3$	0.25 [100]				1.3 [100]	
$\text{Li}_{1.2}\text{Ti}_{1.8}\text{Al}_{0.2}(\text{PO}_4)_3$	0.22–0.28 [262]				1.1 [100]	
$\text{Li}_{2.88}\text{PO}_{3.73}\text{N}_{0.14}$	0.45–0.55 [263]				3.3×10^{-3} [263]	
$\text{LiHf}_2(\text{PO}_4)_3$	0.33 [195]				1.3×10^{-2} [195]	

(Continues)

TABLE 1 (Continued)

Species	$E_a(\text{exp})$ (eV)	$E_a(\text{cal})$ (eV)	$D(\text{exp})$ ($\text{cm}^2 \text{s}^{-1}$)	$D(\text{cal})$ ($\text{cm}^2 \text{s}^{-1}$)	$\sigma(\text{exp})$ (mS cm^{-1})	$\sigma(\text{cal})$ (mS cm^{-1})
<i>Halide electrolyte</i>						
Li_3InCl_6	0.326–0.347 [266,267]	0.20 [268]	1.49–2.04 [266,267]	6–21 [268–270]		
Li_3ErCl_6	0.41 [271]	0.31 [271]				
Li_3YCl_6	0.40–0.45 [271,272]	0.19 [272]	(0.95–5) $\times 10^{-1}$ [271,272]	14 [272]		
Li_3YBr_6	0.37 [272]	0.28 [272]	1.7 [272]	2.2 [272]		
LiScCl_4	0.39 [273]	0.37 [273]	0.12 [273]	1.8 $\times 10^{-2}$ [273]		
$\text{Li}_{1.5}\text{ScCl}_{4.5}$	0.38 [273]	0.24 [273]				
$\text{Li}_{1.8}\text{ScCl}_{4.8}$	0.34 [273]	4.4 $\times 10^{-2}$ [273]				
Li_2ScCl_5	0.38 [273]	0.62 [273]				
$\text{Li}_{2.5}\text{ScCl}_{5.5}$	0.37 [273]	2.5 [273]				
Li_3ScCl_6	0.36 [273]	3.0 [273]	5.1–29 [268,272,273]			
$\text{Li}_{3.5}\text{ScCl}_{6.5}$	0.36 [273]	2.4 [273]				
Li_4ScCl_7	0.38 [273]	1.9 [273]				
Li_5ScCl_8	0.26 [273]	2.4 [273]				
Li_3ScBr_6	0.30 [272]	1.4 [272]				
Li_3HoCl_6	0.19 [272]	21 [272]				
Li_3HoBr_6	0.26 [272]	3.8 [272]				
$\text{Li}_{2.5}\text{In}_{0.5}\text{Zr}_{10.5}\text{Cl}_6$	0.20 [268]	27 [268]				
$\text{Li}_{2.5}\text{Sc}_{0.5}\text{Zr}_{10.5}\text{Cl}_6$	0.16 [268]	89 [268]				
LiAlCl_4	0.47–0.50 [274–276]	(2.1–2.9) $\times 10^{-2}$ [274,275]				
LiAlBr_4	0.437 [274]	3.3 $\times 10^{-2}$ [274]				
LiAlI_4	0.429 [274]	1.2 $\times 10^{-2}$ [274]				
$\text{Li}_2\text{Sc}_{2/3}\text{Cl}_4$	0.277 [277]	2.07 [277]				
$\text{Li}_2\text{Sc}_{2/3}\text{Br}_4$	0.366 [277]	0.20 [277]				
$\text{Li}_2\text{Sc}_{2/3}\text{I}_4$	0.257 [277]	2.78 [277]				

TABLE 1 (Continued)

Species	$E_a(\text{exp})$ (eV)	$E_a(\text{cal})$ (eV)	$D(\text{exp})$ ($\text{cm}^2 \text{s}^{-1}$)	$D(\text{cal})$ ($\text{cm}^2 \text{s}^{-1}$)	$\sigma(\text{exp})$ (mS cm^{-1})	$\sigma(\text{cal})$ (mS cm^{-1})
<i>Cathode</i>						
LiCoO_2	0.3 [278]	0.31 [279]	10^{-16} – 10^{-11} [122,278]	7.3×10^{-19} [278]		
LiNiO_2	0.59 [278]					
$\text{Li}_{1.2}\text{Co}_{0.3}\text{Ni}_{0.13}\text{Mn}_{0.54}\text{O}_2$	0.53 [280]					
$\text{Li}_{1.2}\text{Ni}_{0.15}\text{Co}_{0.11}\text{Mn}_{0.55}\text{O}_2$	0.26 [281]					

well to a new one. Since phonon frequencies are an indicator of the strength of interatomic interactions. A low average phonon frequency of Li atoms is related to low activation energy (Figure 9a), which also results in a low attempt frequency. Several specific modes dominantly contributing to the transport of Li ions are further distinguished (Figure 9b), which implies a possible strategy (e.g., phonon–phonon coupling,¹⁸⁹ electron–photon coupling,¹⁹⁰ and THz electric fields¹⁹¹) to manipulate the Li-ion transports from a phonon perspective. A detailed discussion about the effect of phonon on Li transports can be found in a recent review by Zeier et al.,¹⁸² in which the roles of phonon on Li-ion migrations are comprehensively classified into five aspects: (1) the effect of ionic polarizability, (2) the effect of lattice stiffness, (3) the connection between specific phonon frequencies and activation energies, (4) the implication of average phonon frequencies, and (5) the paddle-wheel effect. A high-throughput calculation to search for the promising SE candidates is performed using average phonon frequencies as a descriptor.¹⁹² The close contact between lattice dynamics and Li-ion migrations is being gradually uncovered.

3.5.4 | Crystalline structure

The crystalline structures of SEs exhibit several characteristics, which is critical to ensure fast Li-ion transports. (1) A moderate neck size is beneficial to fast Li-ion transport in SEs. A too strong interaction between Li ions and anionic frameworks is received in SEs with small neck sizes when Li ions move to transition states. Therefore, the strategies to increase neck sizes such as elemental substitution can increase ionic conductivities in some SEs. For example, the substitution of Ga^{4+} and Ti^{4+} with Hf^{4+} in $\text{LiMM}'(\text{PO}_4)_3$ ($\text{M}/\text{M}' = \text{Ga}, \text{Ti}$, and Hf) increase ionic conductivity by up to 4 orders of magnitude.¹⁹⁵ However, too large neck sizes in SEs result in significantly changed Li-site occupancies, which is also unfavorable for fast Li transports. The neck size of common oxide and sulfide SEs falls within the range of 0.54–0.72 Å (Figure 10a,b).¹⁹⁶ (2) A 3D Li-ion diffusion pathway is expected compared with a 1D/2D pathway. 1D diffusion pathway is easily blocked by point defects, for example, the antisite defects induced by the migration of Fe ions in LiFePO_4 .¹³¹ As a consequence, the ionic conductivities of 1D ion conductors exhibit a significant size effect. LGPS is considered as a 1D Li-ion conductor in early research because of the recognizable <001> diffusion channel.¹⁹⁷ The following AIMD¹⁹⁸ and NMR¹⁹⁹ researches indicate the nature of its 3D Li-ion conduction pathway, which is a structural

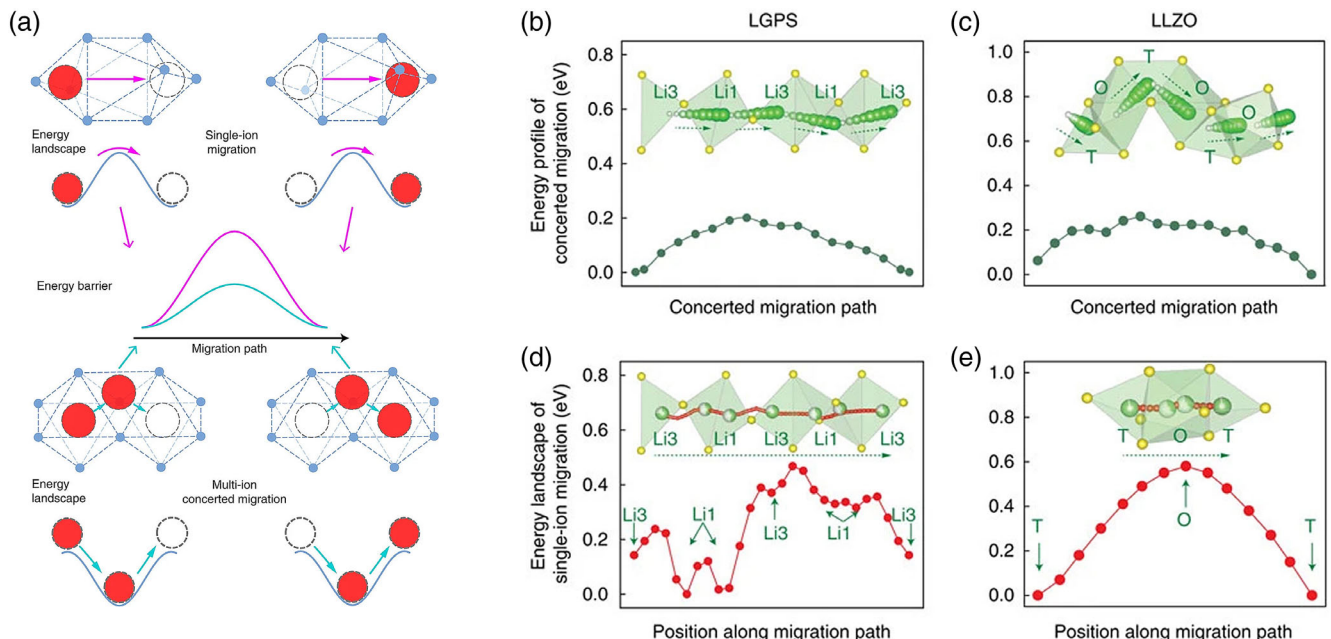


FIGURE 7 Schematic of concerted diffusion of Li ions. (a) A comparison in migration energy profiles between single-ion hops and multi-ion concerted diffusions. The migration energy profiles in (b) LGPS and (c) LLZO by multi-ion concerted diffusions. The migration energy profiles in (d) LGPS and (e) LLZO by single-ion hops. Insets show the migration pathways in LGPS and LLZO, respectively. The green and yellow balls in the insets denote Li ions and anions, respectively. Reprinted with permission from Reference 100. Copyright © 2017 Springer Nature

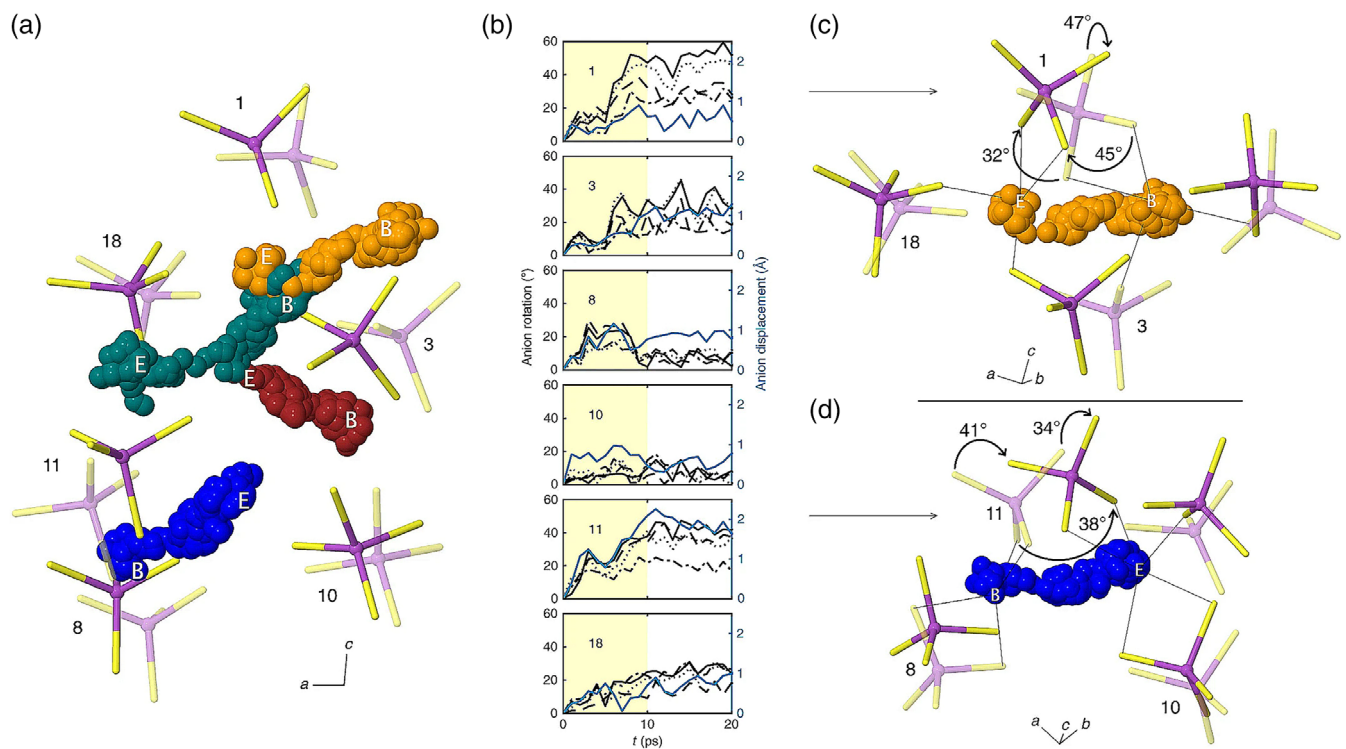


FIGURE 8 Schematic of the paddle-wheel effect. (a) The trajectories of four Li ions, where the “E” and “B” label the initial and final positions of the Li ions, respectively. The neighboring PS_4 tetrahedra are labeled by numbers. The initial positions of the PS_4 tetrahedra are shown with partial transparency to distinguish them from the final positions. (b) Angular rotations (black) and linear displacements (blue) of the PS_4 tetrahedron as a function of time. (c,d) The closeups of the Li ions and local PS_4 tetrahedra. Reprinted with permission from Reference 184. Copyright[©] 2020 Springer Nature

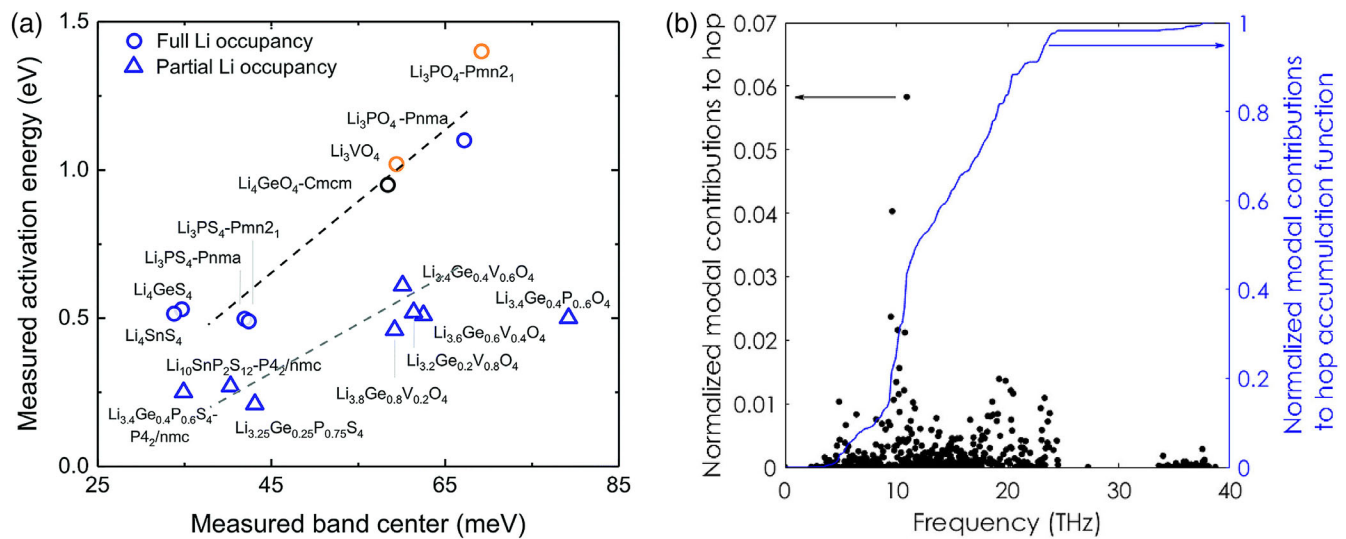


FIGURE 9 The relationship between lattice dynamics and Li transports in SEs. (a) Comparison between measured activation energy and measured phonon band center of SEs. Reprinted with permission from Reference¹⁹³. Copyright[©] 2018 Royal Society of Chemistry. (b) Vibrational modal contributions in the form of scatter (black dots) and integration (blue line) plots for one individual Li ion hop in $\text{Li}_{3.042}\text{Ge}_{0.042}\text{P}_{0.958}\text{O}_4$. Reprinted with permission from Reference 194. Copyright[©] 2021 Elsevier

origin of high ionic conductivities of LGPS. Interestingly, the equal activation energy of 0.30 eV along the $\langle 001 \rangle$ and $\langle 110 \rangle$ directions was recently measured in single-crystal LGPS samples,²⁰⁰ implying that an underlying mechanism of lithium-ion transports in LGPS needs to be further understood. In short, a Li-site connection distance of less than 2.5 Å

for a 3D percolation network is detected in common oxide and sulfide SEs, indicating the significance of the 3D Li-ion diffusion pathway (Figure 10c,d).¹⁹⁶ (3) Local disordered Li site is proposed to be a feature enabling the fast Li-ion transports in the SEs.¹⁹⁶ The distance between two neighboring 96h sites in LLZO is 0.8 Å. It seems impossible for the two sites to be occupied simultaneously. Therefore, the two sites merge into an enlarged Li site. A similar phenomenon is also observed in LGPS, in which the distance of two neighboring Li1 sites is 1.5 Å. The enlarged Li sites are also verified by the anisotropic atomic displacement parameter (ADP) in the result of ssNMR.¹⁹⁹ (4) Anion packing is also of

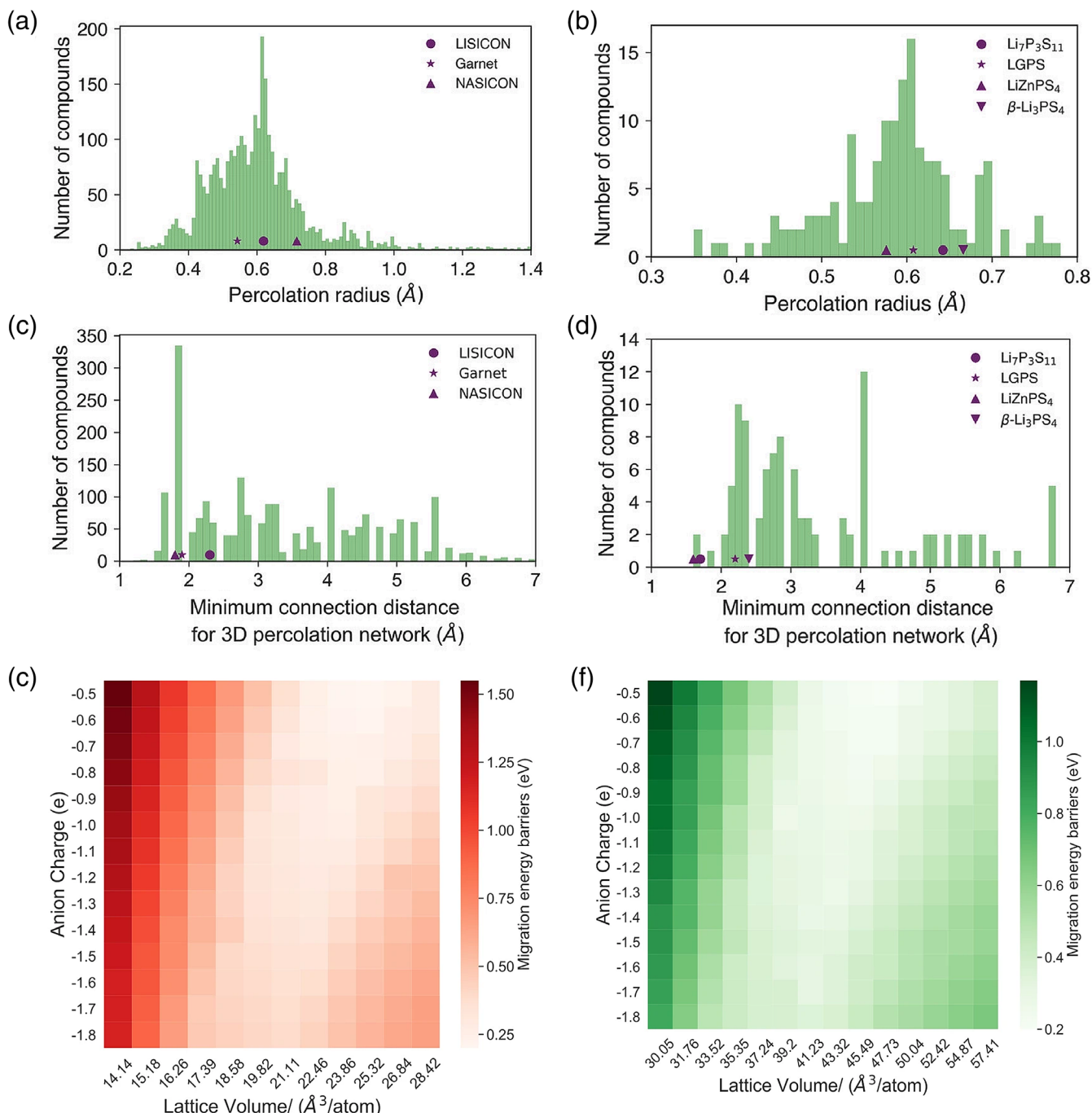


FIGURE 10 The features of the crystalline structure and electronic structure of SEs. The percolation radius (i.e., neck size) in Li-containing (a) oxides and (b) sulfides. Minimum Li-site connection distance for a 3D percolation network in Li-containing (c) oxides and (d) sulfides. Reprinted with permission from Reference 196. Copyright[©] 2019 Wiley. The migration energy barrier as a function of anion charge and lattice volume for (a) oxide and (b) sulfide SEs. Reprinted with permission from Reference 204. Copyright[©] 2020 Springer Nature

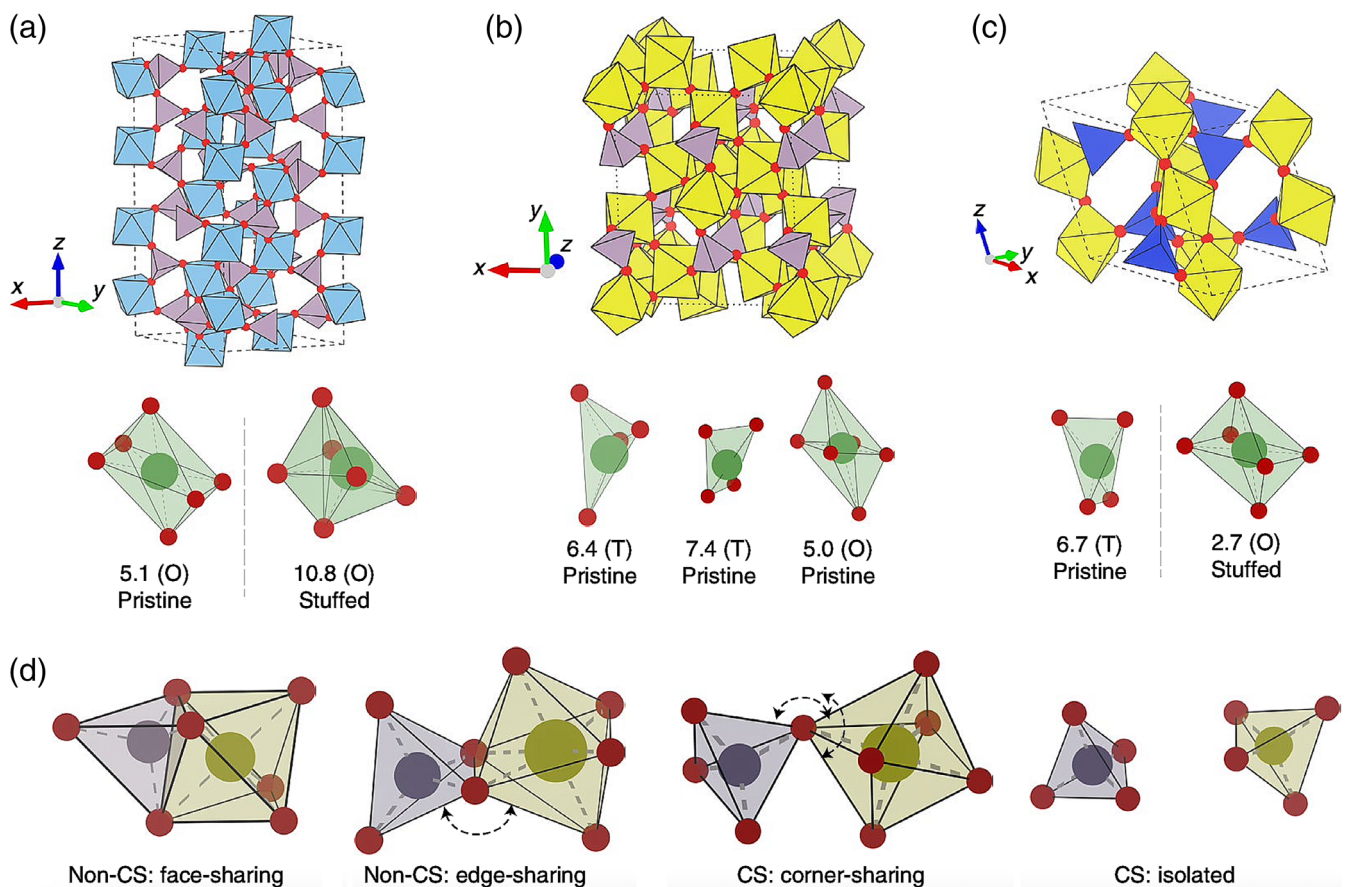


FIGURE 11 Structural analyses of common SEs with CS frameworks. Crystalline structures of common SEs (a) $\text{Li}_{1+x}\text{Al}_x\text{Ti}_{2-x}(\text{PO}_4)_3$, (b) LiTa_2PO_8 , and (c) $\text{Li}_{1+x}\text{Ta}_{1-x}\text{Zr}_{1-x}\text{SiO}_5$ with CS frameworks, in which the local Li-ion environments with labels of CSM values are shown below each framework. Both pristine and stuffed structures are considered to determine the CSM values of tetrahedra (T) and octahedra (O). (d) The illustration of the face-sharing, edge-sharing, CS, and isolated connectivity of the framework. Reprinted with permission from Reference 202. Copyright[®] 2022 Springer Nature

great concern for fast Li-ion transport. The Li-ion diffusion in body-centered cubic (BCC) anion framework exhibits lower activation energy compared to that in FCC and hexagonal close-packed (HCP) ones.²⁰¹ Such a conclusion is a critical strategy for the rational design of SEs, which will be discussed in detail in the following section. (5) Corner-sharing (CS) connectivity of the anion framework is very recently proposed as a feature for the high-ionic-conductivity oxide SEs (Figure 11).²⁰² The advantages of the CS framework are considered in three aspects. (i) The CS framework exhibits a more significantly distorted Li-ion environment than the non-CS ones with face-sharing and edge-sharing connectivity, which is characterized by continuous symmetry measure (CSM). CSM is a metric to measure the deviation from a perfect polyhedron geometry.²⁰³ (ii) Weak interactions between Li ions and other cations are detected in the CS framework. (iii) 3D diffusion pathway is more likely to appear in the structures with the CS framework.

In addition to understanding the Li-ion transport mechanism in the SEs, structural descriptors are also used to rationally design new SE materials through high-throughput calculations or ML methods. Two representative examples are discussed below. (1) High-throughput calculations using neck size, 3D Li-ion diffusion pathway, and enlarged Li sites as three descriptors.¹⁹⁶ The structures of 5537 Li-containing oxides and 510 Li-containing sulfides were exported from the Inorganic Crystal Structure Database (ICSD).²⁰⁵ 15 SE candidates were predicted to exhibit room-temperature ionic conductivity of $>0.1 \text{ mS cm}^{-1}$ after a series of structure filtering operations and AIMD simulations. (2) High-throughput calculations using the CS connectivity as a descriptor.²⁰² The structural information of 9572 compounds of quaternary Li-containing oxides was extracted from the Materials Project inorganic crystal structure database,²⁰⁶ which was further classified into 1728 groups. An automatic workflow including framework connectivity analysis, chemical suitability prediction, known phase exclusion, and high-temperature AIMD simulation was constructed. Ten new

frameworks were screened out, in which the high ionic conductivity and low activation energy of $\text{LiGa}(\text{SeO}_3)_2$ were verified by experiments. The two examples indicate the significance of structural descriptors in the design of SE materials.

3.5.5 | Electronic structure

The Li-ion transport mechanism in SEs is further understood by electronic structures. Several features are summarized below. (1) Electronegativity of non-Li cations. A higher ionic conductivity was reported in $\text{Li}_{10}\text{GeP}_2\text{S}_{12}$ than that in $\text{Li}_{10}\text{SnP}_2\text{S}_{12}$, which is interpreted by the difference in electronegativity between Sn (1.7) and Ge (2.0).²⁰⁷ The Sn atoms donate more electrons to the neighboring S atoms because of their lower electronegativity, leading to stronger Coulombic attractions between Li and S ions. A recent NMR research indicates the in-place Li1–Li4 diffusion pathway is blocked in $\text{Li}_{10}\text{SnP}_2\text{S}_{12}$, and only ca. 10% of the Li4 sites are active for Li-ion transport.²⁰⁸ Such a fresh conclusion suggests the complexity of the effect of elemental substitutions on the Li-ion transports in SEs. (2) Anionic polarizability. Sulfides SEs usually exhibit higher ionic conductivities than oxide SEs because of the larger polarizability of anion S^{2-} than that of O^{2-} .¹⁸¹ The effect of anionic polarizability on Li-ion diffusions is further understood by considering the effect of anionic size and anionic charge, both of which determine the anionic polarizability. The larger anion exhibits larger polarizability for the anions with the same charge. The anion with a more negative charge is more polarizable for the anions of the same size. The Li-ion migration energy barrier as a function of a lattice volume and an anion charge is predicted based on a hypothetical SE lattice with the FCC anion framework (Figure 10e,f). A more negative anion

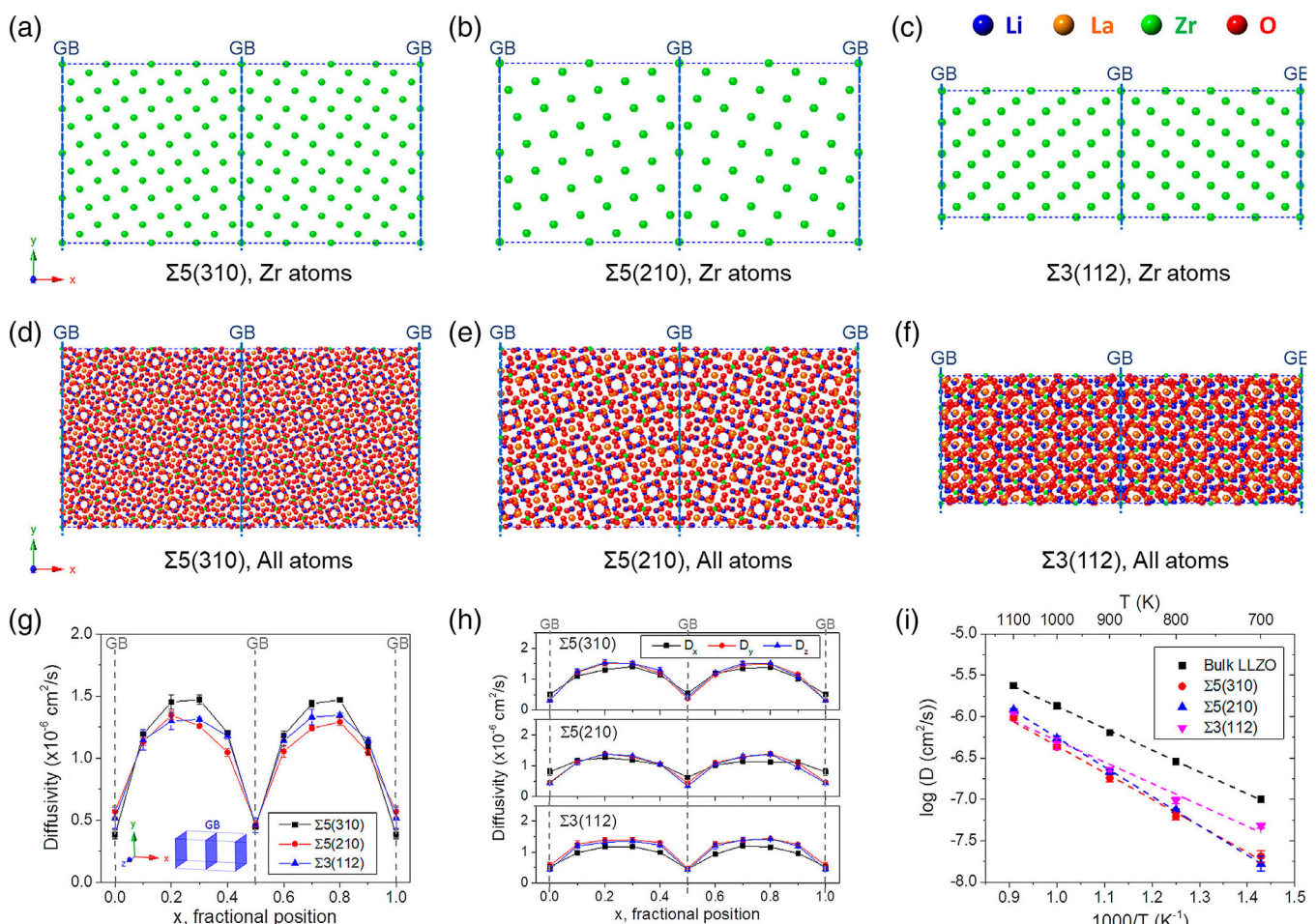


FIGURE 12 The Li transport at the GB in SEs. Model structures of the three symmetric tilt (a) $\Sigma 5(310)$, (b) $\Sigma 5(210)$, and (c) $\Sigma 3(112)$ GBs. The Zr sublattices are only shown to illustrate the coincident-site nature. The whole models are accordingly shown in panels d–f. (g) Total diffusivities and (h) decomposed diffusivities as a function of positions. (i) Arrhenius plots for Li-ion diffusivity in the GB and bulk LLZO. Reprinted with permission from Reference 219. Copyright[©] 2017 American Chemical Society

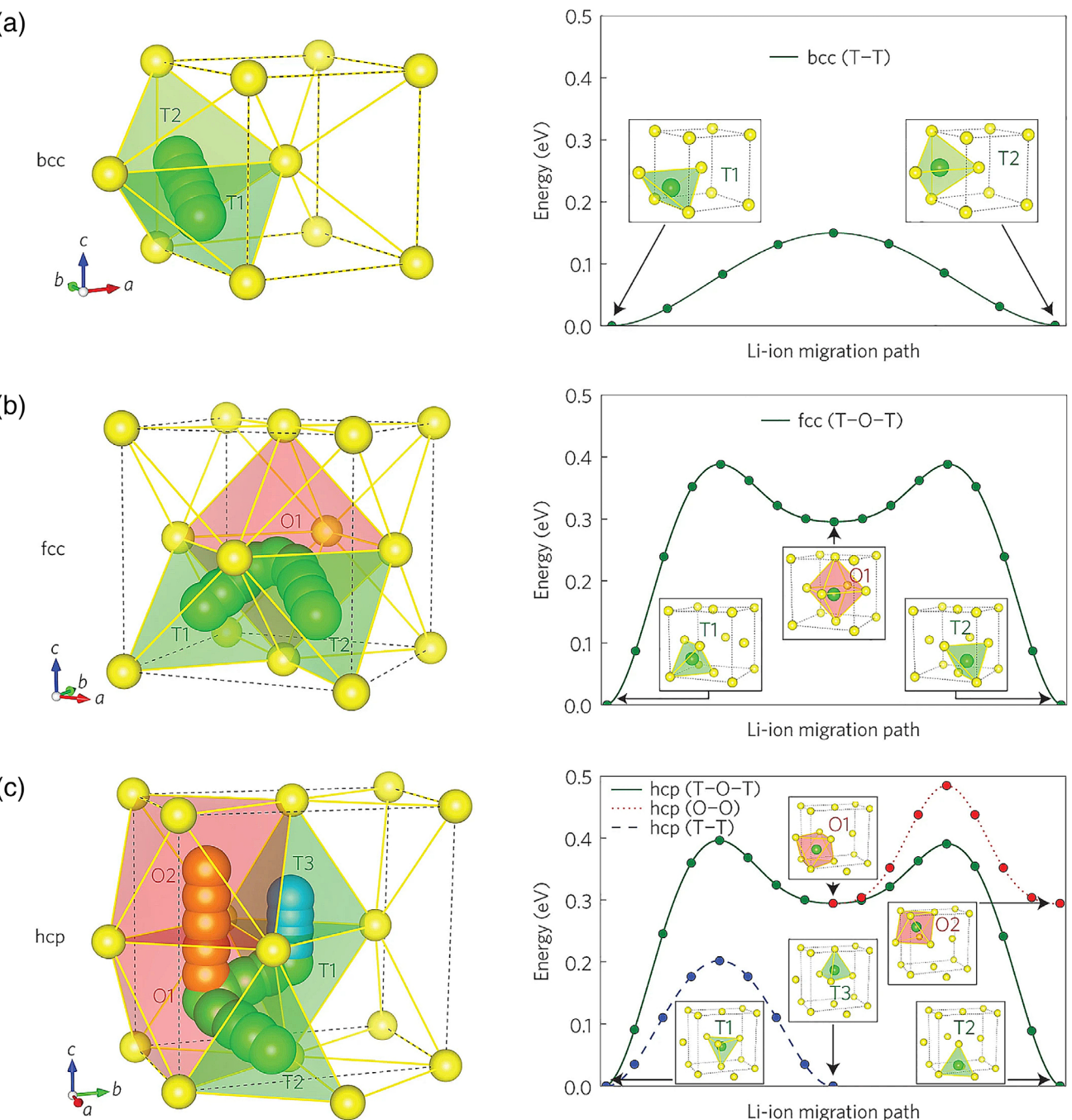


FIGURE 13 Li migration paths and corresponding calculated energy profiles in (a) BCC, (b) FCC and (c) HCP S sublattices. The yellow and green balls denote S and Li ions, respectively. The green and red regions represent LiS₄ tetrahedra and LiS₆ octahedra, respectively. Reprinted with permission from Reference 201. Copyright © 2015 Springer Nature

charge in the oxide and sulfide SEs with the same lattice volume (i.e., the same anionic size) corresponds to a lower Li-ion migration energy barrier. Based on a fact that the size of S²⁻ is larger than that of O²⁻, the sulfide SE exhibits a lower migration energy barrier than the oxide SE when the S²⁻ and O²⁻ are fixed to the same charge. Both situations demonstrate that the more polarizable anionic framework exhibits a lower Li-ion migration energy barrier.

(3) Electron density. The space with high electron density in SEs is generally unfavorable for the Li-ion transport because of a strong interaction between Li ions and electrons.²⁰⁹ Therefore, the electron density is proposed as a potentially possible descriptor to fast search for the reasonable Li-ion diffusion pathway in SEs, which has been successfully applied in the prediction of the diffusion pathways in LiFePO₄, Li₂S, Li₅PS₄Cl₂, Li₁₀GeP₂S₁₂, Li₄GeS₄, and Li₃Y(PS₄)₂.²¹⁰

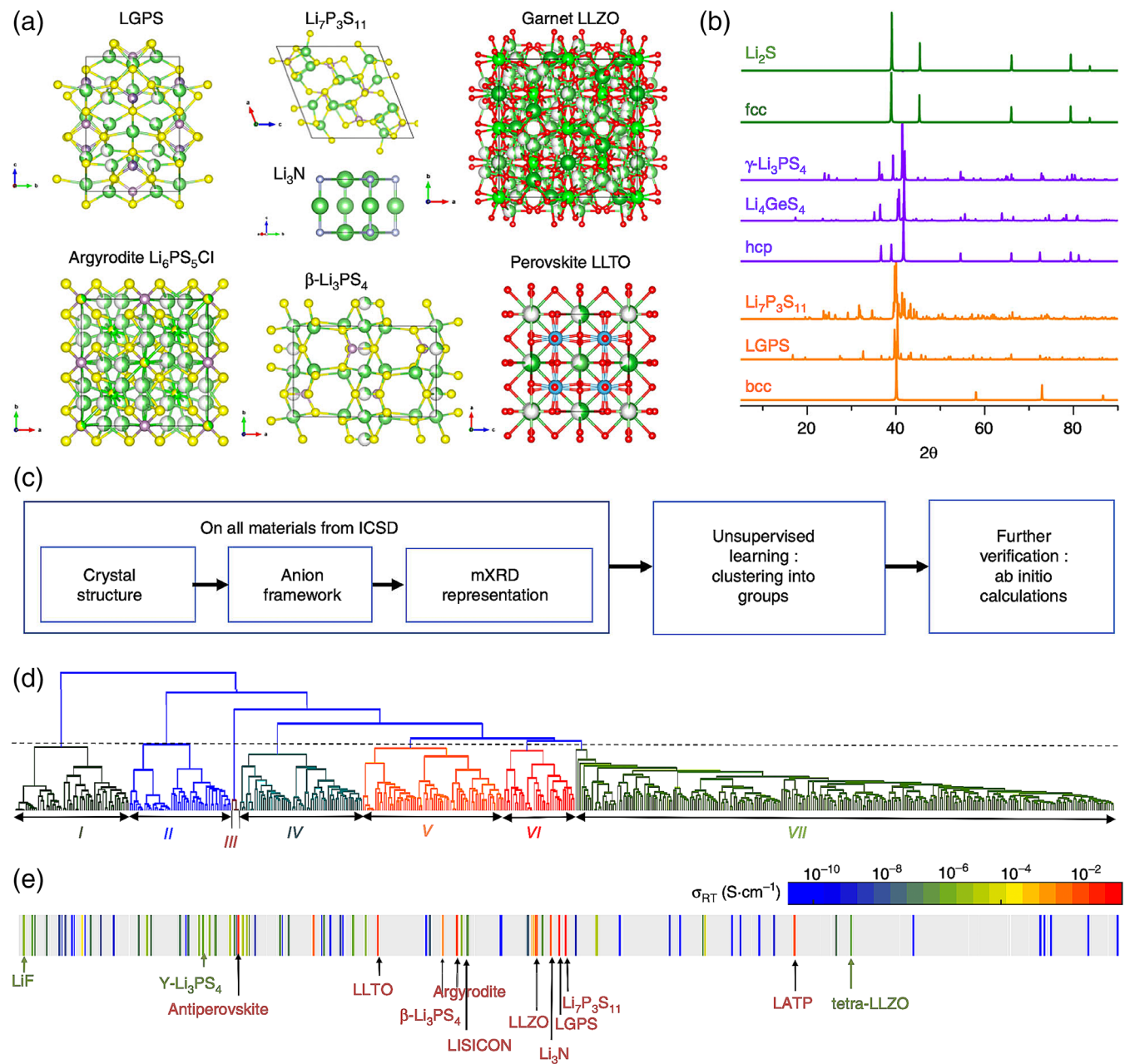


FIGURE 14 Unsupervised discovery of SEs. (a) The crystalline structures of common SEs. (b) The mXRD patterns of the common SEs and the ideal FCC, HCP, and BCC anion framework. (c) Workflow of unsupervised learning to search for potential SE candidates. (d) Bottom-up tree diagram (dendrogram) generated by the agglomerative hierarchical clustering method. (e) Mapping the dendrogram to conductivity reveals the grouping of common SEs. Reprinted with permission from Reference 282. Copyright[©] 2019 Springer Nature

3.6 | Diffusion at interfaces

Interfaces are usually considered as fast Li transport channels in solids for a long time. Compared to the average Li transport behaviors at interfaces characterized by experimental techniques, the Li transport properties predicted by atomistic simulations heavily rely on computational models. Such a situation hinders a direct comparison between experimental and computational results. Two explicit situations are discussed as follows.

3.6.1 | Interfaces in solid electrolyte interphases

Since most liquid electrolytes or SEs are not chemically or electrochemically stable with lithium metal anodes, multicomponent interphase at the electrode surface with a thickness of dozens of nanometers has been proposed by Peled in 1979, namely, solid electrolyte interphases (SEIs).^{211–214} It is generally recognized that SEIs are composed of nano-sized inorganic and organic building blocks, in which higher-proportion inorganic structures are distributed in the inner layer, close to electrodes. The structural and component complexity impedes the understanding of Li-ion transports in SEIs. The high activation energy and low ionic conductivities indicate the slow Li-ion transports in bulk inorganic SEIs, for example, the activation energy of 1.99,²¹⁵ 0.86,²¹⁶ and 0.67 eV⁹⁷ for LiF, Li₂O, and Li₂CO₃, respectively. Therefore, the Li-ion transport in inorganic SEIs is considered to be mediated by the grain boundary (GB) between the components. Ramasubramanian et al. predicted the activation energy of the Li-ion transports in $\Sigma 5$ LiF/LiF, $\Sigma 15$ Li₂O/Li₂O, and LiF/Li₂O GBs is 0.68, 0.78, and 0.45 eV,²¹⁷ much lower than those of bulk counterparts. Li-ion diffusion coefficients of 4.6×10^{-16} and $3.16 \times 10^{-23} \text{ m}^2 \text{ s}^{-1}$ were estimated in $\Sigma 5$ and $\Sigma 3$ LiF/LiF GB, respectively, compared to that of $3.5 \times 10^{-20} \text{ m}^2 \text{ s}^{-1}$ in bulk LiF.²¹⁷ Such results indicate that Li-ion transport pathway in SEIs is regulated by the structure matching. A similar NEB calculation demonstrated low activation energy (0.10–0.22 eV) of the Li transport in LiF/Li₂CO₃ GB compared to that (0.30 eV) in bulk Li₂CO₃.²¹⁸

3.6.2 | Interfaces in solid electrolytes

Different from the general understanding that the interface is fast Li transport channels in solids, the GBs in SEs exhibit slow average Li-ion transports than the bulk characterized by EIS analyses. Several low-energy symmetric tilt GBs in LLZO including $\Sigma 3(112)$, $\Sigma 5(210)$, and $\Sigma 5(310)$ were constructed and investigated by CMD simulations (Figure 12).²¹⁹ Several intriguing conclusions are summarized. (1) $\Sigma 5$ GBs (0.64 and 0.71 eV) exhibit higher activation energy of Li diffusions than the bulk (0.52 eV) and $\Sigma 3$ GB (0.52 eV). (2) The diffusion coefficient ($[3\text{--}15] \times 10^{-19} \text{ m}^2 \text{ s}^{-1}$) at room temperature in $\Sigma 5$ GBs is much lower than that in bulk ($9.16 \times 10^{-17} \text{ m}^2 \text{ s}^{-1}$) and $\Sigma 3$ GB ($4.71 \times 10^{-17} \text{ m}^2 \text{ s}^{-1}$). (3) Compared with $\Sigma 3$ GB with diffusion isotropy, $\Sigma 5$ GB exhibits a definite diffusion anisotropy. The diffusion coefficient ($4 \times 10^{-16} \text{ m}^2 \text{ s}^{-1}$) of $\Sigma 5$ GB along the GB is 1000 times that ($4 \times 10^{-19} \text{ m}^2 \text{ s}^{-1}$) through the GB. Very recently, an AIMD simulation also demonstrated the high diffusion coefficient at the $\Sigma 3$ GB in LLZO by comparing the Li transport in bulk and at $\Sigma 1(110)$ and $\Sigma 3(112)$.²²⁰

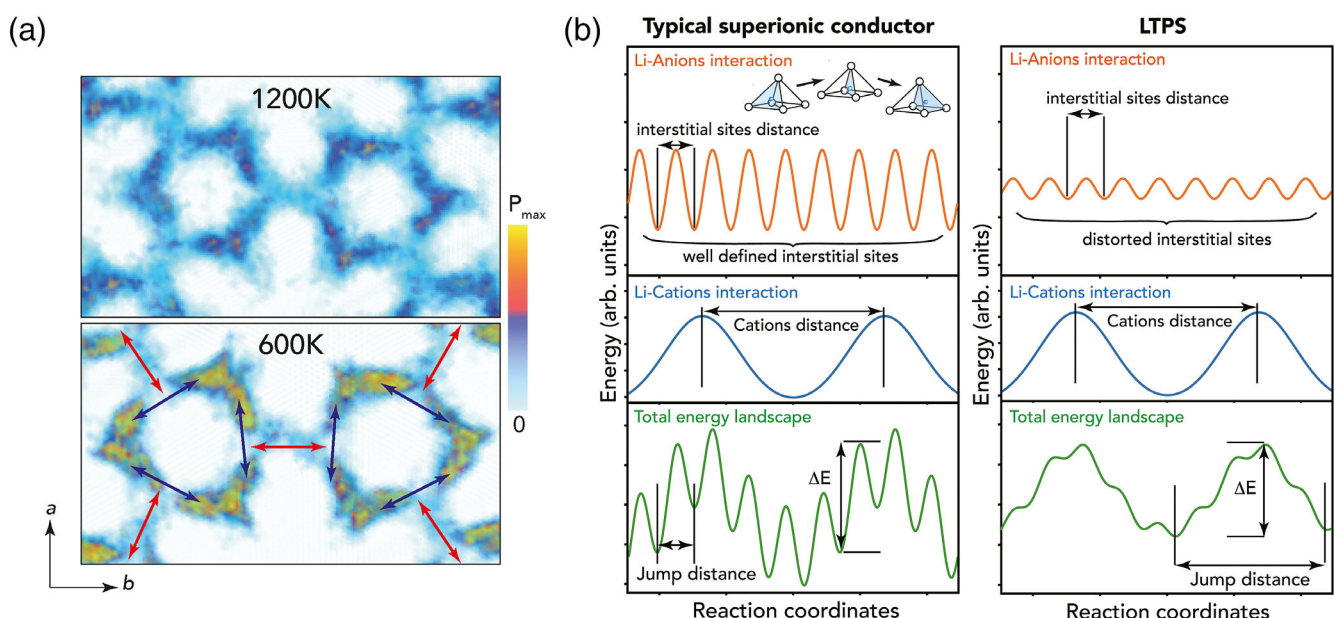


FIGURE 15 Illustration of a high pre-exponential factor in LTPS. (a) The Li probability density obtained from AIMD simulations. The migration energy landscape composed of Li-anion and Li-cation interactions for (b) a typical superionic conductor LGPS and (c) LTPS. Reprinted with permission from Reference 286. Copyright © 2019 Elsevier

4 | FAST Li TRANSPORT DESIGN

Fast Li transport is indispensable to ensure the excellent dynamical stability of SSBMs during battery operation. According to the formula determining the Li diffusion coefficient $D^* = D_0 \exp\left(-\frac{H_a}{k_B T}\right)$, several strategies are considered, that is, decreasing activation energy and increasing pre-exponential factor. In addition, interface design strategies are also deliberated to improve interfacial Li transports.

4.1 | Activation energy

Activation energy remarkably affects the sensitivity of diffusion coefficient to temperature because of its location in the exponential term. Such a situation implies that a smaller difference in diffusion coefficients between room temperature and low temperature (e.g., -20°C) appears in an ion conductor with low activation energy, which is of critical significance for the design of low-temperature electrolytes. Several insights to decrease activation energy are summarized as follows.

(1) *Anion packing*. The Li-ion diffusion in BCC anion framework exhibits lower activation energy compared to that in FCC and HCP ones.²⁰¹ The Li ions within BCC anion sublattices hop between two equivalent face-sharing tetrahedral sites, that is, T1-T2 path. The Li ions with FCC anion sublattices migrate through a tetrahedron-octahedron-tetrahedron (T1-O1-T2) pathway. The Li ions with HCP anion sublattices have three migration paths, (i) T1-O1-T2 pathway similar to that within FCC anion sublattice, (ii) T1-T3 pathway, and (iii) O1-O2 pathway (Figure 13). The activation energy (0.15 eV) of Li migration along with the T1-T2 path is much lower than that along with the T1-O1-T2 path (0.40 eV) with the same volume of anion sublattices (40 \AA^3), which is responsible for the fast Li transport within BCC anion sublattices. Such the mechanism is the origin of low activation energy in SEs LGPS (0.25 eV),¹⁷¹ Li₇P₃S₁₁ (0.18 eV),¹⁷³ Li₃BS₃ (0.21 eV),²⁸³ β -Li₃PS₄ (0.16 eV),²³⁷ Li₃OCl (0.26 eV),²⁸⁴ and Li₃OCl_{0.5}Br_{0.5} (0.18 eV).²⁸⁴

Based on the knowledge of the anion packing and ionic conductivity data of common SEs, unsupervised learning was performed to search for the potential high-ionic-conductivity SE materials.²⁸² A representation of normalized x-ray diffraction invariant to lattice parameter or chemical constituent, which is called modified x-ray diffraction (mXRD), is used for unsupervised learning (Figure 14a,b). In total, 2986 compounds that contain lithium but not transition metals were extracted from the ICSD database, in which 528 representative structures were further determined to obtain their mXRDs (Figure 14c). These structures and mXRD information were used to construct an initial dataset. Clustering was performed by the agglomerative hierarchical clustering method to train a bottom-up grouping of the mXRD dataset (Figure 14d). The common SE materials except LATP were clustered into 2 groups in total 7 groups (Figure 14e). The structural feature corresponding to the 2 groups is considered to be beneficial to the fast Li-ion diffusions. Therefore, the other structures in the 2 groups were used for the next filtering step, that is, AIMD simulations. Finally, 16 candidates are predicted to have a room-temperature ionic conductivity of more than $10^{-1} \text{ mS cm}^{-1}$.

(2) *Doping*. Replacing the anions in SEs with higher-atomic-number isovalent ones usually receives lower activation energy because of the larger polarizability of the latter. Such rule has been demonstrated in Li₃PX₄ (X = O and S),^{235,285} LiTi₂(PX₄)₃ (X = O and S),^{195,286} Li₆PX₅I (X = S and Se),²⁸⁷ and Li₃ErX₆ (X = Cl and I).²⁸⁸ However, a few exceptions have also been reported, in which other factors more significantly affect the activation energy, for example, the inductive effect in Li₁₀XP₂S₁₂ (X = Ge and Sn)²⁰⁷ and the anion disorder in Li₆PS₅X (X = Br and I).²⁸⁹ The effect of cationic doping on Li transports mainly affects the Li concentration in lattices and further the distribution of Li sublattices, which is attributed to the changed elemental composition of SEs induced by cationic doping, different from the direct interactions between anions and Li ions.

(3) *Li concentration*. A moderate Li concentration is desirable to enable low activation energy in SEs, which is necessary to activate the concerted diffusion modes. Li ions prefer occupying the low-energy sites in the solids with a low Li concentration. A large diffusion barrier (i.e., activation energy) for single-ion jumps needs to be overwhelmed. The lack of vacancy also results in the difficulty of Li-ion migrations in the solids with a too high Li concentration. Therefore, partially occupied, enlarged Li sites are usually found in SEs.¹⁹⁶ The regulation of lithium concentration often depends on cationic doping. For example, the anion substitution by Si, Ge, and Sn in Li₆PS₅I significantly decrease the activation energy from 0.37 eV in pristine Li₆PS₅I to 0.24 eV in Li_{6.24}P_{0.76}Ge_{0.24}S₅I.²⁹⁰ The similar change of the Li sublattice induced by Si, Ge, and Sn is demonstrated by the x-ray and neutron diffraction analysis. Li7-type garnet (0.3 eV in

LLZO) exhibits considerably low activation energy than Li3- (1.5 eV in $\text{Li}_7\text{La}_3\text{Te}_2\text{O}_{12}$) and Li5-type (0.8 eV in $\text{Li}_7\text{La}_3\text{Nb}_2\text{O}_{12}$) ones by substituting Te or Nb with Zr.²⁹¹

4.2 | Pre-exponential factor

In addition to the widely concerned activation energy, the pre-exponential factor D_0 is receiving increasing attention in the scientific community. Recent research indicates that increasing the anion lattice polarizability in $\text{Li}_6\text{PS}_5\text{X}$ ($\text{X} = \text{Cl}, \text{Br}, \text{and I}$) decreases both the activation energy and pre-exponential factor,²⁹² which is attributed to the positive correlation between pre-exponential factor and activation energy, that is, so-called compensation (Meyer-Neldel) rule proposed by Meyer and Neldel in 1937.²⁹³ An alternative idea to enable fast Li-ion diffusion design is increasing pre-exponential factor. A promising SE candidate $\text{LiTi}_2(\text{PS}_4)_3$ (LTPS) with a high pre-exponential factor has been reported.²⁸⁶ Despite similar activation energy of LTPS (246 meV) and LGPS (220 meV), the former ($2.94 \times 10^{-7} \text{ m}^2 \text{ s}^{-1}$) exhibits a much higher pre-exponential factor than the latter ($1.31 \times 10^{-8} \text{ m}^2 \text{ s}^{-1}$), comparable with the common liquid electrolytes 1 M LiPF_6 in EC/DEC. As a consequence, the ionic diffusivity of LTPS ($1.2 \times 10^{-11} \text{ m}^2 \text{ s}^{-1}$) is higher than that of LGPS ($2.20 \times 10^{-12} \text{ m}^2 \text{ s}^{-1}$). The high pre-exponential factor is attributed to unusual Li-ion distribution in LTPS, that is, ring-like Li “pockets” deviating from crystallographic Li-ion sites (Figure 15a). A long jump length and high migration entropy contribute to a liquid-like Li-ion diffusion in LTPS (Figure 15b).

Another strategy to increase pre-exponential factors is increasing defect concentration. The sluggish Li transports in Li metal and SEI including LiF and Li_2O are ascribed to ultralow defect concentrations instead of high migration energy. For example, a vacancy concentration of $4 \times 10^{-5} \text{ mol L}^{-3}$ in BCC Li has been determined based on a vacancy formation energy of 520 meV.¹⁴⁷ In contrast, the migration energy of the vacancies in BCC Li is only 55 meV, which is much low than that (200–300 meV) of common SEs. The introduction of extrinsic defects is critical to increasing the Li diffusion coefficient in Li metal, compared to the abundant intrinsic defects in SEs.

4.3 | Carrier concentration

Since ionic conductivities σ are directly proportional to carrier concentration c according to the Nernst–Einstein equation $\sigma = \frac{cq^2}{k_b T} D_\sigma$, increasing carrier concentration is also an effective strategy to accelerate Li transports. The carrier concentrations (e.g., 33.6 mol L^{-3} in LGPS and 42.5 mol L^{-3} in LLZO) in Li-contained solids are usually much larger than those in the liquid electrolytes (0.01 – 4 mol L^{-3}).^{10,294} The high carrier concentration is one of the origins of high ionic conductivities in SEs besides low activation energy and abundant intrinsic defect concentration as discussed above.

4.4 | Interface

Besides the fast intrinsic Li transports in crystals, interfacial design is also an indispensable strategy to enable fast Li transport in batteries. The interfacial design strategy is divided into four aspects: (1) *Anode/SE interface*: Al_2O_3 coating layer is introduced between Li metal and $\text{Li}_7\text{La}_{2.75}\text{Ca}_{0.25}\text{Zr}_{1.75}\text{Nb}_{0.25}\text{O}_{12}$ by atomic layer deposition. The interfacial impedance of the modified interface significantly decreases from 1710 to $1 \Omega \text{ cm}^2$ compared to that of the pristine Li/ $\text{Li}_7\text{La}_{2.75}\text{Ca}_{0.25}\text{Zr}_{1.75}\text{Nb}_{0.25}\text{O}_{12}$ interface.²⁹⁵ Mixed ionic–electronic conductors made of nanotubes are constructed to enable dynamically stable Li metal deposition and stripping by fast Li interfacial transport (i.e., Coble creep).²⁹⁶ (2) *SEI interface*: Since the interface in SEIs is considered as fast Li transport channel, more interface should be introduced for fast Li transport. (3) *SE/SE interface*: Theoretical calculations predict that the ionic diffusion coefficient at the GB highly depends on the GB matching type in LLZO.²¹⁹ Therefore, a possible interfacial design proposal should be considered by rationally designing GB structures in SEs. (4) *SE/cathode interface*: LiNbO_3 and $\text{Li}_4\text{Ti}_5\text{O}_{12}$ are introduced as additional coating layers on $\text{Li}(\text{Ni}_x\text{Co}_y\text{Al}_z)\text{O}_2$ and LiCoO_2 to decrease interfacial impedances, respectively.²⁹⁷ More elaborate discussion can be found in a high-quality review by Meng et al.²⁹⁸

5 | CONCLUSION AND REMARKS

The Li transport mechanisms in SSBMs are comprehensively summarized in this review. The theoretical and experimental characterization methods are briefly introduced. The design strategies to enable fast Li transports are discussed based on the terms (e.g., activation energy, pre-exponential factor, and carrier concentration) in the formula determining diffusion coefficients and ionic conductivities. The achievements and challenges of Li transport mechanisms in solid-state battery materials are discussed in detail as follows.

(1) *Understanding Li transport mechanisms in electrode materials.* The Li transport mechanisms in solids have been tried to be unscrambled over decades. Specifically, the Li transport mechanisms in SEs are sophisticatedly illustrated based on the fixed structural composition in SEs under operation. Contrarily, understanding the Li transport mechanisms in electrode materials is still challenging. First, the structures of the electrode materials with variational Li contents fall in a large configuration space, resulting in a great obstacle to determining the ground-state structures. Second, the electrode materials under operation are not in thermodynamic equilibrium. Li content gradients are inevitably distributed from the SE/electrode interface to the electrode center, which drives additional chemical diffusions in electrodes. Third, the Li transports in electrodes are difficult to be determined by a unified experimental characterization method due to the various electrode forms from metallic alloy/graphite to semiconducting Si and insulating S/LiCoO₂. Different electronic distribution characteristics in electrodes might affect Li transport behaviors.

(2) *Understanding collective motions.* The collective motions are widely considered as the origin of fast Li transports in SEs by decreasing activation energy. However, it is far away from a fundamental understanding of collective motion mechanisms in SEs. It is fascinating to understand the relationships between the concerted diffusion and the Li contents, between the concerted diffusion and the structural topology, and between the paddle-wheel effect and the anion framework type. It is still unknown whether the pre-exponential factors are affected by the collective motions. A clear understanding of collective motions is a prerequisite to rationally designing SEs with high ionic conductivities.

(3) *Interfacial design strategy.* Interfacial design is of fundamental necessity to enable fast Li transport at interfaces and address interfacial Li dynamical instability in solid-state Li metal batteries. Usually, a trial-and-error procedure is experimentally performed to search for ideal coating material (e.g., Li₃BO₃²⁹⁹ and LiNbO₃³⁰⁰) or additive (e.g., LiBr and LiI^{301–303}) candidates. It is confusing to understand the effect of the coating materials or additives on interfacial Li transports on the atomic scale because of the difficulty in directly probing the buried interfaces through experiments and the complexity of computational modeling. A reasonable and reliable simulation procedure regarding interfacial Li transports urgently needs to be established.

(4) *Artificial intelligence technology.* A new data-driven research paradigm has been established with the introduction of ML technology in scientific research. MLMD has broken through the boundaries of traditional CMD and AIMD simulations, and has shown powerful ability to reveal the Li transport mechanism in SEs.^{69,70} Unsupervised learning has significantly accelerated to screen out the promising SE candidates with high ionic conductivities and low activation energy.²⁸² As regards Li transports, It is believed that ML will play an increasingly important role in the following two aspects: (a) revealing Li transport mechanisms and designing new SE materials by MLMD and (b) high-throughput data mining of diffusion-related physical quantities by ML technology.

Fast Li transports in SSBMs are a prerequisite to ensuring superior Li dynamical stability and rate performance of batteries. Advanced theoretical prediction and experimental characterization techniques are powerful tools to understand Li transports in SSBMs, which lays the foundation for rationally designing the materials with targeted properties. The introduction of artificial intelligence technology and great advances in computer technology will significantly accelerate the research and development of materials.

AUTHOR CONTRIBUTIONS

Zhong-Heng Fu: Conceptualization (equal); data curation (equal); formal analysis (equal); investigation (equal); methodology (equal); validation (equal); writing – original draft (equal); writing – review and editing (equal). **Xiang Chen:** Conceptualization (equal); data curation (equal); formal analysis (equal); funding acquisition (equal); investigation (equal); methodology (equal); project administration (equal); resources (equal); software (equal); validation (equal); visualization (equal); writing – original draft (equal); writing – review and editing (equal). **Qiang Zhang:** Conceptualization (equal); funding acquisition (equal); investigation (equal); resources (equal); supervision (equal).

ACKNOWLEDGMENTS

The authors acknowledged the support from Tsinghua National Laboratory for Information Science and Technology for theoretical simulations. X. Chen appreciates the support from the Shuimu Tsinghua Scholar Program of Tsinghua University and the Young Elite Scientists Sponsorship Program by CAST.

FUNDING INFORMATION

This work was supported by the National Key Research and Development Program (2021YFB2500300), Beijing Municipal Natural Science Foundation (Z200011), National Natural Science Foundation of China (22109086, U1801257, and 21825501), China Postdoctoral Science Foundation (2021TQ0161 and 2021M691709), and Grant 2020GQG1006 from the Guoqiang Institute at Tsinghua University.

CONFLICT OF INTEREST

The authors have declared no conflicts of interest for this article.

DATA AVAILABILITY STATEMENT

Data available on request from the authors.

ORCID

Zhong-Heng Fu  <https://orcid.org/0000-0001-8779-9086>

Xiang Chen  <https://orcid.org/0000-0002-7686-6308>

Qiang Zhang  <https://orcid.org/0000-0002-3929-1541>

RELATED WIREs ARTICLES

[Multiscale computations and artificial intelligent models of electrochemical performance in Li-ion battery materials](#)

REFERENCES

- Cherp A, Vinichenko V, Tosun J, Gordon JA, Jewell J. National growth dynamics of wind and solar power compared to the growth required for global climate targets. *Nat Energy*. 2021;6(7):742–54.
- Hulme M, Obermeister N, Randalls S, Borie M. Framing the challenge of climate change in nature and science editorials. *Nat Clim Change*. 2018;8(6):515–21.
- Liu C, Li F, Ma L-P, Cheng H-M. Advanced materials for energy storage. *Adv Mater*. 2010;22(8):E28–62.
- Hall PJ, Bain EJ. Energy-storage technologies and electricity generation. *Energy Policy*. 2008;36(12):4352–5.
- Cheng X-B, Liu H, Yuan H, Peng H-J, Tang C, Huang J-Q, et al. A perspective on sustainable energy materials for lithium batteries. *Sustain Mater*. 2021;1(1):38–50.
- Tarascon JM, Armand M. Issues and challenges facing rechargeable lithium batteries. *Nature*. 2001;414(6861):359–67.
- Tarascon J-M. Key challenges in future Li-battery research. *Philos Trans Royal Soc A*. 1923;2010(368):3227–41.
- Dunn B, Kamath H, Tarascon J-M. Electrical energy storage for the grid: a battery of choices. *Science*. 2011;334(6058):928–35.
- Palacín MR. Recent advances in rechargeable battery materials: a chemist's perspective. *Chem Soc Rev*. 2009;38(9):2565–75.
- Shen X, Zhang X-Q, Ding F, Huang J-Q, Xu R, Chen X, et al. Advanced electrode materials in lithium batteries: retrospect and prospect. *Energy Mater Adv*. 2021;2021:1205324.
- Zhang X-Q, Cheng X-B, Chen X, Yan C, Zhang Q. Fluoroethylene carbonate additives to render uniform Li deposits in lithium metal batteries. *Adv Funct Mater*. 2017;27(10):1605989.
- Chen X, Li H-R, Shen X, Zhang Q. The origin of the reduced reductive stability of ion–solvent complexes on alkali and alkaline earth metal anodes. *Angew Chem Int Ed*. 2018;57(51):16643–7.
- Yuan H, Liu J, Lu Y, Zhao C, Cheng X, Nan H, et al. Toward practical all-solid-state batteries with sulfide electrolyte: a review. *Chem Res Chin Univ*. 2020;36(3):377–85.
- Cheng X-B, Zhao C-Z, Yao Y-X, Liu H, Zhang Q. Recent advances in energy chemistry between solid-state electrolyte and safe lithium-metal anodes. *Chem*. 2019;5(1):74–96.
- Li L, Deng Y, Chen G. Status and prospect of garnet/polymer solid composite electrolytes for all-solid-state lithium batteries. *J Energy Chem*. 2020;50:154–77.
- Zhang W-J. A review of the electrochemical performance of alloy anodes for lithium-ion batteries. *J Power Sources*. 2011;196(1):13–24.
- Oliví P, Pereira EC, Longo E, Varella JA, Bulhões LOS. Preparation and characterization of a dip-coated SnO₂ film for transparent electrodes for transmissive electrochromic devices. *J Electrochem Soc*. 1993;140(5):L81–L2.
- Pan K, Zou F, Canova M, Zhu Y, Kim J-H. Systematic electrochemical characterizations of Si and SiO anodes for high-capacity Li-ion batteries. *J Power Sources*. 2019;413:20–8.

19. Wang Z, Luan D, Madhavi S, Ming Li C, Wen LX. α -Fe₂O₃ nanotubes with superior lithium storage capability. *Chem Commun.* 2011; 47(28):8061–3.
20. Zhou G, Wang D-W, Li F, Zhang L, Li N, Wu Z-S, et al. Graphene-wrapped Fe₃O₄ anode material with improved reversible capacity and cyclic stability for lithium ion batteries. *Chem Mater.* 2010;22(18):5306–13.
21. Aurbach D, Markovsky B, Weissman I, Levi E, Ein-Eli Y. On the correlation between surface chemistry and performance of graphite negative electrodes for Li ion batteries. *Electrochim Acta.* 1999;45(1):67–86.
22. Park K-S, Benayad A, Kang D-J, Doo S-G. Nitridation-driven conductive Li₄Ti₅O₁₂ for lithium ion batteries. *J Am Chem Soc.* 2008; 130(45):14930–1.
23. Cai W, Yan C, Yao Y-X, Xu L, Xu R, Jiang L-L, et al. Rapid lithium diffusion in order@disorder pathways for fast-charging graphite anodes. *Small Struct.* 2020;1(1):2000010.
24. Andre D, Kim S-J, Lamp P, Lux SF, Maglia F, Paschos O, et al. Future generations of cathode materials: an automotive industry perspective. *J Mater Chem A.* 2015;3(13):6709–32.
25. Sun S, Zhao C-Z, Yuan H, Lu Y, Hu J-K, Huang J-Q, et al. Multiscale understanding of high-energy cathodes in solid-state batteries: from atomic scale to macroscopic scale. *Mater Futures.* 2022;1(1):012101.
26. Chen L, Qiu X, Bai Z, Fan L-Z. Enhancing interfacial stability in solid-state lithium batteries with polymer/garnet solid electrolyte and composite cathode framework. *J Energy Chem.* 2021;52:210–7.
27. Weiss M, Ruess R, Kasnatscheew J, Levartovsky Y, Levy NR, Minnmann P, et al. Fast charging of lithium-ion batteries: a review of materials aspects. *Adv Energy Mater.* 2021;11(33):2101126.
28. Gao Y, Nolan AM, Du P, Wu Y, Yang C, Chen Q, et al. Classical and emerging characterization techniques for investigation of ion transport mechanisms in crystalline fast ionic conductors. *Chem Rev.* 2020;120(13):5954–6008.
29. Zhu F, Islam MS, Zhou L, Gu Z, Liu T, Wang X, et al. Single-atom-layer traps in a solid electrolyte for lithium batteries. *Nat Commun.* 2020;11(1):1828.
30. Dawson JA, Attari TS, Chen H, Emge SP, Johnston KE, Islam MS. Elucidating lithium-ion and proton dynamics in anti-perovskite solid electrolytes. *Energ Environ Sci.* 2018;11(10):2993–3002.
31. Zhao W, Yi J, He P, Zhou H. Solid-state electrolytes for lithium-ion batteries: fundamentals, challenges and perspectives. *Electrochem Energy Rev.* 2019;2(4):574–605.
32. Gao J, Zhao Y-S, Shi S-Q, Li H. Lithium-ion transport in inorganic solid state electrolyte. *Chin Phys B.* 2016;25(1):018211.
33. Ohno S, Banik A, Dewald GF, Kraft MA, Krauskopf T, Minafra N, et al. Materials design of ionic conductors for solid state batteries. *Prog Energy.* 2020;2(2):022001.
34. Kohn W, Sham LJ. Self-consistent equations including exchange and correlation effects. *Phys Rev.* 1965;140(4A):A1133–8.
35. Perdew JP, Zunger A. Self-interaction correction to density-functional approximations for many-electron systems. *Phys Rev B.* 1981; 23(10):5048–79.
36. Perdew JP, Wang Y. Accurate and simple analytic representation of the electron-gas correlation energy. *Phys Rev B.* 1992;45(23): 13244–9.
37. Perdew JP, Burke K, Ernzerhof M. Generalized gradient approximation made simple. *Phys Rev Lett.* 1996;77(18):3865–8.
38. Becke AD. Density-functional exchange-energy approximation with correct asymptotic behavior. *Phys Rev A.* 1988;38(6):3098–100.
39. Lee C, Yang W, Parr RG. Development of the Colle-Salvetti correlation-energy formula into a functional of the electron density. *Phys Rev B.* 1988;37(2):785–9.
40. Perdew JP, Kurth S, Zupan A, Blaha P. Accurate density functional with correct formal properties: a step beyond the generalized gradient approximation. *Phys Rev Lett.* 1999;82(12):2544–7.
41. Heyd J, Scuseria GE, Ernzerhof M. Hybrid functionals based on a screened coulomb potential. *J Chem Phys.* 2003;118(18):8207–15.
42. Dudarev SL, Botton GA, Savrasov SY, Humphreys CJ, Sutton AP. Electron-energy-loss spectra and the structural stability of nickel oxide: an LSDA+U study. *Phys Rev B.* 1998;57(3):1505–9.
43. Welborn M, Cheng L, Miller TF. Transferability in machine learning for electronic structure via the molecular orbital basis. *J Chem Theory Comput.* 2018;14(9):4772–9.
44. Cheng L, Welborn M, Christensen AS, Miller III TF. A universal density matrix functional from molecular orbital-based machine learning: transferability across organic molecules. *J Chem Phys.* 2019;150(13):131103.
45. Cheng L, Kovachki NB, Welborn M, Miller TF. Regression clustering for improved accuracy and training costs with molecular-orbital-based machine learning. *J Chem Theory Comput.* 2019;15(12):6668–77.
46. Chen Y, Zhang L, Wang H, E W. Ground state energy functional with Hartree–Fock efficiency and chemical accuracy. *J Phys Chem A.* 2020;124(35):7155–65.
47. Xiao Y, Wang Y, Bo S-H, Kim JC, Miara LJ, Ceder G. Understanding interface stability in solid-state batteries. *Nat Rev Mater.* 2020; 5(2):105–26.
48. Urban A, Seo D-H, Ceder G. Computational understanding of Li-ion batteries. *NPJ Comput Mater.* 2016;2(1):16002.
49. Wang A, Kadam S, Li H, Shi S, Qi Y. Review on modeling of the anode solid electrolyte interphase (SEI) for lithium-ion batteries. *NPJ Comput Mater.* 2018;4(1):15.
50. He Q, Yu B, Li Z, Zhao Y. Density functional theory for battery materials. *Energy Environ Mater.* 2019;2(4):264–79.
51. Henkelman G, Uberuaga BP, Jónsson H. A climbing image nudged elastic band method for finding saddle points and minimum energy paths. *J Chem Phys.* 2000;113(22):9901–4.

52. Bernges THR, Wankmiller B, Imasato K, Lin S, Ghidu M, et al. Diffusion-mediated thermal and ionic transport in superionic conductors. *ChemRxiv*. 2021. <https://doi.org/10.26434/chemrxiv-2021-3zxh4>
53. Sheppard D, Terrell R, Henkelman G. Optimization methods for finding minimum energy paths. *J Chem Phys*. 2008;128(13):134106.
54. Siegel DJ, Nazar L, Chiang Y-M, Fang C, Balsara NP. Establishing a unified framework for ion solvation and transport in liquid and solid electrolytes. *Trends Chem*. 2021;3(10):807–18.
55. Roy K, Kar S, Das RN. Chapter 5—Computational chemistry. In: Roy K, Kar S, Das RN, editors. *Understanding the basics of QSAR for applications in pharmaceutical sciences and risk assessment*. Boston, MA: Academic Press; 2015. p. 151–89.
56. Alder BJ, Wainwright TE. Phase transition for a hard sphere system. *J Chem Phys*. 1957;27(5):1208–9.
57. Rahman A. Correlations in the motion of atoms in liquid argon. *Phys Rev*. 1964;136(2A):A405–11.
58. Tersoff J. Modeling solid-state chemistry: interatomic potentials for multicomponent systems. *Phys Rev B*. 1989;39(8):5566–8.
59. Daw MS, Foiles SM, Baskes MI. The embedded-atom method: a review of theory and applications. *Mater Sci Rep*. 1993;9(7):251–310.
60. Blank TB, Brown SD, Calhoun AW, Doren DJ. Neural network models of potential energy surfaces. *J Chem Phys*. 1995;103(10):4129–37.
61. Behler J, Parrinello M. Generalized neural-network representation of high-dimensional potential-energy surfaces. *Phys Rev Lett*. 2007;98(14):146401.
62. Artrith N, Morawietz T, Behler J. High-dimensional neural-network potentials for multicomponent systems: applications to zinc oxide. *Phys Rev B*. 2011;83(15):153101.
63. Zubatyuk R, Smith JS, Leszczynski J, Isayev O. Accurate and transferable multitask prediction of chemical properties with an atoms-in-molecules neural network. *Sci Adv*. 2019;5(8):eaav6490.
64. Artrith N, Urban A. An implementation of artificial neural-network potentials for atomistic materials simulations: performance for TiO_2 . *Comput Mater Sci*. 2016;114:135–50.
65. Khorshidi A, Peterson AA. *Amp*: a modular approach to machine learning in atomistic simulations. *Comput Phys Commun*. 2016;207:310–24.
66. Zhang L, Han J, Wang H, Car R, E W. Deep potential molecular dynamics: a scalable model with the accuracy of quantum mechanics. *Phys Rev Lett*. 2018;120(14):143001.
67. Bartók AP, Payne MC, Kondor R, Csányi G. Gaussian approximation potentials: the accuracy of quantum mechanics, without the electrons. *Phys Rev Lett*. 2010;104(13):136403.
68. Wang H, Zhang L, Han J, Weinan E. DeePMD-kit: a deep learning package for many-body potential energy representation and molecular dynamics. *Comput Phys Commun*. 2018;228:178–84.
69. Fu Z-H, Chen X, Yao N, Shen X, Ma X-X, Feng S, et al. The chemical origin of temperature-dependent lithium-ion concerted diffusion in sulfide solid electrolyte $\text{Li}_{10}\text{GeP}_2\text{S}_{12}$. *J Energy Chem*. 2022;70:59–66.
70. Huang J, Zhang L, Wang H, Zhao J, Cheng J, E W. Deep potential generation scheme and simulation protocol for the $\text{Li}_{10}\text{GeP}_2\text{S}_{12}$ -type superionic conductors. *J Chem Phys*. 2021;154(9):094703.
71. Qi J, Banerjee S, Zuo Y, Chen C, Zhu Z, Holekevi Chandrappa ML, et al. Bridging the gap between simulated and experimental ionic conductivities in lithium superionic conductors. *Mater Today Phys*. 2021;21:100463.
72. Behler J. Perspective: machine learning potentials for atomistic simulations. *J Chem Phys*. 2016;145(17):170901.
73. Behler J. Four generations of high-dimensional neural network potentials. *Chem Rev*. 2021;121(16):10037–72.
74. Deringer VL, Bartók AP, Bernstein N, Wilkins DM, Ceriotti M, Csányi G. Gaussian process regression for materials and molecules. *Chem Rev*. 2021;121(16):10073–141.
75. Chitra R, Yashonath S. Estimation of error in the diffusion coefficient from molecular dynamics simulations. *J Phys Chem B*. 1997;101(27):5437–45.
76. Huang R, Chavez I, Taute KM, Lukic B, Jeney S, Raizen MG, et al. Direct observation of the full transition from ballistic to diffusive Brownian motion in a liquid. *Nat Phys*. 2011;7(7):576–80.
77. Einstein A. Über die von der molekularkinetischen theorie der wärme geforderte bewegung von in ruhenden flüssigkeiten suspendierten teilchen. *Ann Phys*. 1905;322(8):549–60.
78. von Smoluchowski M. Zur kinetischen theorie der Brownschen molekularbewegung und der suspensionen. *Ann Phys*. 1906;326(14):756–80.
79. Marconi UMB, Puglisi A, Rondoni L, Vulpiani A. Fluctuation–dissipation: response theory in statistical physics. *Phys Rep*. 2008;461(4):111–95.
80. Irvine JTS, Sinclair DC, West AR. Electroceramics: characterization by impedance spectroscopy. *Adv Mater*. 1990;2(3):132–8.
81. Wen CJ, Boukamp BA, Huggins RA, Weppner W. Thermodynamic and mass transport properties of “LiAl”. *J Electrochem Soc*. 1979;126(12):2258–66.
82. Weppner W, Huggins RA. Determination of the kinetic parameters of mixed-conducting electrodes and application to the system Li_3Sb . *J Electrochem Soc*. 1977;124(10):1569–78.
83. Xie J, Imanishi N, Zhang T, Hirano A, Takeda Y, Yamamoto O. Li-ion diffusion kinetics in LiFePO_4 thin film prepared by radio frequency magnetron sputtering. *Electrochim Acta*. 2009;54(20):4631–7.
84. Brugge RH, Chater RJ, Kilner JA, Aguadero A. Experimental determination of Li diffusivity in LLZO using isotopic exchange and FIB-SIMS. *J Phys Energy*. 2021;3(3):034001.
85. Reif B, Ashbrook SE, Emsley L, Hong M. Solid-state NMR spectroscopy. *Nat Rev Dis Primers*. 2021;1(1):2.

86. Goc R. Calculation of the NMR second moment for materials with different types of internal rotation. *Solid State Nucl Magn Reson*. 1998;13(1):55–61.
87. Karlsson M. Proton dynamics in oxides: insight into the mechanics of proton conduction from quasielastic neutron scattering. *Phys Chem Chem Phys*. 2015;17(1):26–38.
88. Chudley CT, Elliott RJ. Neutron scattering from a liquid on a jump diffusion model. *Proc Phys Soc*. 1961;77(2):353–61.
89. Sugiyama J, Mukai K, Ikeda Y, Nozaki H, Måansson M, Watanabe I. Li diffusion in Li_xCoO_2 probed by muon-spin spectroscopy. *Phys Rev Lett*. 2009;103(14):147601.
90. Sugiyama J. Ion diffusion in solids probed by muon-spin spectroscopy. *J Physical Soc Japan*. 2013;82:SA023.
91. Roberts-Austen WC. X. Bakerian lecture.—on the diffusion of metals. *Philos Trans R Soc London, Ser A*. 1896;187:383–415.
92. Van der Ven A, Ceder G. Lithium diffusion in layered Li_xCoO_2 . *Electrochem Solid St*. 2000;3(7):301–4.
93. Van der Ven A, Thomas JC, Xu Q, Swoboda B, Morgan D. Nondilute diffusion from first principles: Li diffusion in Li_xTiS_2 . *Phys Rev B*. 2008;78(10):104306.
94. Kob W, Donati C, Plimpton SJ, Poole PH, Glotzer SC. Dynamical heterogeneities in a supercooled Lennard-Jones liquid. *Phys Rev Lett*. 1997;79(15):2827–30.
95. Donati C, Douglas JF, Kob W, Plimpton SJ, Poole PH, Glotzer SC. Stringlike cooperative motion in a supercooled liquid. *Phys Rev Lett*. 1998;80(11):2338–41.
96. Zener C. Ring diffusion in metals. *Acta Crystallogr*. 1950;3(5):346–54.
97. Shi S, Lu P, Liu Z, Qi Y, Hector LG, Li H, et al. Direct calculation of Li-ion transport in the solid electrolyte interphase. *J Am Chem Soc*. 2012;134(37):15476–87.
98. Chen B, Xu C, Zhou J. Insights into grain boundary in lithium-rich anti-perovskite as solid electrolytes. *J Electrochem Soc*. 2018;165(16):A3946–51.
99. He X, Sun H, Ding X, Zhao K. Grain boundaries and their impact on Li kinetics in layered-oxide cathodes for Li-ion batteries. *J Phys Chem C*. 2021;125(19):10284–94.
100. He X, Zhu Y, Mo Y. Origin of fast ion diffusion in super-ionic conductors. *Nat Commun*. 2017;8(1):15893.
101. Zhang Z, Nazar LF. Exploiting the paddle-wheel mechanism for the design of fast ion conductors. *Nat Rev Mater*. 2022;7:389–405. <https://doi.org/10.1038/s41578-021-00401-0>
102. Morgan D, Van der Ven A, Ceder G. Li conductivity in Li_xMPO_4 ($M = \text{Mn, Fe, Co, Ni}$) olivine materials. *Electrochem Solid St*. 2004;7(2):A30–2.
103. Zheng X, Gu Z, Fu J, Wang H, Ye X, Huang L, et al. Knocking down the kinetic barriers towards fast-charging and low-temperature sodium metal batteries. *Energ Environ Sci*. 2021;14(9):4936–47.
104. Gavilán-Arriazu EM, Mercer MP, Barraco DE, Hoster HE, Leiva EPM. Kinetic Monte Carlo simulations applied to Li-ion and post Li-ion batteries: a key link in the multi-scale chain. *Prog Energy*. 2021;3(4):042001.
105. Yazami R, Touzain P. A reversible graphite-lithium negative electrode for electrochemical generators. *J Power Sources*. 1983;9(3):365–71.
106. Kganyago KR, Ngepe PE. Structural and electronic properties of lithium intercalated graphite LiC_6 . *Phys Rev B*. 2003;68(20):205111.
107. Cai W, Yao Y-X, Zhu G-L, Yan C, Jiang L-L, He C, et al. A review on energy chemistry of fast-charging anodes. *Chem Soc Rev*. 2020;49(12):3806–33.
108. Gao T, Han Y, Fragedakis D, Das S, Zhou T, Yeh C-N, et al. Interplay of lithium intercalation and plating on a single graphite particle. *Joule*. 2021;5(2):393–414.
109. Persson K, Hinuma Y, Meng YS, Van der Ven A, Ceder G. Thermodynamic and kinetic properties of the Li-graphite system from first-principles calculations. *Phys Rev B*. 2010;82(12):125416.
110. Ran Y, Zou Z, Liu B, Wang D, Pu B, Mi P, et al. Towards prediction of ordered phases in rechargeable battery chemistry via group–subgroup transformation. *NPJ Comput Mater*. 2021;7(1):184.
111. Yu P, Popov BN, Ritter JA, White RE. Determination of the lithium ion diffusion coefficient in graphite. *J Electrochem Soc*. 1999;146(1):8–14.
112. Takami N, Satoh A, Hara M, Ohsaki T. Structural and kinetic characterization of lithium intercalation into carbon anodes for secondary lithium batteries. *J Electrochem Soc*. 1995;142(2):371–9.
113. Yang H, Bang HJ, Prakash J. Evaluation of electrochemical interface area and lithium diffusion coefficient for a composite graphite anode. *J Electrochem Soc*. 2004;151(8):A1247.
114. Dathar GKP, Sheppard D, Stevenson KJ, Henkelman G. Calculations of Li-ion diffusion in olivine phosphates. *Chem Mater*. 2011;23(17):4032–7.
115. Johnston WD, Heikes RR, Sestrich D. The preparation, crystallography, and magnetic properties of the $\text{Li}_x\text{Co}_{1-x}\text{O}$ system. *J Phys Chem Solid*. 1958;7(1):1–13.
116. Mizushima K, Jones PC, Wiseman PJ, Goodenough JB. Li_xCoO_2 ($0 < x < -1$): a new cathode material for batteries of high energy density. *Mater Res Bull*. 1980;15(6):783–9.
117. Wang H, Jang Y-I, Huang B, Sadoway DR, Chiang YM. TEM study of electrochemical cycling-induced damage and disorder in LiCoO_2 cathodes for rechargeable lithium batteries. *J Electrochem Soc*. 1999;146(2):473–80.
118. Wang H, Jang Y-I, Huang B, Sadoway DR, Chiang Y-M. Electron microscopic characterization of electrochemically cycled LiCoO_2 and $\text{Li}(\text{Al},\text{Co})\text{O}_2$ battery cathodes. *J Power Sources*. 1999;81–82:594–8.

119. Gabrisch H, Yazami R, Fultz B. A transmission electron microscopy study of cycled LiCoO₂. *J Power Sources*. 2003;119-121:674–9.
120. Van der Ven A, Aydinol MK, Ceder G, Kresse G, Hafner J. First-principles investigation of phase stability in Li_xCoO₂. *Phys Rev B*. 1998;58(6):2975–87.
121. Van der Ven A, Ceder G. Lithium diffusion mechanisms in layered intercalation compounds. *J Power Sources*. 2001;97-98:529–31.
122. Xia H, Lu L, Ceder G. Li diffusion in LiCoO₂ thin films prepared by pulsed laser deposition. *J Power Sources*. 2006;159(2):1422–7.
123. Ohzuku T, Ueda A. Solid-state redox reactions of LiCoO₂ (R3m) for 4 volt secondary lithium cells. *J Electrochem Soc*. 1994;141(11):2972–7.
124. Whittingham MS. Lithium batteries and cathode materials. *Chem Rev*. 2004;104(10):4271–302.
125. Dahn JR, von Sacken U, Juzkow MW, Al-Janaby H. Rechargeable LiNiO₂ / carbon cells. *J Electrochem Soc*. 1991;138(8):2207–11.
126. Nitta N, Wu F, Lee JT, Yushin G. Li-ion battery materials: present and future. *Mater Today*. 2015;18(5):252–64.
127. Schipper F, Erickson EM, Erk C, Shin J-Y, Chesneau FF, Aurbach D. Review—recent advances and remaining challenges for lithium ion battery cathodes. *J Electrochem Soc*. 2016;164(1):A6220–8.
128. Wei Y, Zheng J, Cui S, Song X, Su Y, Deng W, et al. Kinetics tuning of Li-ion diffusion in layered Li(Ni_xMn_yCo_z)O₂. *J Am Chem Soc*. 2015;137(26):8364–7.
129. Padhi AK, Nanjundaswamy KS, Goodenough JB. Phospho-olivines as positive-electrode materials for rechargeable lithium batteries. *J Electrochem Soc*. 1997;144(4):1188–94.
130. Malik R, Burch D, Bazant M, Ceder G. Particle size dependence of the ionic diffusivity. *Nano Lett*. 2010;10(10):4123–7.
131. Yang J, Tse JS. Li ion diffusion mechanisms in LiFePO₄: an *ab initio* molecular dynamics study. *J Phys Chem A*. 2011;115(45):13045–9.
132. Nishimura S-i, Kobayashi G, Ohoyama K, Kanno R, Yashima M, Yamada A. Experimental visualization of lithium diffusion in Li_xFePO₄. *Nat Mater*. 2008;7(9):707–11.
133. Franger S, Le Cras F, Bourbon C, Rouault H. LiFePO₄ synthesis routes for enhanced electrochemical performance. *Electrochem Solid St*. 2002;5(10):A231.
134. Kuss C, Liang G, Schougaard SB. Atomistic modeling of site exchange defects in lithium iron phosphate and iron phosphate. *J Mater Chem*. 2012;22(47):24889–93.
135. Ferg E, Gummow RJ, de Kock A, Thackeray MM. Spinel anodes for lithium-ion batteries. *J Electrochem Soc*. 1994;141(11):L147–L50.
136. Ohzuku T, Ueda A, Yamamoto N. Zero-strain insertion material of Li[Li_{1/3}Ti_{5/3}]O₄ for rechargeable lithium cells. *J Electrochem Soc*. 1995;142(5):1431–5.
137. Ganapathy S, Wagemaker M. Nanosize storage properties in spinel Li₄Ti₅O₁₂ explained by anisotropic surface lithium insertion. *ACS Nano*. 2012;6(10):8702–12.
138. Ziebarth B, Klinsmann M, Eckl T, Elsässer C. Lithium diffusion in the spinel phase Li₄Ti₅O₁₂ and in the rocksalt phase Li₇Ti₅O₁₂ of lithium titanate from first principles. *Phys Rev B*. 2014;89(17):174301.
139. Sugiyama J, Nozaki H, Umegaki I, Mukai K, Miwa K, Shiraki S, et al. Li-ion diffusion in Li₄Ti₅O₁₂ and LiTi₂O₄ battery materials detected by muon spin spectroscopy. *Phys Rev B*. 2015;92(1):014417.
140. Rho YH, Kanamura K. Li⁺ ion diffusion in Li₄Ti₅O₁₂ thin film electrode prepared by PVP sol-gel method. *J Solid State Chem*. 2004;177(6):2094–100.
141. Huynh LTN, Ha CTD, Nguyen VD, Nguyen DQ, Le MLP, Man TV. Structure and electrochemical properties of Li₄Ti₅O₁₂ prepared via low-temperature precipitation. *J Chem*. 2019;2019:1727859.
142. Zhang W, Seo D-H, Chen T, Wu L, Topsakal M, Zhu Y, et al. Kinetic pathways of ionic transport in fast-charging lithium titanate. *Science*. 2020;367(6481):1030–4.
143. Schmidt W, Bottke P, Sternad M, Gollob P, Hennige V, Wilkening M. Small change—great effect: steep increase of Li ion dynamics in Li₄Ti₅O₁₂ at the early stages of chemical Li insertion. *Chem Mater*. 2015;27(5):1740–50.
144. Ganapathy S, Vasileiadis A, Heringa JR, Wagemaker M. The fine line between a two-phase and solid-solution phase transformation and highly mobile phase interfaces in spinel Li_{4+x}Ti₅O₁₂. *Adv Energy Mater*. 2017;7(9):1601781.
145. Cheng X-B, Zhang R, Zhao C-Z, Zhang Q. Toward safe lithium metal anode in rechargeable batteries: a review. *Chem Rev*. 2017;117(15):10403–73.
146. Shen X, Zhang R, Shi P, Chen X, Zhang Q. How does external pressure shape Li dendrites in Li metal batteries? *Adv Energy Mater*. 2021;11(10):2003416.
147. Frank W, Breier U, Elsässer C, Fähnle M. First-principles calculations of absolute concentrations and self-diffusion constants of vacancies in lithium. *Phys Rev Lett*. 1996;77(3):518–21.
148. Heitjans P, Korblein A, Ackermann H, Dubbers D, Fujara F, Stockmann HJ. Self-diffusion in solid lithium probed by spin-lattice relaxation of ⁸Li nuclei. *J Phys F*. 1985;15(1):41–54.
149. Messer R, Noack F. Nuclear magnetic relaxation by self-diffusion in solid lithium: T1-frequency dependence. *Appl Phys*. 1975;6(1):79–88.
150. Lodding A, Mundy JN, Ott A. Isotope inter-diffusion and self-diffusion in solid lithium metal. *Phys Status Solidi B*. 1970;38(2):559–69.
151. Marion Fischer D, Duwe P, Indris S, Heitjans P. Tracer diffusion measurements in solid lithium: a test case for the comparison between NMR in static and pulsed magnetic field gradients after upgrading a standard solid state NMR spectrometer. *Solid State Nucl Magn Reson*. 2004;26(2):74–83.

152. Mali M, Roos J, Sonderegger M, Brinkmann D, Heitjans P. ^6Li and ^7Li diffusion coefficients in solid lithium measured by the NMR pulsed field gradient technique. *J Phys F*. 1988;18(3):403–12.
153. Liu J, Yuan H, Liu H, Zhao C-Z, Lu Y, Cheng X-B, et al. Unlocking the failure mechanism of solid state lithium metal batteries. *Adv Energy Mater*. 2021;12(4):2100748.
154. Doux J-M, Nguyen H, Tan DHS, Banerjee A, Wang X, Wu EA, et al. Stack pressure considerations for room-temperature all-solid-state lithium metal batteries. *Adv Energy Mater*. 2020;10(1):1903253.
155. Xu R, Liu F, Ye Y, Chen H, Yang RR, Ma Y, et al. A morphologically stable Li/electrolyte interface for all-solid-state batteries enabled by 3D-micropatterned garnet. *Adv Mater*. 2021;33(49):2104009.
156. Zhu G-L, Zhao C-Z, Peng H-J, Yuan H, Hu J-K, Nan H-X, et al. A self-limited free-standing sulfide electrolyte thin film for all-solid-state lithium metal batteries. *Adv Funct Mater*. 2021;31(32):2101985.
157. Krauskopf T, Mogwitz B, Rosenbach C, Zeier WG, Janek J. Diffusion limitation of lithium metal and Li–Mg alloy anodes on LLZO type solid electrolytes as a function of temperature and pressure. *Adv Energy Mater*. 2019;9(44):1902568.
158. Krauskopf T, Hartmann H, Zeier WG, Janek J. Toward a fundamental understanding of the lithium metal anode in solid-state batteries—an electrochemo-mechanical study on the garnet-type solid electrolyte $\text{Li}_{6.25}\text{Al}_{0.25}\text{La}_3\text{Zr}_2\text{O}_{12}$. *ACS Appl Mater Interfaces*. 2019;11(15):14463–77.
159. Kim H, Park B, Sohn H-J, Kang T. Electrochemical characteristics of Mg–Ni alloys as anode materials for secondary Li batteries. *J Power Sources*. 2000;90(1):59–63.
160. Iwamura S, Nishihara H, Ono Y, Morito H, Yamane H, Nara H, et al. Li-rich Li–Si alloy as a lithium-containing negative electrode material towards high energy lithium-ion batteries. *Sci Rep*. 2015;5(1):8085.
161. Seng KH, Park M-H, Guo ZP, Liu HK, Cho J. Self-assembled germanium/carbon nanostructures as high-power anode material for the lithium-ion battery. *Angew Chem Int Ed*. 2012;51(23):5657–61.
162. Wang J, King P, Huggins RA. Investigations of binary lithium–zinc, lithium–cadmium and lithium–lead alloys as negative electrodes in organic solvent-based electrolyte. *Solid State Ion*. 1986;20(3):185–9.
163. Inaba M, Uno T, Tasaka A. Irreversible capacity of electrodeposited Sn thin film anode. *J Power Sources*. 2005;146(1):473–7.
164. Lu Y, Zhao C-Z, Zhang R, Yuan H, Hou L-P, Fu Z-H, et al. The carrier transition from Li atoms to Li vacancies in solid-state lithium alloy anodes. *Sci Adv*. 2021;7(38):eabi5520.
165. Jow TR, Liang CC. Lithium–aluminum electrodes at ambient temperatures. *J Electrochem Soc*. 1982;129(7):1429–34.
166. Hwa Y, Sung JH, Wang B, Park C-M, Sohn H-J. Nanostructured Zn-based composite anodes for rechargeable Li-ion batteries. *J Mater Chem*. 2012;22(25):12767–73.
167. Gasparotto LHS, Borisenko N, Bocchi N, Zein El Abedin S, Endres F. *In situ* STM investigation of the lithium underpotential deposition on Au(111) in the air- and water-stable ionic liquid 1-butyl-1-methylpyrrolidinium bis(trifluoromethylsulfonyl)amide. *Phys Chem Chem Phys*. 2009;11(47):11140–5.
168. Taillades G, Sarradin J. Silver: high performance anode for thin film lithium ion batteries. *J Power Sources*. 2004;125(2):199–205.
169. Kim Y, Choi W, Kim O-H, Park H, Yun S, Thangavel R, et al. Dual lithium storage of Pt electrode: alloying and reversible surface layer. *J Mater Chem A*. 2021;9(34):18377–84.
170. Qu J, Xiao J, Wang T, Legut D, Zhang Q. High rate transfer mechanism of lithium ions in lithium–tin and lithium–indium alloys for lithium batteries. *J Phys Chem C*. 2020;124(45):24644–52.
171. Kamaya N, Homma K, Yamakawa Y, Hirayama M, Kanno R, Yonemura M, et al. A lithium superionic conductor. *Nat Mater*. 2011;10(9):682–6.
172. Mizuno F, Hayashi A, Tadanaga K, Tatsumisago M. New, highly ion-conductive crystals precipitated from $\text{Li}_2\text{S}-\text{P}_2\text{S}_5$ glasses. *Adv Mater*. 2005;17(7):918–21.
173. Seino Y, Ota T, Takada K, Hayashi A, Tatsumisago M. A sulphide lithium super ion conductor is superior to liquid ion conductors for use in rechargeable batteries. *Energ Environ Sci*. 2014;7(2):627–31.
174. Deiseroth H-J, Kong S-T, Eckert H, Vannahme J, Reiner C, Zaiss T, et al. $\text{Li}_6\text{PS}_5\text{X}$: a class of crystalline Li-rich solids with an unusually high Li^+ mobility. *Angew Chem Int Ed*. 2008;47(4):755–8.
175. Murugan R, Thangadurai V, Weppner W. Fast lithium ion conduction in garnet-type $\text{Li}_7\text{La}_3\text{Zr}_2\text{O}_{12}$. *Angew Chem Int Ed*. 2007;46(41):7778–81.
176. Aono H, Sugimoto E, Sadaoka Y, Imanaka N, Gy A. Ionic conductivity of solid electrolytes based on lithium titanium phosphate. *J Electrochem Soc*. 1990;137(4):1023–7.
177. Inaguma Y, Liquan C, Itoh M, Nakamura T, Uchida T, Ikuta H, et al. High ionic conductivity in lithium lanthanum titanate. *Solid State Commun*. 1993;86(10):689–93.
178. Asano T, Sakai A, Ouchi S, Sakaida M, Miyazaki A, Hasegawa S. Solid halide electrolytes with high lithium-ion conductivity for application in 4 V class bulk-type all-solid-state batteries. *Adv Mater*. 2018;30(44):1803075.
179. Zhao Q, Stalin S, Zhao C-Z, Archer LA. Designing solid-state electrolytes for safe, energy-dense batteries. *Nat Rev Mater*. 2020;5(3):229–52.
180. Famprakis T, Canepa P, Dawson JA, Islam MS, Masquelier C. Fundamentals of inorganic solid-state electrolytes for batteries. *Nat Mater*. 2019;18(12):1278–91.
181. Bachman JC, Muy S, Grimaud A, Chang H-H, Pour N, Lux SF, et al. Inorganic solid-state electrolytes for lithium batteries: mechanisms and properties governing ion conduction. *Chem Rev*. 2016;116(1):140–62.

182. Muy S, Schlem R, Shao-Horn Y, Zeier WG. Phonon–ion interactions: designing ion mobility based on lattice dynamics. *Adv Energy Mater.* 2021;11(15):2002787.
183. Fu Z-H, Chen X, Zhao C-Z, Yuan H, Zhang R, Shen X, et al. Stress regulation on atomic bonding and ionic diffusivity: mechanochemical effects in sulfide eolid electrolytes. *Energy Fuel.* 2021;35(12):10210–8.
184. Smith JG, Siegel DJ. Low-temperature paddlewheel effect in glassy solid electrolytes. *Nat Commun.* 2020;11(1):1483.
185. Jansen M. Volume effect or paddle-wheel mechanism–fast alkali-metal ionic conduction in solids with rotationally disordered complex anions. *Angew Chem Int Ed.* 1991;30(12):1547–58.
186. Zhang Z, Li H, Kaup K, Zhou L, Roy P-N, Nazar LF. Targeting superionic conductivity by turning on anion rotation at room temperature in fast ion conductors. *Matter.* 2020;2(6):1667–84.
187. Hanghofer I, Gadermaier B, Wilkening HMR. Fast rotational dynamics in argyrodite-type $\text{Li}_6\text{PS}_5\text{X}$ (X : cl, Br, I) as seen by ^{31}P nuclear magnetic relaxation—on cation-anion coupled transport in thiophosphates. *Chem Mater.* 2019;31(12):4591–7.
188. Wu S, Xiao R, Li H, Chen L. New insights in the mechanism of cation migration induced by cation-anion dynamic coupling in superionic conductors. *J Mater Chem A.* 2022;10:3093–101.
189. Först M, Manzoni C, Kaiser S, Tomioka Y, Tokura Y, Merlin R, et al. Nonlinear phononics as an ultrafast route to lattice control. *Nat Phys.* 2011;7(11):854–6.
190. Dhar L, Rogers JA, Nelson KA. Time-resolved vibrational spectroscopy in the impulsive limit. *Chem Rev.* 1994;94(1):157–93.
191. Minami S, Miura K, Ishioka M, Morimoto N, Isoda N, Yamamoto H, et al. Homocysteine supplementation ameliorates steatohepatitis induced by a choline-deficient diet in mice. *Hepatol Res.* 2019;49(2):189–200.
192. Muy S, Voss J, Schlem R, Koerver R, Sedlmaier SJ, Maglia F, et al. High-throughput screening of solid-state Li-ion conductors using lattice-dynamics descriptors. *iScience.* 2019;16:270–82.
193. Muy S, Bachman JC, Giordano L, Chang H-H, Abernathy DL, Bansal D, et al. Tuning mobility and stability of lithium ion conductors based on lattice dynamics. *Energ Environ Sci.* 2018;11(4):850–9.
194. Gordiz K, Muy S, Zeier WG, Shao-Horn Y, Henry A. Enhancement of ion diffusion by targeted phonon excitation. *Cell Rep Phys Sci.* 2021;2(5):100431.
195. Martínez-Juárez A, Pecharromán C, Iglesias JE, Rojo JM. Relationship between activation energy and bottleneck size for Li^+ ion conduction in NASICON materials of composition $\text{LiMM}'(\text{PO}_4)_3$; $\text{M}, \text{M}' = \text{Ge}, \text{Ti}, \text{Sn}, \text{Hf}$. *J Phys Chem B.* 1998;102(2):372–5.
196. He X, Bai Q, Liu Y, Nolan AM, Ling C, Mo Y. Crystal structural framework of lithium super-ionic conductors. *Adv Energy Mater.* 2019;9(43):1902078.
197. Kwon O, Hirayama M, Suzuki K, Kato Y, Saito T, Yonemura M, et al. Synthesis, structure, and conduction mechanism of the lithium superionic conductor $\text{Li}_{10+\delta}\text{Ge}_{1+\delta}\text{P}_{2-\delta}\text{S}_{12}$. *J Mater Chem A.* 2015;3(1):438–46.
198. Mo Y, Ong SP, Ceder G. First principles study of the $\text{Li}_{10}\text{GeP}_2\text{S}_{12}$ lithium super ionic conductor material. *Chem Mater.* 2012;24(1):15–7.
199. Weber DA, Senyshyn A, Weldert KS, Wenzel S, Zhang W, Kaiser R, et al. Structural insights and 3D diffusion pathways within the lithium superionic conductor $\text{Li}_{10}\text{GeP}_2\text{S}_{12}$. *Chem Mater.* 2016;28(16):5905–15.
200. Iwasaki R, Hori S, Kanno R, Yajima T, Hirai D, Kato Y, et al. Weak anisotropic lithium-ion conductivity in single crystals of $\text{Li}_{10}\text{GeP}_2\text{S}_{12}$. *Chem Mater.* 2019;31(10):3694–9.
201. Wang Y, Richards WD, Ong SP, Miara LJ, Kim JC, Mo Y, et al. Design principles for solid-state lithium superionic conductors. *Nat Mater.* 2015;14(10):1026–31.
202. Jun K, Sun Y, Xiao Y, Zeng Y, Kim R, Kim H, et al. Lithium superionic conductors with corner-sharing frameworks. *Nat Mater.* 2022. <https://doi.org/10.1038/s41563-022-01222-4>
203. Zabrodsky H, Peleg S, Avnir D. Continuous symmetry measures. *J Am Chem Soc.* 1992;114(20):7843–51.
204. Xu Z, Chen X, Chen R, Li X, Zhu H. Anion charge and lattice volume dependent lithium ion migration in compounds with fcc anion sublattices. *NPJ Comput Mater.* 2020;6(1):47.
205. Belsky A, Hellenbrandt M, Karen VL, Luksch P. New developments in the inorganic crystal structure database (ICSD): accessibility in support of materials research and design. *Acta Crystallogr B.* 2002;58(3):364–9.
206. Jain A, Ong SP, Hautier G, Chen W, Richards WD, Dacek S, et al. Commentary: the materials project: a materials genome approach to accelerating materials innovation. *APL Mater.* 2013;1(1):011002.
207. Culver SP, Squires AG, Minafra N, Armstrong CWF, Krauskopf T, Böcher F, et al. Evidence for a solid-electrolyte inductive effect in the superionic conductor $\text{Li}_{10}\text{Ge}_{1-x}\text{Sn}_x\text{P}_2\text{S}_{12}$. *J Am Chem Soc.* 2020;142(50):21210–9.
208. Liang X, Yang L, Lei Y, Qu L, Wang L, Cai W, et al. Selective blockage of Li-ion diffusion pathways in $\text{Li}_{10}\text{SnP}_2\text{S}_{12}$: insights from nuclear magnetic resonance. *J Phys Chem C.* 2021;125(50):27884–90.
209. Monchak M, Hupfer T, Senyshyn A, Boysen H, Chernyshov D, Hansen T, et al. Lithium diffusion pathway in $\text{Li}_{1.3}\text{Al}_{0.3}\text{Ti}_{1.7}(\text{PO}_4)_3$ (LATP) superionic conductor. *Inorg Chem.* 2016;55(6):2941–5.
210. Liu Y, Jiang X, Zhao J, Hu M. Electronic charge density as a fast approach for predicting Li-ion migration pathways in superionic conductors with first-principles level precision. *Comput Mater Sci.* 2021;192:110380.
211. Peled E. The electrochemical behavior of alkali and alkaline earth metals in nonaqueous battery systems - the solid electrolyte interphase model. *J Electrochem Soc.* 1979;126(12):2047–51.
212. Zhao C-Z, Duan H, Huang J-Q, Zhang J, Zhang Q, Guo Y-G, et al. Designing solid-state interfaces on lithium-metal anodes: a review. *Sci China Chem.* 2019;62(10):1286–99.

213. Xu R, Cheng X-B, Yan C, Zhang X-Q, Xiao Y, Zhao C-Z, et al. Artificial interphases for highly stable lithium metal anode. *Matter*. 2019; 1(2):317–44.
214. Shen X, Zhang R, Chen X, Cheng X-B, Li X, Zhang Q. The failure of solid electrolyte interphase on Li metal anode: structural uniformity or mechanical strength? *Adv Energy Mater*. 2020;10(10):1903645.
215. Haven Y. The ionic conductivity of Li-halide crystals. *Recl Trav Chim Pays-Bas*. 1950;69(12):1471–89.
216. Lörger S, Usiskin RE, Maier J. Transport and charge carrier chemistry in lithium oxide. *J Electrochem Soc*. 2019;166(10):A2215–20.
217. Ramasubramanian A, Yurkiv V, Foroozan T, Ragone M, Shahbazian-Yassar R, Mashayek F. Lithium diffusion mechanism through solid-electrolyte interphase in rechargeable lithium batteries. *J Phys Chem C*. 2019;123(16):10237–45.
218. Ahmad Z, Venturi V, Hafiz H, Viswanathan V. Interfaces in solid electrolyte interphase: implications for lithium-ion batteries. *J Phys Chem C*. 2021;125(21):11301–9.
219. Yu S, Siegel DJ. Grain boundary contributions to Li-ion transport in the solid electrolyte $\text{Li}_7\text{La}_3\text{Zr}_2\text{O}_{12}$ (LLZO). *Chem Mater*. 2017; 29(22):9639–47.
220. Gao B, Jalem R, Tian H-K, Tateyama Y. Revealing atomic-scale ionic stability and transport around grain boundaries of garnet $\text{Li}_7\text{La}_3\text{Zr}_2\text{O}_{12}$ solid electrolyte. *Adv Energy Mater*. 2021;12(3):2102151.
221. Langer J, Epp V, Heitjans P, Mautner FA, Wilkening M. Lithium motion in the anode material LiC_6 as seen via time-domain ${}^7\text{Li}$ NMR. *Phys Rev B*. 2013;88(9):094304.
222. Umegaki I, Kawauchi S, Sawada H, Nozaki H, Higuchi Y, Miwa K, et al. Li-ion diffusion in Li intercalated graphite C_6Li and C_{12}Li probed by $\mu^+\text{SR}$. *Phys Chem Chem Phys*. 2017;19(29):19058–66.
223. Funabiki A, Inaba M, Ogumi Z, Si Y, Otsuji J, Tasaka A. Impedance study on the electrochemical lithium intercalation into natural graphite powder. *J Electrochem Soc*. 1998;145(1):172–8.
224. Vikram Babu B, Vijaya Babu K, Tewodros Aregai G, Seeta Devi L, Madhavi Latha B, Sushma Reddi M, et al. Structural and electrical properties of $\text{Li}_4\text{Ti}_5\text{O}_{12}$ anode material for lithium-ion batteries. *Results Phys*. 2018;9:284–9.
225. Pan J, Cheng Y-T, Qi Y. General method to predict voltage-dependent ionic conduction in a solid electrolyte coating on electrodes. *Phys Rev B*. 2015;91(13):134116.
226. Guan P, Liu L, Lin X. Simulation and experiment on solid electrolyte interphase (SEI) morphology evolution and lithium-ion diffusion. *J Electrochem Soc*. 2015;162(9):A1798–808.
227. He M, Guo R, Hobold GM, Gao H, Gallant BM. The intrinsic behavior of lithium fluoride in solid electrolyte interphases on lithium. *Proc Natl Acad Sci USA*. 2020;117(1):73–9.
228. Lin D, Liu Y, Chen W, Zhou G, Liu K, Dunn B, et al. Conformal lithium fluoride protection layer on three-dimensional lithium by non-hazardous gaseous reagent freon. *Nano Lett*. 2017;17(6):3731–7.
229. Chen L, Chen K-S, Chen X, Ramirez G, Huang Z, Geise NR, et al. Novel ALD chemistry enabled low-temperature synthesis of lithium fluoride coatings for durable lithium anodes. *ACS Appl Mater Interfaces*. 2018;10(32):26972–81.
230. Yıldırım H, Kinaci A, Chan MKY, Greeley JP. First-principles analysis of defect thermodynamics and ion transport in inorganic SEI compounds: LiF and NaF . *ACS Appl Mater Interfaces*. 2015;7(34):18985–96.
231. Lörger S, Usiskin RE, Maier J. Transport and charge carrier chemistry in lithium sulfide. *Adv Funct Mater*. 2019;29(6):1807688.
232. Bechtold-Schweickert E, Mali M, Roos J, Brinkmann D. ${}^7\text{Li}$ diffusion constant in the superionic conductor Li_3N measured by NMR. *Phys Rev B*. 1984;30(5):2891–3.
233. Li W, Wu G, Araújo CM, Scheicher RH, Blomqvist A, Ahuja R, et al. Li^+ ion conductivity and diffusion mechanism in $\alpha\text{-Li}_3\text{N}$ and $\beta\text{-Li}_3\text{N}$. *Energ Environ Sci*. 2010;3(10):1524–30.
234. Alpen UV, Rabenau A, Talat GH. Ionic conductivity in Li_3N single crystals. *Appl Phys Lett*. 1977;30(12):621–3.
235. Kanno R, Murayama M. Lithium ionic conductor thio-LISICON: the $\text{Li}_2\text{S}-\text{GeS}_2-\text{P}_2\text{S}_5$ system. *J Electrochem Soc*. 2001;148(7):A742.
236. Murayama M, Kanno R, Irie M, Ito S, Hata T, Sonoyama N, et al. Synthesis of new lithium ionic conductor thio-LISICON—lithium silicon sulfides system. *J Solid State Chem*. 2002;168(1):140–8.
237. Homma K, Yonemura M, Kobayashi T, Nagao M, Hirayama M, Kanno R. Crystal structure and phase transitions of the lithium ionic conductor Li_3PS_4 . *Solid State Ion*. 2011;182(1):53–8.
238. Hayashi A, Hama S, Morimoto H, Tatsumisago M, Minami T. Preparation of $\text{Li}_2\text{S}-\text{P}_2\text{S}_5$ amorphous solid electrolytes by mechanical milling. *J Am Ceram Soc*. 2001;84(2):477–9.
239. Kuhn A, Duppel V, Lotsch BV. Tetragonal $\text{Li}_{10}\text{GeP}_2\text{S}_{12}$ and Li_7GePS_8 —exploring the Li ion dynamics in LGPS Li electrolytes. *Energ Environ Sci*. 2013;6(12):3548–52.
240. Ong SP, Mo Y, Richards WD, Miara L, Lee HS, Ceder G. Phase stability, electrochemical stability and ionic conductivity of the $\text{Li}_{10\pm 1}\text{MP}_2\text{X}_{12}$ ($\text{M} = \text{Ge}, \text{Si}, \text{Sn}, \text{Al}$ or P , and $\text{X} = \text{O}, \text{S}$ or se) family of superionic conductors. *Energ Environ Sci*. 2013; 6(1):148–56.
241. Bron P, Johansson S, Zick K, Schmedt auf der Günne J, Dehnens S, Roling B. $\text{Li}_{10}\text{SnP}_2\text{S}_{12}$: an affordable lithium superionic conductor. *J Am Chem Soc*. 2013;135(42):15694–7.
242. Kuhn A, Gerbig O, Zhu C, Falkenberg F, Maier J, Lotsch BV. A new ultrafast superionic Li-conductor: ion dynamics in $\text{Li}_{11}\text{Si}_2\text{PS}_{12}$ and comparison with other tetragonal LGPS-type electrolytes. *Phys Chem Chem Phys*. 2014;16(28):14669–74.
243. Kato Y, Hori S, Saito T, Suzuki K, Hirayama M, Mitsui A, et al. High-power all-solid-state batteries using sulfide superionic conductors. *Nat Energy*. 2016;1(4):16030.

244. Boulineau S, Courty M, Tarascon J-M, Viallet V. Mechanochemical synthesis of Li-argyrodite $\text{Li}_6\text{PS}_5\text{X}$ ($\text{X} = \text{Cl}, \text{Br}, \text{I}$) as sulfur-based solid electrolytes for all solid state batteries application. *Solid State Ion.* 2012;221:1–5.
245. Zhou L, Park K-H, Sun X, Lalère F, Adermann T, Hartmann P, et al. Solvent-engineered design of argyrodite $\text{Li}_6\text{PS}_5\text{X}$ ($\text{X} = \text{Cl}, \text{Br}, \text{I}$) solid electrolytes with high ionic conductivity. *ACS Energy Lett.* 2019;4(1):265–70.
246. Murugan R, Weppner W, Schmid-Beurmann P, Thangadurai V. Structure and lithium ion conductivity of bismuth containing lithium garnets $\text{Li}_5\text{La}_3\text{Bi}_2\text{O}_{12}$ and $\text{Li}_6\text{SrLa}_2\text{Bi}_2\text{O}_{12}$. *Mater Sci Eng B.* 2007;143(1):14–20.
247. Thangadurai V, Kaack H, Weppner WJF. Novel fast lithium ion conduction in garnet-type $\text{Li}_5\text{La}_3\text{M}_2\text{O}_{12}$ ($\text{M} = \text{Nb}, \text{Ta}$). *J Am Ceram Soc.* 2003;86(3):437–40.
248. Thangadurai V, Weppner W. $\text{Li}_6\text{AlA}_2\text{Ta}_2\text{O}_{12}$ ($\text{A} = \text{Sr}, \text{Ba}$): novel garnet-like oxides for fast lithium ion conduction. *Adv Funct Mater.* 2005;15(1):107–12.
249. Awaka J, Kijima N, Takahashi Y, Hayakawa H, Akimoto J. Synthesis and crystallographic studies of garnet-related lithium-ion conductors $\text{Li}_6\text{CaLa}_2\text{Ta}_2\text{O}_{12}$ and $\text{Li}_6\text{BaLa}_2\text{Ta}_2\text{O}_{12}$. *Solid State Ion.* 2009;180(6):602–6.
250. Li Y, Han J-T, Wang C-A, Xie H, Goodenough JB. Optimizing Li^+ conductivity in a garnet framework. *J Mater Chem.* 2012;22(30):15357–61.
251. Narayanan S, Hitz GT, Wachsman ED, Thangadurai V. Effect of excess Li on the structural and electrical properties of garnet-type $\text{Li}_6\text{La}_3\text{Ta}_{1.5}\text{Y}_{0.5}\text{O}_{12}$. *J Electrochem Soc.* 2015;162(9):A1772–7.
252. Peng H, Feng L, Li L, Zhang Y, Zou Y. Synthesis of $\text{Li}_{5+x}\text{La}_3\text{Hf}_x\text{Nb}_{2-x}\text{O}_{12}$ ($x = 0.2\text{--}1$) ceramics with cubic garnet-type structure. *Mater Lett.* 2017;194:138–41.
253. Xie H, Li Y, Han J, Dong Y, Paranthaman MP, Wang L, et al. $\text{Li}_6\text{La}_3\text{SnMO}_{12}$ ($\text{M} = \text{Sb}, \text{Nb}, \text{Ta}$), a family of lithium garnets with high Li-ion conductivity. *J Electrochem Soc.* 2012;159(8):A1148–51.
254. Li Y, Wang C-A, Xie H, Cheng J, Goodenough JB. High lithium ion conduction in garnet-type $\text{Li}_6\text{La}_3\text{ZrTaO}_{12}$. *Electrochim Commun.* 2011;13(12):1289–92.
255. Ohta S, Kobayashi T, Asaoka T. High lithium ionic conductivity in the garnet-type oxide $\text{Li}_{7-x}\text{La}_3(\text{Zr}_{2-x}, \text{Nb}_x)\text{O}_{12}$ ($X = 0\text{--}2$). *J Power Sources.* 2011;196(6):3342–5.
256. Zaiß T, Ortner M, Murugan R, Weppner W. Fast ionic conduction in cubic hafnium garnet $\text{Li}_7\text{La}_3\text{Hf}_2\text{O}_{12}$. *Ionics.* 2010;16(9):855–8.
257. Jin Y, McGinn PJ. Al-doped $\text{Li}_7\text{La}_3\text{Zr}_2\text{O}_{12}$ synthesized by a polymerized complex method. *J Power Sources.* 2011;196(20):8683–7.
258. Wu J-F, Chen E-Y, Yu Y, Liu L, Wu Y, Pang WK, et al. Gallium-doped $\text{Li}_7\text{La}_3\text{Zr}_2\text{O}_{12}$ garnet-type electrolytes with high lithium-ion conductivity. *ACS Appl Mater Interfaces.* 2017;9(2):1542–52.
259. Nemori H, Matsuda Y, Matsui M, Yamamoto O, Takeda Y, Imanishi N. Relationship between lithium content and ionic conductivity in the $\text{Li}_{5+2x}\text{La}_3\text{Nb}_{2-x}\text{Sc}_x\text{O}_{12}$ system. *Solid State Ion.* 2014;266:9–12.
260. Deviannapoorani C, Dhivya L, Ramakumar S, Murugan R. Lithium ion transport properties of high conductive tellurium substituted $\text{Li}_7\text{La}_3\text{Zr}_2\text{O}_{12}$ cubic lithium garnets. *J Power Sources.* 2013;240:18–25.
261. Murugan R, Ramakumar S, Janani N. High conductive yttrium doped $\text{Li}_7\text{La}_3\text{Zr}_2\text{O}_{12}$ cubic lithium garnet. *Electrochim Commun.* 2011;13(12):1373–5.
262. Arbi K, Lazarraga MG, Ben Hassen Chehimi D, Ayadi-Trabelsi M, Rojo JM, Sanz J. Lithium mobility in $\text{Li}_{1.2}\text{Ti}_{1.8}\text{R}_{0.2}(\text{PO}_4)_3$ compounds ($\text{R} = \text{Al}, \text{Ga}, \text{Sc}$, in) as followed by NMR and impedance spectroscopy. *Chem Mater.* 2004;16(2):255–62.
263. Bates JB, Dudney NJ, Gruzalski GR, Zuhir RA, Choudhury A, Luck CF, et al. Electrical properties of amorphous lithium electrolyte thin films. *Solid State Ion.* 1992;53–56:647–54.
264. Deng Y, Eames C, Chotard J-N, Lalère F, Seznec V, Emge S, et al. Structural and mechanistic insights into fast lithium-ion conduction in $\text{Li}_4\text{SiO}_4\text{-Li}_3\text{PO}_4$ solid electrolytes. *J Am Chem Soc.* 2015;137(28):9136–45.
265. Bruce PG, West AR. The A-C conductivity of polycrystalline LISICON, $\text{Li}_{2+2x}\text{Zn}_{1-x}\text{GeO}_4$, and a model for intergranular constriction resistances. *J Electrochem Soc.* 1983;130(3):662–9.
266. Li X, Liang J, Luo J, Norouzi Banis M, Wang C, Li W, et al. Air-stable Li_3InCl_6 electrolyte with high voltage compatibility for all-solid-state batteries. *Energ Environ Sci.* 2019;12(9):2665–71.
267. Li X, Liang J, Chen N, Luo J, Adair KR, Wang C, et al. Water-mediated synthesis of a superionic halide solid electrolyte. *Angew Chem Int Ed.* 2019;58(46):16427–32.
268. Park D, Park H, Lee Y, Kim S-O, Jung H-G, Chung KY, et al. Theoretical design of lithium chloride superionic conductors for all-solid-state high-voltage lithium-ion batteries. *ACS Appl Mater Interfaces.* 2020;12(31):34806–14.
269. Zevgolis A, Wood BC, Mehmedović Z, Hall AT, Alves TC, Adelstein N. Alloying effects on superionic conductivity in lithium indium halides for all-solid-state batteries. *APL Mater.* 2018;6(4):047903.
270. Sendek AD, Cubuk ED, Antoniuk ER, Cheon G, Cui Y, Reed EJ. Machine learning-assisted discovery of solid Li-ion conducting materials. *Chem Mater.* 2019;31(2):342–52.
271. Schlem R, Muy S, Prinz N, Banik A, Shao-Horn Y, Zobel M, et al. Mechanochemical synthesis: a tool to tune cation site disorder and ionic transport properties of Li_3MCl_6 ($\text{M} = \text{Y}, \text{Er}$) superionic conductors. *Adv Energy Mater.* 2020;10(6):1903719.
272. Wang S, Bai Q, Nolan AM, Liu Y, Gong S, Sun Q, et al. Lithium chlorides and bromides as promising solid-state chemistries for fast ion conductors with good electrochemical stability. *Angew Chem Int Ed.* 2019;58(24):8039–43.
273. Liang J, Li X, Wang S, Adair KR, Li W, Zhao Y, et al. Site-occupation-tuned superionic $\text{Li}_x\text{ScCl}_{3+x}$ halide solid electrolytes for all-solid-state batteries. *J Am Chem Soc.* 2020;142(15):7012–22.
274. Flores-González N, Minafra N, Dewald G, Reardon H, Smith RI, Adams S, et al. Mechanochemical synthesis and structure of lithium tetrahaloaluminates, LiAlX_4 ($\text{X} = \text{Cl}, \text{Br}, \text{I}$): a family of Li-ion conducting ternary halides. *ACS Mater Lett.* 2021;3(5):652–7.

275. Tanibata N, Takimoto S, Nakano K, Takeda H, Nakayama M, Sumi H. Metastable chloride solid electrolyte with high formability for rechargeable all-solid-state lithium metal batteries. *ACS Mater Lett.* 2020;2(8):880–6.
276. Weppner W, Huggins RA. Ionic conductivity of solid and liquid LiAlCl₄. *J Electrochem Soc.* 1977;124(1):35–8.
277. Chun H, Nam K, Hong SJ, Kang J, Han B. Design of a unique anion framework in halospinels for outstanding performance of all solid-state Li-ion batteries: first-principles approach. *J Mater Chem A.* 2021;9(28):15605–12.
278. Nakamura K, Ohno H, Okamura K, Michihiro Y, Nakabayashi I, Kanashiro T. On the diffusion of Li⁺ defects in LiCoO₂ and LiNiO₂. *Solid State Ion.* 2000;135(1):143–7.
279. Kang K, Ceder G. Factors that affect Li mobility in layered lithium transition metal oxides. *Phys Rev B.* 2006;74(9):094105.
280. Yang S, Yan B, Wu J, Lu L, Zeng K. Temperature-dependent lithium-ion diffusion and activation energy of Li_{1.2}Co_{0.13}Ni_{0.13}Mn_{0.54}O₂ thin-film cathode at nanoscale by using electrochemical strain microscopy. *ACS Appl Mater Interfaces.* 2017;9(16):13999–4005.
281. Kou J, Chen L, Su Y, Bao L, Wang J, Li N, et al. Role of cobalt content in improving the low-temperature performance of layered lithium-rich cathode materials for lithium-ion batteries. *ACS Appl Mater Interfaces.* 2015;7(32):17910–8.
282. Zhang Y, He X, Chen Z, Bai Q, Nolan AM, Roberts CA, et al. Unsupervised discovery of solid-state lithium ion conductors. *Nat Commun.* 2019;10(1):5260.
283. Bianchini F, Fjellvåg H, Vajeeston P. A first-principle investigation of the Li diffusion mechanism in the super-ionic conductor lithium orthothioborate Li₃BS₃ structure. *Mater Lett.* 2018;219:186–9.
284. Zhao Y, Daemen LL. Superionic conductivity in lithium-rich anti-perovskites. *J Am Chem Soc.* 2012;134(36):15042–7.
285. Muy S, Bachman JC, Chang H-H, Giordano L, Maglia F, Lupart S, et al. Lithium conductivity and Meyer-Neldel rule in Li₃PO₄–Li₃VO₄–Li₄GeO₄ lithium superionic conductors. *Chem Mater.* 2018;30(16):5573–82.
286. Di Stefano D, Miglio A, Robeyns K, Filinchuk Y, Lechartier M, Senyshyn A, et al. Superionic diffusion through frustrated energy landscape. *Chem.* 2019;5(9):2450–60.
287. Schlem R, Ghidui M, Culver SP, Hansen A-L, Zeier WG. Changing the static and dynamic lattice effects for the improvement of the ionic transport properties within the argyrodite Li_xPS_{5-x}Se_xI. *ACS Appl Energy Mater.* 2020;3(1):9–18.
288. Schlem R, Bernges T, Li C, Kraft MA, Minafra N, Zeier WG. Lattice dynamical approach for finding the lithium superionic conductor Li₃ErI₆. *ACS Appl Energy Mater.* 2020;3(4):3684–91.
289. Morgan BJ. Mechanistic origin of superionic lithium diffusion in anion-disordered Li₆PS₅X argyrodites. *Chem Mater.* 2021;33(6):2004–18.
290. Ohno S, Helm B, Fuchs T, Dewald G, Kraft MA, Culver SP, et al. Further evidence for energy landscape flattening in the superionic argyrodites Li_{6+x}P_{1-x}M_xS₅I (M = Si, Ge, Sn). *Chem Mater.* 2019;31(13):4936–44.
291. Xu M, Park MS, Lee JM, Kim TY, Park YS, Ma E. Mechanisms of Li⁺ transport in garnet-type cubic Li_{3+x}La₃M₂O₁₂ (M = Te, Nb, Zr). *Phys Rev B.* 2012;85(5):052301.
292. Kraft MA, Culver SP, Calderon M, Böcher F, Krauskopf T, Senyshyn A, et al. Influence of lattice polarizability on the ionic conductivity in the lithium superionic argyrodites Li₆PS₅X (X = cl, Br, I). *J Am Chem Soc.* 2017;139(31):10909–18.
293. Wv M, Neldel H. Relation between the energy constant and the quantity constant in the conductivity–temperature formula of oxide semiconductors. *Z Tech Phys.* 1937;18(12):588–93.
294. Jiang L-L, Yan C, Yao Y-X, Cai W, Huang J-Q, Zhang Q. Inhibiting solvent co-intercalation in a graphite anode by a localized high-concentration electrolyte in fast-charging batteries. *Angew Chem Int Ed.* 2021;60(7):3402–6.
295. Han X, Gong Y, Fu K, He X, Hitz GT, Dai J, et al. Negating interfacial impedance in garnet-based solid-state Li metal batteries. *Nat Mater.* 2017;16(5):572–9.
296. Chen Y, Wang Z, Li X, Yao X, Wang C, Li Y, et al. Li metal deposition and stripping in a solid-state battery via coble creep. *Nature.* 2020;578(7794):251–5.
297. Banerjee A, Tang H, Wang X, Cheng J-H, Nguyen H, Zhang M, et al. Revealing nanoscale solid–solid interfacial phenomena for long-life and high-energy all-solid-state batteries. *ACS Appl Mater Interfaces.* 2019;11(46):43138–45.
298. Banerjee A, Wang X, Fang C, Wu EA, Meng YS. Interfaces and interphases in all-solid-state batteries with inorganic solid electrolytes. *Chem Rev.* 2020;120(14):6878–933.
299. Park K, Yu B-C, Jung J-W, Li Y, Zhou W, Gao H, et al. Electrochemical nature of the cathode interface for a solid-state lithium-ion battery: Interface between LiCoO₂ and garnet-Li₇La₃Zr₂O₁₂. *Chem Mater.* 2016;28(21):8051–9.
300. Kim AY, Strauss F, Bartsch T, Teo JH, Hatsukade T, Mazilkin A, et al. Stabilizing effect of a hybrid surface coating on a Ni-rich NCM cathode material in all-solid-state batteries. *Chem Mater.* 2019;31(23):9664–72.
301. Suyama M, Kato A, Sakuda A, Hayashi A, Tatsumisago M. Lithium dissolution/deposition behavior with Li₃PS₄-LiI electrolyte for all-solid-state batteries operating at high temperatures. *Electrochim Acta.* 2018;286:158–62.
302. Han F, Yue J, Zhu X, Wang C. Suppressing Li dendrite formation in Li₂S-P₂S₅ solid electrolyte by LiI incorporation. *Adv Energy Mater.* 2018;8(18):1703644.
303. Liu M, Wang C, Zhao C, van der Maas E, Lin K, Arszelewski VA, et al. Quantification of the Li-ion diffusion over an interface coating in all-solid-state batteries via NMR measurements. *Nat Commun.* 2021;12(1):5943.

How to cite this article: Fu Z-H, Chen X, Zhang Q. Review on the lithium transport mechanism in solid-state battery materials. *WIREs Comput Mol Sci.* 2023;13(1):e1621. <https://doi.org/10.1002/wcms.1621>